THE HONG KONG
POLYTECHNIC UNIVERSITY
香港理工大學
Pao Yue-kong Library
包玉剛圖書館

Copyright Undertaking

This thesis is protected by copyright, with all rights reserved.

By reading and using the thesis, the reader understands and agrees to the following terms:

1. The reader will abide by the rules and legal ordinances governing copyright regarding the use of the thesis.
2. The reader will use the thesis for the purpose of research or private study only and not for distribution or further reproduction or any other purpose.
3. The reader agrees to indemnify and hold the University harmless from and against any loss, damage, cost, liability or expenses arising from copyright infringement or unauthorized usage.

IMPORTANT

If you have reasons to believe that any materials in this thesis are deemed not suitable to be distributed in this form, or a copyright owner having difficulty with the material being included in our database, please contact lbsys@polyu.edu.hk providing details. The Library will look into your claim and consider taking remedial action upon receipt of the written requests.

Pao Yue-kong Library, The Hong Kong Polytechnic University, Hung Hom, Kowloon, Hong Kong

http://www.lib.polyu.edu.hk

BISMUTH TELLURIDE/PEDOT:PSS COMPOSITES FOR FLEXIBLE THERMOELECTRIC GENERATORS

LIN SHUPING

PhD

The Hong Kong Polytechnic University

2021

The Hong Kong Polytechnic University

Institute of Textiles and Clothing

Bismuth Telluride / PEDOT:PSS Composites for Flexible Thermoelectric Generators

Lin Shuping

A thesis submitted in partial fulfilment of the

requirements for the degree of Doctor of Philosophy

September 2020

CERTIFICATE OF ORIGINALITY

I hereby declare that this thesis is my own work and that, to the best of my knowledge and belief, it reproduces no material previously published or written, nor material that has been accepted for the award of any other degree or diploma, except where due acknowledgement has been made in the text.

_____(Signed)

LIN SHUPING (Name of student)

ABSTRACT

Thermoelectric (TE) generators are regards as environmentally friendly technology for harvesting and recovering heat and converting it into electrical energy. Light and flexible thermoelectric generators are much desirable for numerous applications of wearable microelectronics, internet of things, and waste heat recovery. However, their progress has been hindered by the shortage of such thermoelectric materials. The various designed flexible thermoelectric generators (FTEGs) using these materials are also limited. Thus, the systematic study of both p- and n-type TE materials in one system and the affected device performance remains muted.

To address the problems, in this thesis, functional $Bi_{0.52}$ $Sb_{1.48}Te_3$/ PEDOT:PSS and $Bi_2Te_{2.68}Se_{0.32}$/PEDOT:PSS flexible thermoelectric composites have been explored in the room temperature range, aiming at producing various structure FTEGs. Annealing effects on the behavior of $Bi_{0.52}$ $Sb_{1.48}Te_3$/PEDOT:PSS and $Bi_2Te_{2.68}Se_{0.32}$/PEDOT:PSS, are discussed and compared. The satup gradient annealing temperature (423K, 593K, 623K, 673K) is programmed on the basis of the stability and configuration state of the PEDOT:PSS, observing the annealing effect on the performance of configuration state of $Bi_{0.52}Sb_{1.48}Te_3$/PEDOT:PSS, $Bi_2Te_{2.68}Se_{0.32}$/PEDOT:PSS composites. The resultant composites exhibit a surprising synergy that the composite Seebeck coefficients are higher than those of the constituent alloys and conductive polymer. The Seebeck coefficient of the optimized TE compsites exhibit superior Seebeck coefficient, power factor and figure of merit among Bi_xTe_y/PEDOT:PSS composites reported so far. The $Bi_{0.52}$ $Sb_{1.48}Te_3$/ and $Bi_2Te_{2.68}Se_{0.32}$/PEDOT:PSS thermoelectric composites advanced room-temperature

performance explored in this work are suitable for flexible printed film-structure and sandwich-like strcuture thermoelectric generators. Furthermore, thin-film and sandwich structured flexible thermoelectric generators have been developed in a systematic investigation in terms of device structure and fabrication processes.

For $Bi_{0.52}Sb_{1.48}Te_3$/PEDOT:PSS thermoelectric composite, The Seebeck coefficient of the optimized $Bi_{0.52}Sb_{1.48}Te_3$/PEDOT:PSS sample is 273.3 μV/K at room temperature, reaching that of pure $Bi_{0.52}Sb_{1.48}Te_3$, representing the highest value for Bi_xTe_y/PEDOT:PSS composites reported so far. The measured thermal conductivity of the resultant composites is within the range from 0.28 to 0.46 W/(m·K) with the enhanced thermal treatments, and their Seebeck coefficient from 168.9 to 273.3 μV/K with power factors from 4.12 to 473.5 μW/(m·K^2) near room temperature, respectively. The corresponding power factor and ZT are 473.5 μW/m·K^2 and 0.4, respectively. The possible influential factors related to the TE performace are disscussed.

For the $Bi_2Te_{2.68}Se_{0.32}$ /PEDOT:PSS composites, the Seebeck coefficient of the optimized $Bi_2Te_{2.68}Se_{0.32}$ /PEDOT:PSS sample is -218.0 μV/K at room temperature, reaching that of pure n-Bi_2Te_3, representing the highest value for Bi_xTe_y/PEDOT:PSS composites reported so far. The corresponding power factor and ZT are 306μW/m·K^2 and 0.23, respectively. The measured thermal conductivity of the resultant composites is within the range from 0.32 to 0.54 $Wm^{-1}K^{-1}$, and their Seebeck coefficient from -166.3 to -218.0 μV/K with power factors from 8.79 to 305.79 μW/(m·K^2) near room temperature, respectively. The behavior of the $Bi_2Te_{2.68}Se_{0.32}$ /PEDOT:PSS is different from the p-type ones and the corresponding poosible resaons are proposed.

Furthermore, two types, film structure and sandwich-like strcture FTEGs are desinged and fabricated using these versatile p-/n- type materials. These two protypes are based on the different varying degrees of thermal treatments of the TE mateirals.

Moderate annealing treatment is applicable to fabricate film type FTEGs. The paper-based FTEG possesses a high output power, specific and areal power density as well as excellent flexibility. FTEGs were fabricated by disperse printing on aramid paper and PDMS substrate, respectively. With ΔT = 70 K, the paper-based thermoelectric generator demonstrates a high output power of 30.8 μW, specific power density of 12.3 μW/g and areal power density of 20.5 $\mu W/cm^2$. High flexibility and durability have been displayed in cyclic bending tests of PDMS-based thermoelectric generators. The variation in electric resistance is negligible even after 100,000 bending cycles up to 2.5 cm^{-1} curvature. The solution-processible, soft and flexible composites offer unique advantages that are not available to their rigid counterparts. A printed FTEG on polyimide paper circuit board yields a specific output power of 2.5 μW/g, and an areal power density up to 4.0 $\mu W/cm^2$ when ΔT = 67 K.

High-temperature treatment is applicable to fabricate sandwich structure FTEGs. The sandwich-like FTEG possesses the higher output power, specific and areal power density than that of film type FTEGs. For the FTEG with copper fabric, the overall performance demonstrate higher than the one without copper fabric. A sandwich-structured flexible generator equipped with heat sink fabric produces an output power of 9.0 mW with a temperature difference of 45 K, which demonstrates its great promises in wearable microelectronics applications that require a driving power of several mWs. The correspoinding specific output power areal power density are 2.3 mW/g and 0.65 mW/cm^2,

respectively. The vast difference of almost three orders of magnitude between the two types of FTEGs is attributed to effects of annealing and densification processes, TE leg cross-sectional area, contact resistance, heat sink. In addition, by comparing its performance with the predicted theoretical output power, this work illustrates the large feasible scope for further improvement, and charts up a roadmap of approaches towards achieving the theoretical output upper limit.

PUBLICATIONS

Refereed Journal Papers

1. Shuping Lin, Lisha Zhang, Wei Zeng, Dongliang Shi, Su Liu, Xujiao Ding, Jiangtao Xu, Bao Yang, Jin Liu, Kwok-ho Lam, Baolin Huang, Xiaoming Tao. High performance thermoelectric composites and flexible thermoelectric generators. Under evaluation.
2. Zeng, W.; Tao, X. M.; **Lin, S. P.**; Lee, C.; Shi, D. L.; Lam, K. H.; Huang, B. L.; Wang, Q. M.; Zhao, Y., Defect-engineered reduced graphene oxide sheets with high electric conductivity and controlled thermal conductivity for soft and flexible wearable thermoelectric generators. Nano Energy 2018**,** 54, 163-174.
3. Zhang, L. S.; **Lin, S. P.**; Hua, T.; Huang, B. L.; Liu, S. R.; Tao, X. M., Fiber-Based Thermoelectric Generators: Materials, Device Structures, Fabrication, Characterization, and Applications. Adv Energy Mater 2018**,** 8 (5).
4. Li-Sha Zhang , Bao Yang , **Shu-Pin Lin**, Tao Hua, Xiao-Ming Tao, Predicting performance of fiber thermoelectric generator arrays in wearable electronic applications, Nano Energy, 2020,76, 105117.

Conference paper

1. **Lin, S. P.**; Zeng, W.; Zhang, L. S.; Tao, X. M., Flexible film-based thermoelectric generators. *Mrs Adv*, 2019, 4 (30), 1691-1697.

ACKNOWLEDGEMENTS

When I recall the memory in my previous study, a great of deal beautiful moments come to my mind. As for me, the PhD study living is like a bittersweet chocolate, the happy times let me enjoy the pleasure of learning while the tough times make me grow up. Many thanks that I would like to express to many people whom have provided help and supports to me both in my study and life.

The greatest appreciation goes to my supervisor Prof. Xiaoming Tao. Prof. Tao has wide experiences not only in textile, electronic, materials and mechanics research field, but also in fostering students. I always remember that Prof. Tao kindly embraces my poor expression and encourages me to express myself confidently. The discussion on diversity and interdisciplinary subjects in every week's group meeting has inspired me overwhelmingly. Prof. Tao has been supportive and has given me the freedom to explore in the research field without objection. I am also very grateful to Prof. Tao for her scientific advices and knowledge and many insightful discussions and effective suggestions. Thanks Prof. Tao for bringing me up to speed on this novel research program.

I am also very thankful to my co-superviosr, Dr. Kwok-ho Lam. Dr. Lam has been helpful in providing advice many times during my study. Dr. Lam is an easy going, warm and caring supervisor, and I feel lucky to be one of this group members. The study opportunity in Dr. Lam's group has open a door for me in the electrical field. I can always ask for advice and opinions on technical related issues no matter when and where. I am very grateful to Dr. Lam for his insight suggestions, enthusiasm supports, and expert guidance.

In addition, I appreciate the great help from our group members: Dr. Wei Zeng, Dr. Bao Yang, Dr. Xi Wang, Dr. Jianliang Gong, Dr. Fei Wang, Dr. Jian Song, Dr. Qiao Li, Dr. Rong Yin, Dr. Jie Feng, Dr. Lisha Zhang, Ms. Ying Li, Ms. Su Liu, Ms. Linlin Ma, Ms. Ying Xiong, Mr. Jin Liu, Mr. Linqi Pan, Mr. Jun Li, Mr. Zehua Peng, Ms. Yufei Xiang, Mr. Ziheng Zhang, Ms. Ching Lee, Mr. Shirui Liu. Ms. Xingxing Yang. As well as from Dr. Lam's group members: Dr. Dongliang Shi, Mr. Zhiming Geng, Dr.Lu Shi, Dr. Qi Zhang, Ms.Ying Li, Dr. Baojun Liu, Dr. Ruitao Zhou.

I also would like to express my sincere appreciation to the panels for their commitment of efforts and reviews in this process. I would like to thank The Hong Kong Polytechnic University for a postgraduate scholarship. The supports from the laboratory and general office are also highly appreciated. Many thanks to the technicians and staffs in general office for the guidance on my study. Many thanks to Dr. Patrick Pang, his very careful and patient technical guidance in the laboratory help me a lot. Many thanks to Dr Nuruzzaman Noor for the encouragement, his humor and understanding let me know never deny myself no matter how many times I failed.

I am grateful for time spent with friends, for our memorable trips, encouraging talking and sharing. Many thanks to Dr. Yingqiao Yang, Dr. Yelan Xiao, Dr. Lisha Zhang, Ms. Ruichen Dai, Ms. Fengna Chen, Dr. Ling Chen, Ms. Weilin Weng. Thanks to Serene Vitale, her flexibility in marine biology, fashion industry, and humanities inspired me a lot.

Finally, special thanks to my beloved family, my beloved parents, my beloved brother and sister. They are always there for me. Their endless love and everlasting faith make this thesis possible. I love you forever.

TABLE OF CONTENTS

LIST OF FIGURES

LIST OF TABLES

LIST OF SYMBOLS AND ABBREVIATIONS

General Symbols

ΔT	Temperature Difference
n	Carrier Concentration
μ	Mobility
T	Temperature
κ	Thermal conductivity
q	Electrical charge

Abbreviations

TE	Thermoelectric
FTEG	Flexible thermoelectric generator
3D	Three-dimensionally
Ag	Silver
PEDOT:PSS	Poly(3,4-ethylenedioxythiophene) polystyrene sulfonate
Bi_2Te_3	Bismuth telluride
ZT	Figure of merit
PDMS	Polydimethylsiloxane
FTEGs	Flexible thermoelectric generators
XRD	X-ray diffraction
DMSO	Dimethylsulfoxide
EtOH	Ethanol
PVA	Polyvinyl acetate
HCl	Hydrochloric acid
$SnCl_2$	Stannous chloride
DI water	Deionized water
SEM	Scanning Electron Microscopy
XPS	X-ray Photoelectron Spectrometer

PF	Power Factor
TGA	Thermogravimetric Analysis

Chapter 1 INTRODUCTION

1.1. Background

Industrial waste heat is usually hard to apply in practice and most waste heat is discharged into environment, becoming the potential risk to the whole ecological environment. The Sankey diagram in **Figure 1.1** demonstrates the waste heat produced distribution of 2012 in worldwide, based on the flow chart by the Lawrence Livermore National Laboratory.(*1*) Only about 28.2% of energy (133.659 PJ) is devoted into daily life services like transportation, industrial, residential and commercial. In addition, the exhausts/effluents part has a share of 52 % . From the perspective of energy recycle or recovery, this power source seems “flexible”, and generally hard to collect.

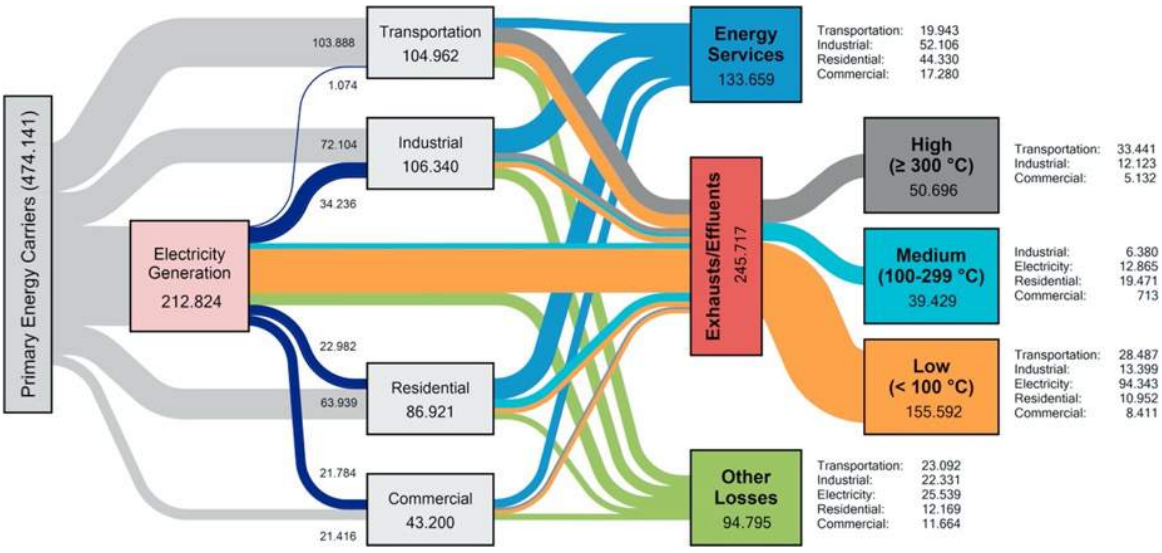

Figure 1.1Estimated global waste heat distribution of 2012 in PJ. (*1*)

The waste heat temperature distribution further provides insight into the detailed sectoral shares of exhausts/effluents fraction (**Figure 1.2**). The waste heat is divided into three temperature gradient, below 100 °C, within 100 to 299 °C, and more than 300 ºC. The low

temperature waste heat (100 °C) show a relatively high proportion in all sectors, especially the commercial section. This low-grade waste heat may be utilized by 'useful' energy transformation.(*1*) Specifically, more than 50% of the energy used in automobile industry is the exhaust heat (*2*), and this kind of energy lost reside in various aspects of human's life.

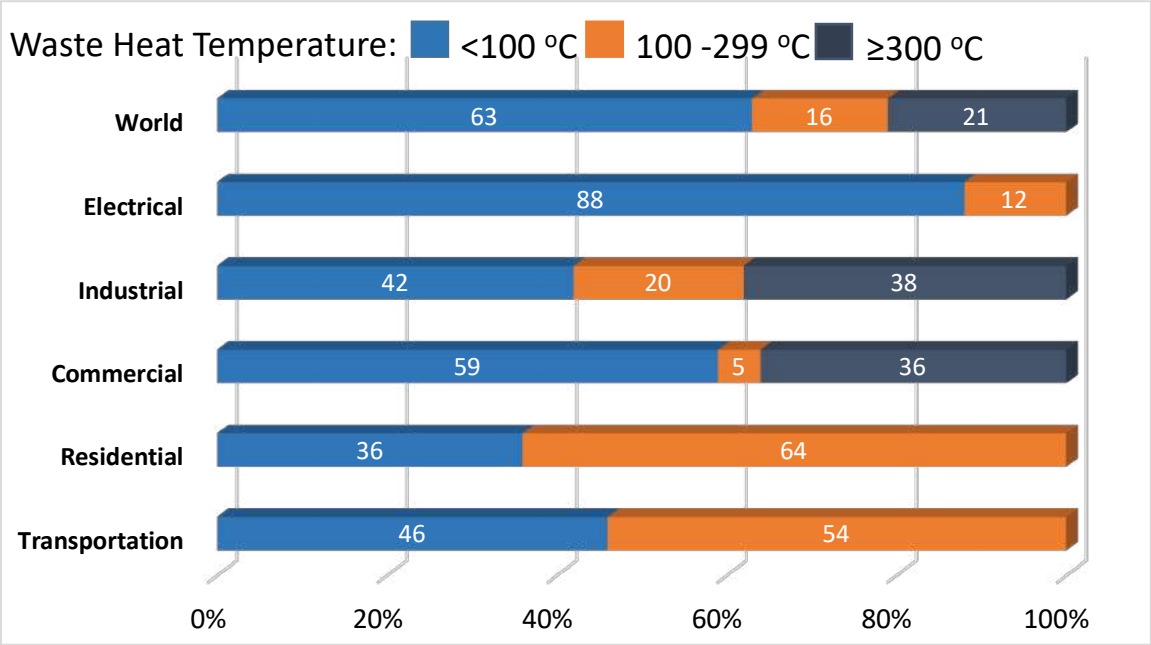

Figure 1.2 Sectoral shares of waste heat distribution.(*1*)

The human body also can work as a remarkable heat engine. It can change chemical energy from the nutrient into heat and mechanical energy while helping support vital energy. When the body works hard, it will release much heat energy to the environment to maintain the inner thermal balance. The mechanisms of mammalian temperature regulation help us to know more about the potentiality of temperature-sensitive system. When people are at a cold or warm ambient conditions, the skin temperatures are the minimum in the upper and lower extremities (about 28-31 °C) and the core body is adjusted at 37 °C.(*3*) (**Figure 1.3**)

The human body mainly releases heat to the external environment by convection, radiation, or evaporation. The results of heat flux distribution are illustrated in **Figure 1.4**. It showed

that the experimental heat fluxes range in different parts of the body. An wearable thermoelectric generator can be designed to gather energy from human body motion and devoting it to a wearable application.

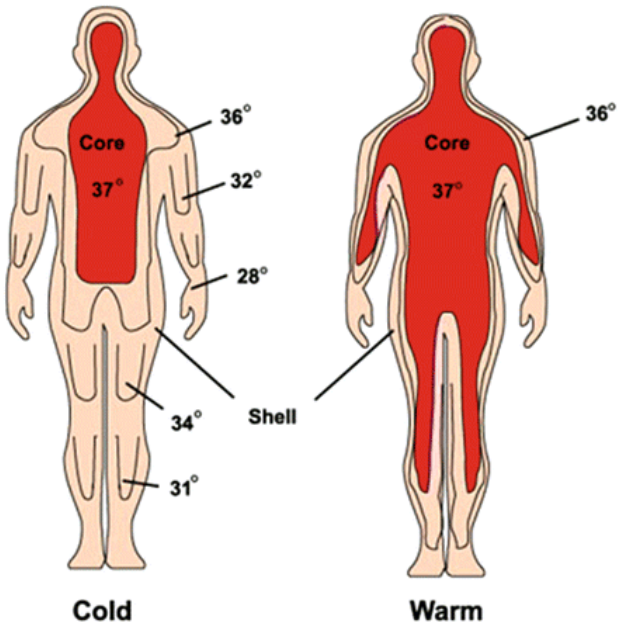

Figure 1.3 Core and skin surface temperature distribution.(*4*)

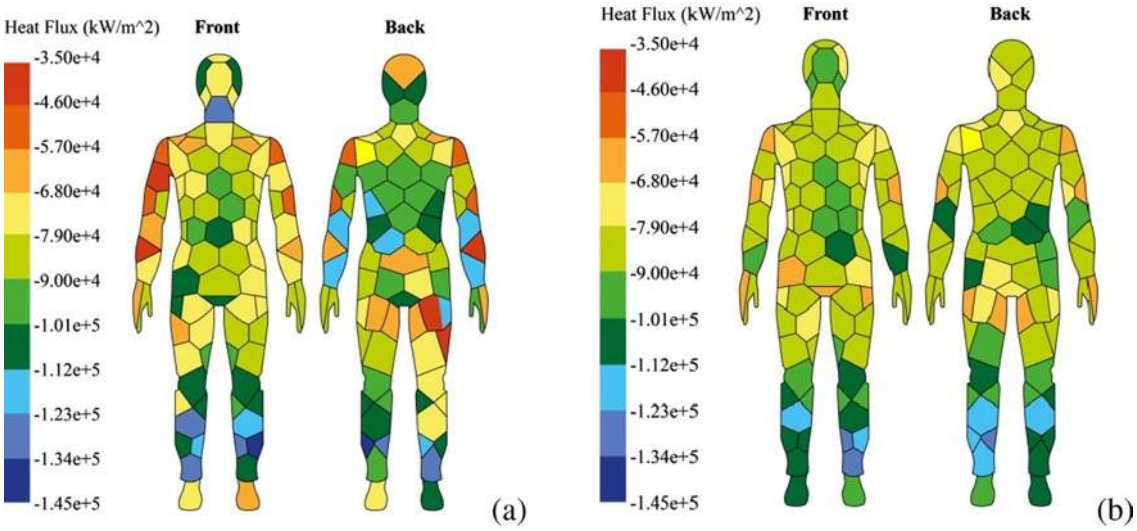

Figure 1.4 Heat flux distribution of manikin surface, for (a) experiment, and (b) simulation.(*5*)

Considering the situation discussed above, a serious of lightweight and flexible energy storage devices are favoured to solve this heat loss issue. Thermoelectric technology is widely believed as a green and environmentally benign strategy for collecting heat and converting into the electrical power. Moreover, in addition to waste heat energy utilization, flexible thermoelectric generators (FTEGs) with light-weight and large-area have drawn an remarkable attention as a potential power supplier for wearable microelectronic systems, active microclimate controlling wearable systems. (*6*) The immediate energy transformation from body heat to electrical power without external force is helpful for self-powering electronics.

Thermoelectric effect is based on a series of physical phenomenons, namely Seebeck effect, Peltier effect, and Thomson effect, which were discovered successively in 19th century. **Figure 1.5** presents the real functioning thermoelectric materials and devices.

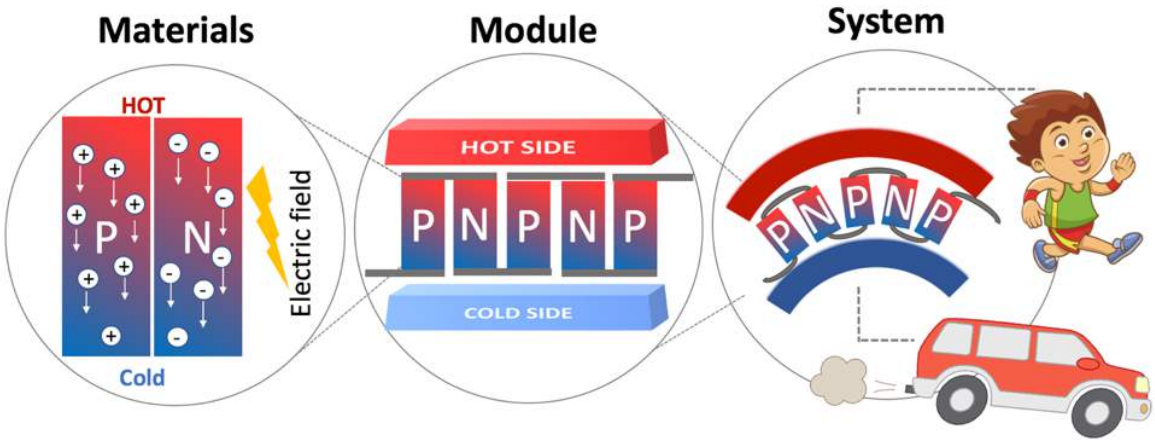

Figure 1.5 Illustration diagram of TE material and TE application

Generally, the key parameters to evaluate the materials or device efficiency should be these three intrinsic properties: Seebeck coefficient, electrical conductivity and thermal

conductivity. For the thermoelectric materials, developing superior performance thermoelectric materials means tailoring interrelated thermoelectric physical parameters-electrical conductivity, Seebeck coefficient, and thermal conductivity to achieve optimum inherent balance. Both high electrical conductivity and Seebeck coefficient are essential to the superior thermoelectric performance for practical applications. In the same vein, low thermal conductivity is necessary to keep a high temperature gradient in the thermoelectric generator design. In the thermoelectric field, most of the scientists orient their interests from the TE materials toward to the TE applications. For the standard commercial thermoelectric modules, it consists of multi p- and n-type semiconducting chips covered with two metallized ceramic plates. The ceramic plates here are rigidity and electrical insulation to the system.

TE materials can be optimized to work in different temperature region. Bismuth Telluride (Bi_xTe_y) type semiconductors are most commonly used TE materials, other materials like Silicides, Skutterudites, Zintl phase, Clathrate, Stoichiometric copper selenide (Cu_2Se) and tetrahedrite are also developed for thermoelectric applications. Recently, another category of organic conducting polymers like polyaniline (PANI), polythiophene (PTH), poly(3,4-ethylenedioxythiophene): poly(styrenesulfonate)/tosylate (PEDOT-Tos), polyacetylene (PA), polypyrrole (PPY), polycarbazoles(PC), polyphenylenevinylene (PPV) are being explored owing to the intrisinc flexibility and solution processability.

Harvesting thermal energy from three-dimensional complex shaped objects or human body requires a generator device with low rigidities of bending, in-plane shear and tensile deformation so that intimately close contacts and efficient heat transfer can be achieved between the generator and heat source. Therefore, light and flexible thermoelectric generators (FTEGs) working at room- or low-temperature are much desirable for

applications of wearable microelectronics, IoT, active microclimate controlling systems and waste heat utilization.(*7-12*)

An output power in the order of mini-watts from an FTEG, operating within a temperature difference of ~50 K, is required for driving common wearable microelectronic and IoT devices working at near room temperature. The FTEG output performance depends on its functional and structural materials, device structural design and fabrication process. At present, heavy and rigid semi-conductor functional and structural materials have been used to fabricate most thermoelectric generators that require annealing at high temperature, at which most polymers or fibers cannot survive. While the generators equipped with rigid thermoelectric semiconductors can reach the required output power, flexible polymeric TE materials do not offer such high performance and long-term stability. New high-performance flexible TE materials must be developed so that they can be processed via cost-effective operations at room- or low-temperature for FTEG fabrication. The state-of-arts flexible TE precursor materials are in the solution form, which normally consists of inorganic semiconductors, organic binder or organic conducting polymers. They can be printed, painted, or drop casted, followed by drying or curing processes at an elevated temperature,[8] in order to form solid TE materials or structures. To fabricate FTEGs from such precursors, a great difficulty is that the inevitable organic-conducting binders residuals between the semiconducting particles bring down the TE performance. Compromise may be necessary to strike a balance between the flexibility and performance of FTEGs.

There are several major types of FTEGs categorized by their device structures, that is, thin-film, sandwich and fabric structured FTEGs. An increasing number of thin-film structured FTEGs has been reported, where physical/chemical deposition, photolithography, patterning, and ink printing have been used.(*11*) The ink printing is one of the favourable

techniques for the flexible device fabrication because of material saving, one-shot synthesis, structural flexibility and low-temperature operation. However, thin-film structured FTEGs demonstrated have a limited output power in a range of nW~μW.(*13, 14*) The sandwich-structured FTEGs have better performance. Cho's group has developed several lightweight watch-like Bi_2Te_3-based FTEGs via screen printing.(*15*) However, high temperature annealing is usually needed for such FTEGs. The functional materials are semi-conductive alloys, rigid but have high TE performance. Son's group reported p- and n-type Bi_2Te_3 inorganic paints, geometrically compatible to surface of any shape.(*16*) The same materials system was used to fabricate relatively rigid conformal cylindrical generators.(*17*) The fabric type FTEGs are new comers, yet they show some promises in flexibility but fail to offer high performance. The impacts of FTEG device structure on their output performance have remained elusive. For instance, so far very few studies have paid attention to the heat sink effect on FTEGs, although improved performance is known for a rigid generator with heat sink.

1.2 Problem Statement

The thermoelectric generators are facing decades of transformation, such as flexible application in irregular-shape heat sources. One of the big challenges is how to design thermoelectric generators (TEG) employing these materials for steady, reliable, and nimble power generation. Apparently, a change of technology paradigm is compulsory from existing rigid generators to flexible ones, which can be easily integrated on curved three dimensional surfaces like human body or machine with a large surface area.(*11*)

The progress of FTEGs has been hindered by lack of suitable thermoelectric materials, poor understanding of structural design of the flexible devices and their fabrication process.

Researchers have been working on new FTEGs that can be printed on flexible thin-films, which reduces the costs of fabrication further. However, most TE generators were fabricated by using heavy and rigid TE materials that require annealing at high temperature, where most polymer films or fibers cannot survive. Flexible polymeric TE materials do not offer high performance and have great challenges with regard to long-term stability. There are several important issues:

1. Materials diversity: Most of flexible TE works have focused on either p-type or n-type flexible materials. More investigations on p-type flexible materials have been reported than n-type materials owing to the challenges in n-type modifying of organic conducting polymers. Many n-type conducting polymers are unstable in the air, which pares their applications in TE fields. Both the p- and n-types are essential in the fabrication of π-FTEG facilities. The FTEGs should be fabricated via cost-effective solution-based approaches at low or room temperature. Inorganic based materials like Bi_xTe_y/PEDOT:PSS, Bi_xTe_y, Ag_2Se, SiGe and conductive polymers are used for flexible TE film fabrication.

2. FTEGs structure: Sandwich and flexible film structures are two major FTEGs device designs. The flexible film type uses conducting polymers or graphene based materials. For the sandwich structure type, most of them consists of rigid semiconductors, and require high temperature post treatments. To our best knowledge, up-to-date now, no comparative works has reported on the effects of device structure using the same materials systems. This is important since this investigation can help the researchers to design optimal FTEGs.

3. Materials performance and effects of processing conditions: The flexible TE materials are in solution form which consists of inorganic semiconductors and organic binder,

and these materials can be printed, painted, or drop casted. However, from the solution to solid state, very little was known on the factors that influence the three basic TE properties and micro-structures of the TE materials individually and the internal connections among them.

1.3 Objectives

In order to address the current limitations of FTEGs, we set up the research goal. Try to explore and develop a novel, high performance of inorganic/ organic TE composites, which are suitable for 2D or 3D flexible thermoelectric generators at room-temperature.

The specific objectives are listed as follows:

(1) To prepare novel inorganic/ organic TE composite ink suitable for printing processes.

(2) To study the influences of annealing temperature on TE properties of the solid composites.

(3) To determine the effects of influencing factors and to identify operational mechanisms of inorganic/ organic TE composites.

(4) To design and fabricate FTEGs on flexible substrates with 2D film and 3D sandwich structure, then compare the device performances.

In order to achieve the above objectives, appropriate techniques or strategies will be selected to conquer the main difficulties step by step.

1.4 Methodology

In this section, detailed methodology includes the main technique for FTEGs fabrication, data collection or generation, as well as data analysis.

(1) A comprehensive review will be conducted on state-of- the- art of flexible TE materials and FTEGs. Problems and major challenges will be identified, together with understanding specific procedures or techniques used to prepare TE materials and FTEG devices.

(2) Inorganic- organic strategy will be employed to fabricate the TE materials for FTEGs. The favorable inorganic/ organic TE composite systems will be selected as the precursors for the FTEGs. Properties and performance of both the TE materials and FTEGs will be studied experimentally.

(3) Material characterization

After the TE material selection, instruments for materials various characterization will be illustrated here.

a. **X-ray diffraction** is a rapid analysis technique for the material phase. We can obtain detail structure information of measured substance, for example, unit cell dimensions, orientation, crystallinity or even the particle size. This technique is widely used in material science. The forms of analysed material are various, both films and powders can be measured. In this measurement, a finely focused monochromatic radiation is produced by a cathode ray tube, then directed toward the sample. The interference pattern from sample is then generated and conformed to Bragg's Law ($n\lambda=2d\sin\theta$). By collecting and counting the scattered intensity, all the possible structure information can be provided. The

crystalline structure of TE materials was obtained from Rigaku Smart Lab with Cu Kα radiation (λ = 1.5406 Å).

b. **Fourier-transform infrared spectroscopy** (FTIR) has been widely used in organic chemistry, polymer science, and medical science, etc. It can help researchers to get the obtain the absorption or emission spectrum of samples in Infrared scope. During the measurement, the samples can absorb the infrared radiation with specific wavelengths. It will induce the dipole vibration of chemical bonding or functional group in the molecules. This information helps to confirm the sample structure. The advantages of this technology are 1) simple and quick test; 2) available to the various samples, such as liquid, solid powders, or gel; 3) cost-effective; 4) non-damage test. In this work, FT-IR spectra of TE materials are recorded on Perkin Elmer Spectrum 100 FT-IR Spectrometers.

c. **Raman spectroscopy** is another technique which can provide details on molecular vibrations and material connections. Different from FTIR spectroscopy, which is sensitive to OH vibration in water, Raman is sensitive to homo-nuclear molecular bonds. Thus Raman technique is an ideal strategy to study the biological materials and chemical compound in water. The measured wavelength of Raman spectroscopy range from 50 cm^{-1} to 4000 cm^{-1}, covering most inorganic and organic materials. In addition, the diameter of laser beam is about 0.2-2mm, that means a very small quantity of materials is required for the detection. In this work, Raman spectra measurements are carried out on a Raman spectrometer (BaySpec's Nomadic™ Raman microscope 3-in-1, λ_{exc}=532 nm).

d. **The scanning electron microscope** (SEM) is based on the interaction between high-energy electrons and material surface. Using SEM, we can observe the surface morphology of the sample directly, also can get the information of chemical composition, and crystalline

structure and material orientation. The morphology of TE materials and TE films are characterized by scanning electron microscopy (Tescan VEGA3).

e. **X-ray photoelectron spectroscopy** (XPS) is a classical method for the analysis of surface composition and surface chemistry. According to the position and intensity of the peaks in an energy spectrum, we can get the chemical state and element making up the sample easily. XPS analysis is measured by Physical Electronics 5600 multi-technique system, using monochromatic Al-alpha source.

f. **Thermogravimetric analysis** is used to study the thermal stability, revealing weight variation with temperature. Thermal stability analysis of TE materials is conducted on thermogravimetric analyzer (METTLER TOLEDO Thermal Analysis, STARe system) in an atmosphere of nitrogen.

(4) TE materials performance evaluation

Thermal conductivity:

The thermal conductivity was measured by laser flash apparatus (LFA 457 MicroFlash®, NETZSCH Group, German).

Seebeck coefficient and electrical conductivity:

Seebeck coefficient and electrical conductivity of the TE films were obtained in the in-plane direction by SBA 458 Nemesis® measurement Setup (NETZSCH Group, German).

Power factor and ZT: PF is calculated by its Seebeck coefficient and electrical conductivity generated in the same temperature difference, $PF = \sigma S^2$. The dimensionless

Figure of Merit (ZT) is calculated from the Seebeck coefficient (*S*), electrical resistivity (ρ) and thermal conductivity (κ), that is $ZT = \frac{\sigma S^2}{\kappa} T$.

Hall concentration and mobility:

Hall effect of TE samples were tested by pressure-assisted molybdenum contacts equipmented with 2T magnet, using the van der Pauw technique.

(5) FTEGs fabrication and performance assessment

For the FTEG, the TE output performance is measured using a lab-made system which developed in our group. This measurement system includes a Keithley 2700 multimeter, Whatlent TEC temperature Control, and Anbat AT4516 temperature detector together with a temperature difference unit measure the actual temperature difference of the device as close as possible . The output voltages will be measured by Keithley 2700 and temperature difference of the module will be tested by Anbat AT4516 simultaneously.

1.5 Research Significance

The novelty of this work lies in the following aspects:

(1) New ink paste suitable for disperse printing is synthesized, and its resultant composite comprising $Bi_{0.52}$ $Sb_{1.48}Te_3$/PEDOT:PSS exhibits superior Seebeck coefficient, power factor and figure of merit among Bi_xTe_y/PEDOT:PSS composites reported so far. The Seebeck coefficient of the optimized $Bi_{0.52}Sb_{1.48}Te_3$/PEDOT:PSS sample is 273.3 μV/K at room temperature, reaching that of pure $Bi_{0.52}Sb_{1.48}Te_3$, representing the highest value for Bi_xTe_y/PEDOT:PSS composites reported so far.

(2) Another n-type $Bi_2Te_{2.68}Se_{0.32}$ /PEDOT:PSS composites with high perfomrnance, flexibility and stability is successfully prepared. The Seebeck coefficient of the optimized $Bi_2Te_{2.68}Se_{0.32}$ /PEDOT:PSS sample is -218.0 μV/K at room temperature, reaching that of pure n-Bi_2Te_3, representing the highest value for Bi_xTe_y/PEDOT:PSS composites reported so far.

(3) A solution-based, moderate-temperature fabrication process of FTEG devices is firstly described. TE composites was printed on various substrates providing a mechanically soft and robust support that ensures an assortment of applications in complex environment. The intricate microstructure, enabled by 3D multi-material printing, becomes a well-organized and flexible precursor for FTEG. The superior-performance TE composite, facile and cost-effective fabrication methods and findings of this study will facilitate a paradigm shift for the thermoelectric applications from rigid devices to flexible, large-sized, light and deformable devices.

(4) High-temperature treatment is applicable to fabricate sandwich structure FTEGs. The sandwich-like FTEG possesses the higher output power, specific and areal power density than that of film type FTEGs. For the FTEG with copper fabric, the overall performance demonstrate higher than the one without copper fabric. A sandwich-structured flexible generator equipped with heat sink fabric produces an output power of 9.0 mW with a temperature difference of 45 K, which demonstrates its great promises in wearable microelectronics applications that require a driving power of several mWs. In addition, by comparing its performance with the predicted theoretical output power, this work illustrates the large feasible scope for further improvement, and charts up a roadmap of approaches towards achieving the theoretical output upper limit.

1.6 Outlines of the Report

The thesis on flexible thermoelectric generators is presented in six chapters. The following description gives a brief content of each chapter forming this thesis:

Chapter 1 presents the background, problem statements, objectives, originality and significance of the research. It also provides an outline of the thesis.

Chapter 2 offers a brief review of the theory, measurement methods and recent developments of flexible TE materials and FTEGs. First, the theoretical background of TE effect and relevant properties are introduced. After that, state-of-the-arts of inorganic or organic TE and flexible TE materials are reviewed in detail. Finally, current developments of FTEGs are presented.

In chapter 3, the research work of p-type flexible thermoelectric materials is unfolded in detail. First, the state of the art of flexible thermoelectric materials are introduced, and then the materials for the FTEGs is selected according to defined criteria. Secondly, the structural characterization and performances of composite materials are reported. In this way, this chapter lays a solid foundation for the subsequent FTEG fabrication presented in Chapter 5 .

Chapter 4 studies the n-type flexible thermoelectric materials. The behavior of n-type flexible materials is investigated, and the optimal treatments for the TE performance are chosen to fabricate the π-FTEGs with p-type materials.

Chapter 5 presents the electrical and thermal performance of TEG devices. Also, two types of FTEGs are presented. Fabrication processes and performance evaluation of FTEGs are concretized.

Chapter 6 provides a summary of the results, the limitation of the work, and suggestions for future studies.

Chapter 2 LITERATURE REVIEW

2.1 Introduction of Thermoelectric Effect and Thermoelectric Generators

Thermoelectric effect describes a physical phenomenon which a temperature gradient is directly converted to electric voltage and in reverse via a thermocouple.(*18*) The temperature difference in the materials will induce the motion of electrical particles and heat arising from a change in the equilibrium distribution function $f(\kappa)$. In other words, thermoelectric effect is based on the transportation of electrical particles and energy in conducting materials. Thermoelectric effect refers to three identically individual effects, that is, Seebeck effect, Peltier effect, and Thomson effect.(*18*) During the 1820s, a German physicist, Thomas Johann Seebeck first observed the phenomena that the magnetic field was produced in the closed current loop which consisted of two dissimilar conductors (conductor A, and conductor B) when one conductor (A or B) was heated (**Figure 2.1 a**). Then in 1834, Jean-Charles Peltier found the reverse phenomenon in which the temperature difference occurred on the junction of two different conductors when the power supplied in the circuit, which is later called Peltier effect (**Figure 2.1 b**). In 1851, William Thomson predicted another new effect that the heat absorption or releasing occurred when a current flows in a conductor with a temperature gradient (**Figure 2.2 c**).

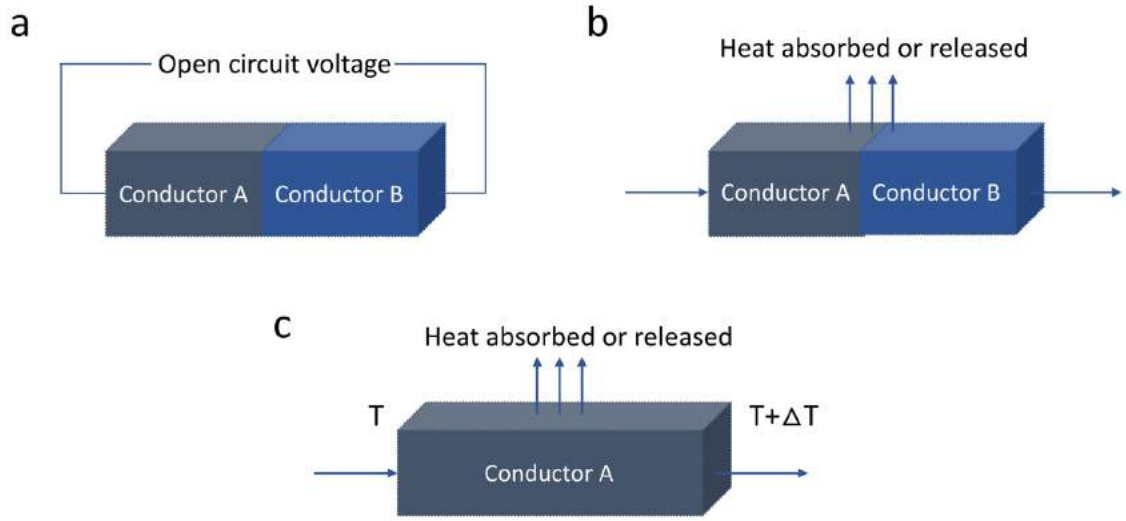

Figure 2.1 A schematic demonstration of (a) Seebeck effect, (b) Peltier effect and (c) Thomson effect.

The physical significance of thermoelectric effects is to realize conversion between heat energy and electrical power. In the Seebeck effect (**Figure 2.1 a**), the equation of $S = \Delta V/\Delta T$ is defined as Seebeck coefficient, micro volt per kelvin (μV/K) is obtained as the unit of Seebeck coefficient. For the Peltier effect (**Figure 2.1 b**), a current flowed through the junction of conductor A and B where heat is absorbed or released, $\pi = Q/I$. In the Thomson effect, the heat absorption or rejection (Q) is calculated by $Q = \beta I \Delta T$, where β is defined as the Thomson coefficient, thus, $\beta = Q/I\Delta T$ (**Figure 2.1 c**).

Generally, there have five important parameters to evaluate the performance of the TE materials: (1) Seebeck Coefficient (*S*) is used to quantified the voltage generated under per unit temperature in a system caused by a thermal gradient, $S = \frac{\Delta V}{\Delta T}$. (*19*) (2) Electrical Conductivity (σ) competes with (3) thermal conductivity (κ) in semiconductors. Specifically, materials which have high electrical conductivity, advanced Seebeck coefficient and low thermal conductivity are likely to boost high power output.(*19*) (4)

Power Factor (PF) is the combination of electrical conductivity and Seebeck coefficient, and it is used to determine the ability of a material as TE function in a TEG or a TEC. PF is calculated by its Seebeck coefficient and electrical conductivity under the same temperature difference, $PF = \sigma S^2$.(*20*) (5) The dimensionless Figure of Merit (ZT) is a parameter to evaluate the efficiency of materials, based on the Seebeck coefficient (*S*), electrical resistivity (ρ) and thermal conductivity (κ), that is $ZT = \frac{\sigma S^2}{\kappa} T$. (*20*) As shown from above description, these five parameters are not individually, and they have a relationship of interaction instead. The equation of Mott-Schottky has been used to depict the relationship among Seebeck coefficient, thermal conductivity, and electrical conductivity, (*21*)that is:

$$S = \frac{\pi^2 {\kappa_B}^2 T}{3q} \left[\frac{1}{\sigma(\varepsilon)} \frac{d\sigma}{d\varepsilon} \right]_{\varepsilon=\varepsilon F}$$

where the conductivity $\sigma = n(\varepsilon) e \mu(\varepsilon)$ and the electron concentration is $n(\varepsilon) = D(\varepsilon) f(\varepsilon)$, here $D(\varepsilon)$ is the density of states function and $f(\varepsilon)$ is the Fermi-Dirac distribution function. (*21*) And we can get the following equation:

$$S = \frac{\pi^2 {\kappa_B}^2 T}{3q} \left[\frac{1}{n} \frac{dn(\varepsilon)}{d\varepsilon} + \frac{1}{\mu} \frac{d\mu(\varepsilon)}{d\varepsilon} \right]_{\varepsilon=\varepsilon F}$$

In addition, the ratio of the thermal conductivity κ to the electrical conductivity s can be written as Wiedermann-Franz equation,(*21*)

$$\frac{\kappa}{\sigma} = \frac{\pi^2 \kappa_B^2 T}{3q^2}$$

Based on these two equations, we can clearly see that the relationship of S and σ are anticorrelated. In general, it is hard to increase *n*, μ and S of one material at the same time. This inherently contradiction becomes one of the main reasons why powering efficiency

enhancement of traditional TE semiconductors under a difficult circumstance since 1950s.(*22*)

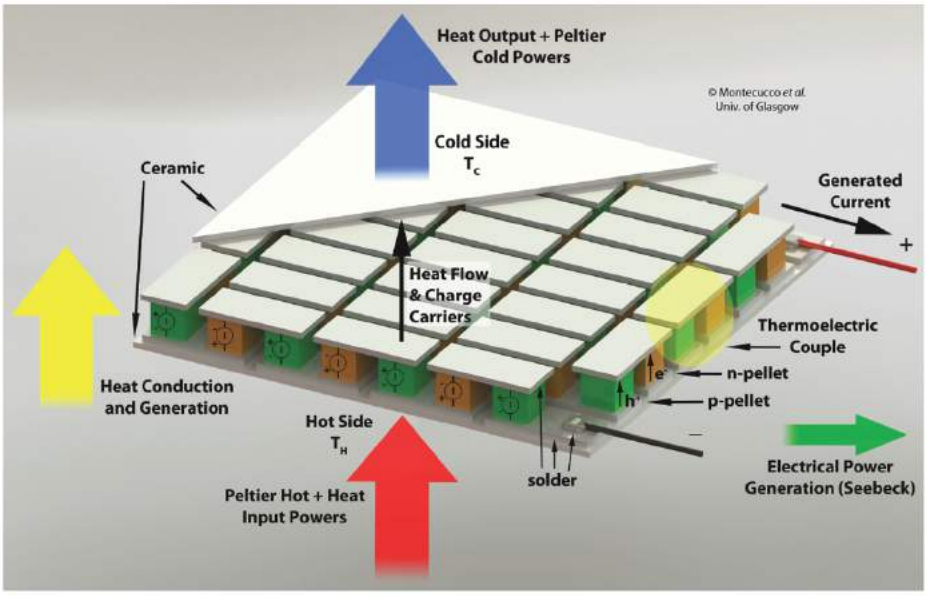

Figure 2.2 A schematic thermoelectric generator structure.(*23*)

As shown in Figure 2.2, a traditional thermoelectric generator compromises of array of p-/n-type chips which are connected electrically in series and thermally in parallel, showing as the sandwich structure. The n- and p-type pellets are connected with copper electrodes, and the potentials from the pellets are series-adding. Top and bottom ceramic layers serve as electrical isolation and mechanical substrate for the device assembly. The resulting module works without any vibration or noise since there are no moving parts. Thermoelectric devices can be handled in Peltier mode for heat output, and in Seebeck mode for power generation. In these two operating modes all the thermoelectric phenomena can be described in Figure 2.3 as below.

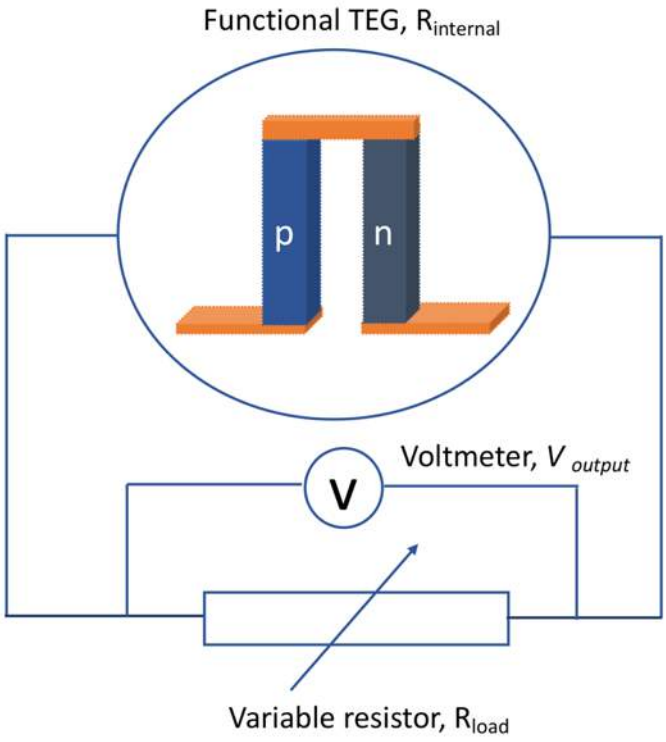

Figure 2.3 A scheme of a real working thermoelectric device.

The device is connected with a load resistance (R). Before calculating the efficiency of the thermoelectric device, the approximation and assumption need to be considered. In this system, we can neglect, as an approximation, the influence of Thomson effect. Then, for the Joule heating, assuming that half of the Joule heat can be reused by the hot side. Then the current can be calculated by

$$I = \frac{V}{R_{int}+R_{load}} = \frac{S\,(T_h-T_c)}{(R_{int}+R_{load})} \quad \text{.....} \quad (1.1)$$

Where R_{int} is the internal device resistivity, R_{load} is the load resistivity, V is the Seebeck voltage, S is the Seebeck coefficient, T_h and T_c are the temperature of the hot side and cold side, respectively. So, the power of the device can be obtained by

$$P = I^2 R_{load} = \frac{S^2(T_h-T_c)^2}{(R_{int}+R_{load})^2} R_{load} \text{.....} (1.2)$$

The load voltage V_{load} can be written as

$V_{load} = V - R_{int}I_{load}$……..(1.3)

$\frac{dP_{load}}{dI_{load}} = V - 2R_{int}I_{load}$……(1.4)

If equation (1.4) equals to 0, we can get the maximum generating power,

$I_{max} = \frac{V}{2R_{int}}$……(1.5)

When $R_{load} = R_{int}$, the maximum generating power can be calculated as

$P_{max} = \frac{V^2}{4R_{int}}$…….(1.6)

Over the past decade or so, there has been raising interest in the realm of thermoelectrics, promoted by the increasing desired for electronic refrigeration and power generation. (*24*) In traditional TEGs, p- or n- type TE legs are connected in series at electrical, and packaged with ceramic substrate. The TEGs have no moving parts with highly structural integration, functioning like engines. No moving parts means they are small and quite reliable. And this is why they are used in some spacecraft for wearable field. (*7, 8, 25, 26*)

2.2 Inorganic Thermoelectric Materials

Since the 1950s, state- of- the- art TE materials are inorganic conducting material, for example, Bi_2Te_3, SiGe and PbTe.(*27*) Some favourable characteristics for the next star generation should be: (1) heavy atoms in the unit cell; (2) atoms with lone-pair electrons; (3) weak, or losing bonding in atoms or layers, (3) complicated unit cell with large size, (4) distorted crystalline structure, (4) sophisticated Fermi surface.(*28*)

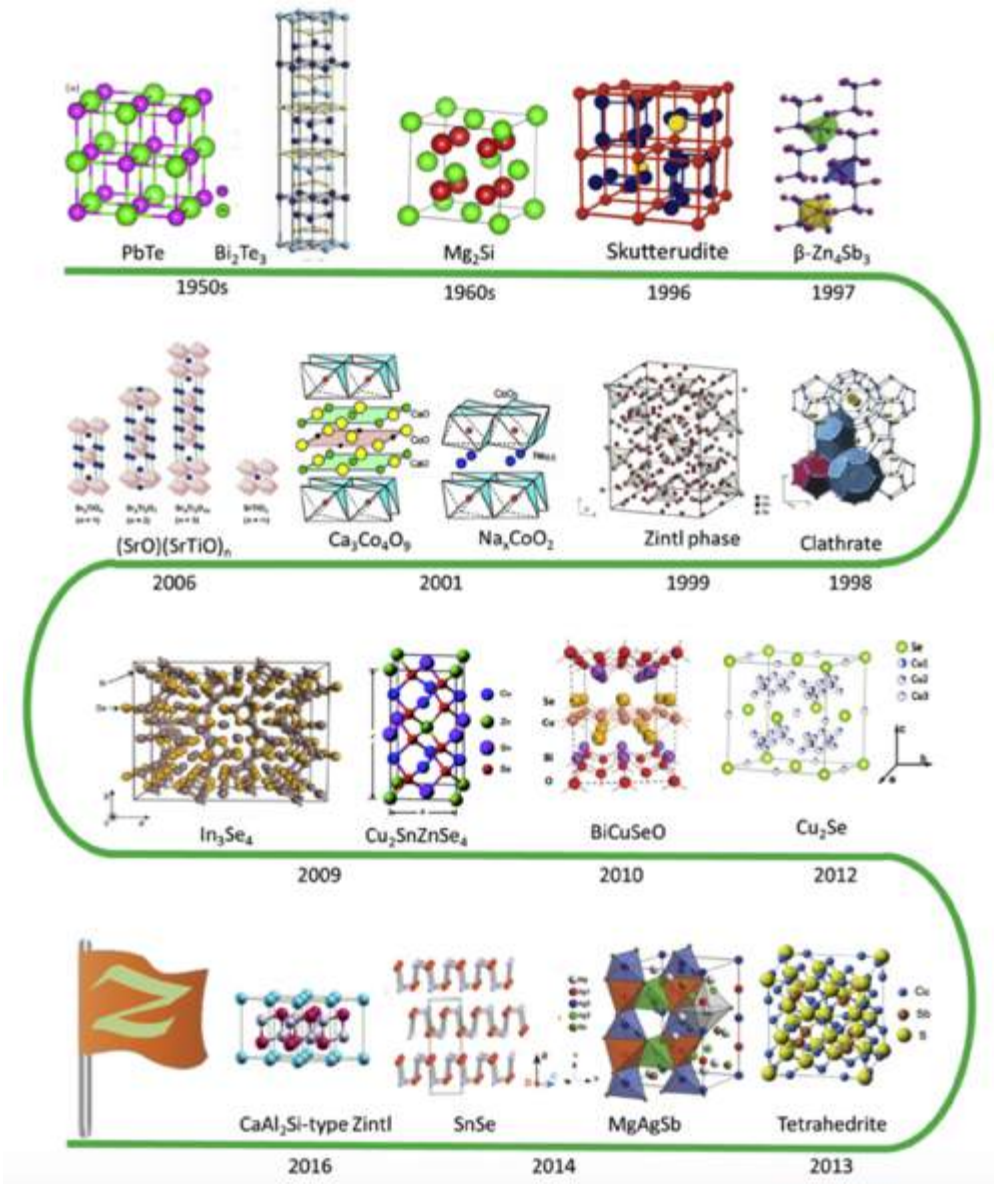

Figure 2.4 Timeline of selected TE materials(*28*)

The classical famous TE semiconductors, like Bi_2Te_3 and SnSe, are equipped with heavy atoms in their unit cells, which are conducive to the inferior thermal conduction. This can reduce the phonon transmission effectively. One popular candidate has been assigned to Bi_2Te_3, which have a layered structure. In this structure, the connection between Bi and Te is covalent bond, the weak link between neighbour Te layers is van der Waals bonding. That is to say, the lattice structure of Bi_2Te_3 consists of quintuple layers, which connected

with Van der Waals force, and each quintuple layer compose Te(1)-Bi-Te(2)-Bi-Te(1). The layered structural Bi_2Te_3 families and the heavy atoms in it are beneficial to the low κ. (*27*)

Glen A. Slack (1994), a pioneer in the study of heat conduction in solids, first proposed the Skutterudite compounds, which having a unconfined atom in the crystal cubic cell , could effectively weaken the lattice thermal conductivity.(*29*) This kind of materials usually have a large cavity which have the ability to support extensive metal atoms. Multitudinous elements have been placed in the cavities containing the alkaline earth metals, lanthanides, and numerous Group IV elements.(*30*) Assuming these atoms in the free connections are ponderous and considerably large, then the outcome disorder is larger, therefore, the thermal conductivity is lower.(*31*) Generally, the structure of skutterudites are cuboid with 32 atoms in one unit cell. We can regulate the heat capacity by improving phonon-scattering centres, that means, inserting atoms in the lacunal holes in crystal.(*32*) Moreover, (Co, Ni, Fe) $(P, Sb, As)_3$ type cubic skutterudite materials demonstrate a possibility for high TE efficiencies owing to their advanced electrical conductivity and high Seebeck coefficient.(*28*) Another category of high-temperature functioning semiconductors, for instance, clathrates, half-Heusler alloys, and complex chalcogenides are being studying. Unlike complex Skutterudite and Clathrate structures, the conventional PbTe type material or other complex compounds without cubic cage structures also draw attentions, as well as complicated chalcogenides and Zintl materials.

Stoichiometric copper selenide and nonstoichiometric $Cu_{2-x}Se$ are p-type materials that can be found in various crystallographic structures covering orthorhombic, monoclinic, and cubic. Notably, Cu_2Se was another favourable typical material for low κ_{lat} compounds with relatively small unit cell, in which the freedom Cu ions scattered the phonons and decreased heat capacity.(*33*) The location of “removable” Cu ion is changeable in the $CuSe_4$-

tetrahedron structure due to the local resonant bonds. The Cu_2Se is selected as the potential candidate for the device working in high temperature range of 600-1000 ^oC.(*33*) And the ZT value of Cu_2Se has been improved up to 1.6, which are comparable to the BiTe-based materials.(*34*) In addition, a phase transition happens at ~140°C, at which the low symmetry α-Cu_2Se phase transitions to the high-temperature β phase.(*35*) And β-phase Cu_2Se crystalized in layered cubic structure could very applicable have a high TE efficiency since the disordered lamella of monoatomic Se layers and free Cu atoms can reduce the thermal conductivity (*35*).

2.2 Flexible P-type Thermoelectric Materials

2.2.1 P-type graphene-based materials

Recently, graphene is proposed as one of ideal candidates for lightweight, high-strength functional material owing to its superior mechanical performance.(*36*) Moreover, graphene-like materials, for instance, exfoliated graphene, GO, and RGO, have been considered for electronic device fabrication.(*37-39*) As it known to all, graphene has ascendant charge transport properties (in excess of 105 cm^2 /(Vs)) which can be utilized for thermoelectric potential, but its thermoelectric performance is enslaved to extremely high thermal conductivity.(*36*) Thus, it is a big challenge here to improve the ZT of graphene-based materials. In order to improve Seebeck coefficient of graphene, nano-structuring is recognized as a valid way to decrease thermal conductivity by designing cavities in the crystal structure. This strategy will enhance phonon decentralization without remarkable scarifying the electronic conducting properties, leading to the high TE properties.(*40*)

For the flexible TEGs, substantial processes have also been reported to push forward its composite application, such as rGO / PANI,(*41*) rGO/ PEDOT:PSS. The tough p-p interaction between the graphene and aromatic groups of conducting polymers can promote electron shifting along the skeletons, therefore, increases the comprehensive electrical performance. Besides, the inherently favorable low heat conduction and thermal capacity of polymer will regulate the thermal conducting properties of graphene-based materials. Wang and co-workers(*42*) reported a mild and environmental friendly technique to prepare the rGO/PANI nano-particles with optimal thermoelectric performance. The modified PANI nano-particles are spread on the rGO plates regularly. The optimal electrical conductivity and ZT of the final products surprisingly achieved 1858.8S/m^{-1} and 4.23×10^{-4}, respectively. In the same vein, Kim *et al* (*43*) firstly demonstrated the PEDOT:PSS / graphene TE materials which shown the highly carrier mobility synthesized via *in situ* polymerization. During this fabricating process, PSS part used as a dispersing agent for the RGO and an excellent adulterant for the PEDOT. The most attracting part of this successful optimization is that PEDOT:PSS/graphene can be prepared by rGO directly, and no reduction treatment is needed. Because the poor conductivity of GO is not an ideal choice for the TE function. For the TE performance, PEDOT:PSS/graphene composites presented highly electrical property of 637 S/cm, when the graphene proportion reach about 3 wt.% in this material system. In addition, the PF was improved up to 45.68 μW/(m K) due to this increasing electrical conductivity.

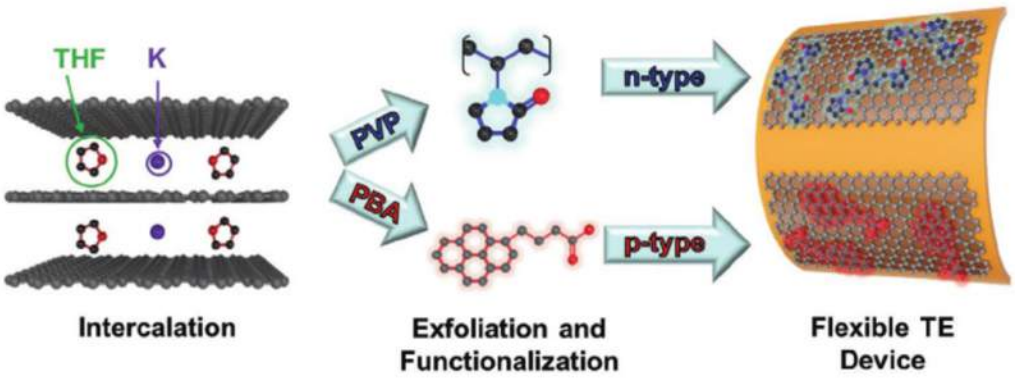

Figure 2.5 Illustrated scheme f p-type and n-type graphene films modified by changing the surfactant during exfoliation.

Travis G. Novak et al (*44*) presented the solution-phase exfoliated graphene for flexible thermoelectric applications. In this work, both extremely high electrical conductivity (3010 S cm^{-1}) and large Seebeck coefficients (53.1μV K^{-1}) can be achieved by altering the adsorbed surfactant during the insertion/ peeling-off procedure (pyrenebutyric acid for p-type). Additionally, the film also reveal amazing power factors. The room temperature power factor was above 600 μW m^{-1} K^{-2} at, almost ten times higher than the previous similar reported results.

In our group, Dr. Zeng(*10*) demonstrated a simultaneous reduction method to prepare large-sized rGO network structure assembly, supported by the PDMS. This reduced graphene oxide sample had a Seebeck coefficient of ~30.9 μV K, high electric conductivity of 2×10^4 S/m and low thermal conductivity of 7 W/mK, due to the improved carrier mobility as well as enhanced phonons scattering in the defects. Also, the boundary in the structure effectively decreased the mean phonon free path and the thermal conductivity. Furthermore, this FTE device was fabricated by assembling RGO film on poly multi-networks PDMS grids via 3D printing technology (Figure 2.6). This device exhibited an extraordinary power per mass of 57.33 mV/g when the temperature gradient is about 50 K. Finally, a wristband-

type FTEGs consisting of seven reduplicative cells produced a maximal power per mass of 4.19 μW/g. This 3D printed device presented an alternative way to wearable self-powering electronics.

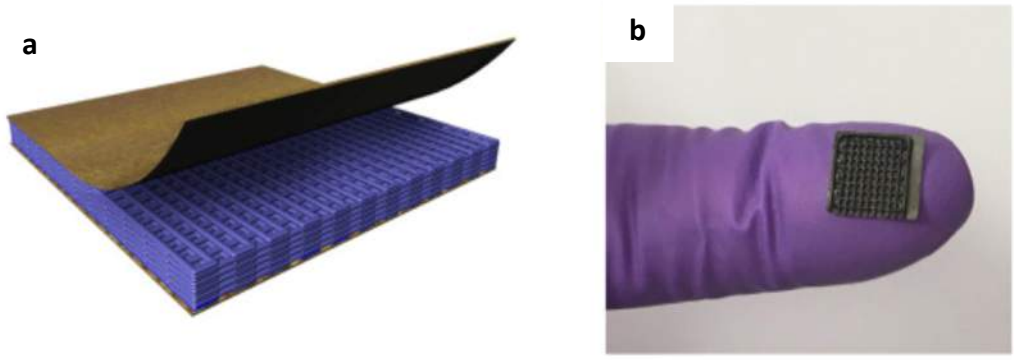

Figure 2.6 (a) Schematic image of 3D printed flexible TE generator, (b) 3D printed flexible TE generator without the top electrode.(*10*)

2.2.2 P-type organic conducting materials

Recently, increasing conducting polymers are well studied as ideal flexible materials for thermoelectric functions due to the rigidity of the inorganic materials. Conducting polymers including polyaniline (PANI), polythiophene (PTH), poly(3,4-ethylenedioxythiophene): poly(styrenesulfonate)/tosylate (PEDOT:PSS, PEDOT-Tos)$_3$, polyacetylene (PA), polypyrrole (PPY), polycarbazoles(PC), polyphenylenevinylene (PPV) and their descendants demonstrated a great possibility and definitely deserved further exploration.(*45*) For example, the performance of PA shown highly promotion doping with halogens chlorine, bromine or iodine and arsenic pentafluoride. For instance, nearly RT electrical conductivity of 20000 S/cm of independent PA thin film was achieved when doping with the iodine.

PANI is also favourable for the flexible TE materials due to its unique attributes, including the easy size engineering, facial adjustment of electrical properties with varied range and low costly fabrication. However, the power factor of PANI is poor due to the comparatively inferior electrical conducting performance and insufficient Seebeck coefficient. Moreover, its electrical conductivity depends upon its oxidation states which can convert from electrical insulation to the conduction with range from 10^{-7} S/cm to 300 S/cm and converting to the semiconducting nature. The Seebeck coefficient of PANI materials can be tuned via changing the dopants acid-base property or appendingg the organic/inorganic additives.(*46*) In most works, evidences confirm that the polymer chain of PANI normally varies from extending structure into the involved constructing, which affecting the degree of crystallinity, resulting the low the TE performance.

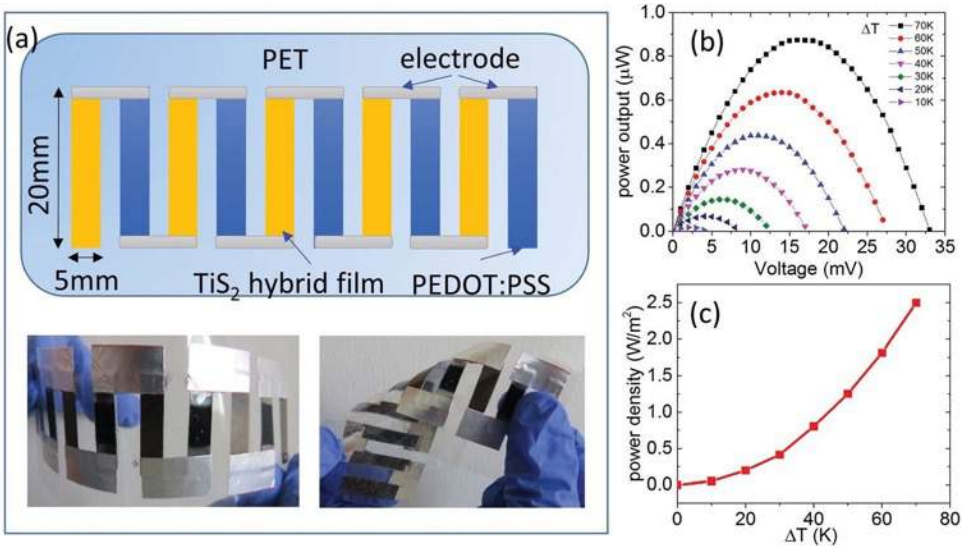

Figure 2.7 TE film with p-type PEDOT:PSS and n-type TiS_2/organic superlattice and their performance.

Beside these, the study on the TE property of PEDOT and its derivatives is also ongoing. However, the major challenge here is to find the effective methods to increase

thermoelectric efficiency of these materials. In order to deal with this problem, a deeper comprehending of charge transport mechanism in organic conducting polymers is needed. However, it is recognized as a big challenge owing to complex morphological and anisotropic physical properties in many respects. In spite of these difficulties, the seebeck coefficient and electrical performance of PEDOT based polymers can be adjusted by doping, which is recognised as a directly strategy to enhance the ZT of the PEDOT based polymers. Moreover, in order to obtain the high solution processability of the PEDOT materials, insulating counterpart PSS or tosylate counterions is usually designed to companies with the PEDOT, forming PEDOT:PSS or PEDOT:Tos.

2.2.3 P-type inorganic-organic materials

Inorganic-organic composites have been pervasively welcome and designing for TE application. Physical mixing, bottom-up preparing, and in-situ synthesis have been used to fabricated the TE composites which demonstrate TE escalation over their individual constituent, contributing to high efficiency and widely usage scenario. Most polymer materials are usually endowed with environmental friendly, sustainable quality, good tractability and flexibility. Cooperating the inorganic substances with various nanostructured particles or nano films can help to obtain higher properties of organic-inorganic hybrids. In most cases, incorporating conducting inorganic materials in conjugated polymers is expected to enhance conductive path, donation or extraction of carriers, structure confinement, or functionalized regulation.

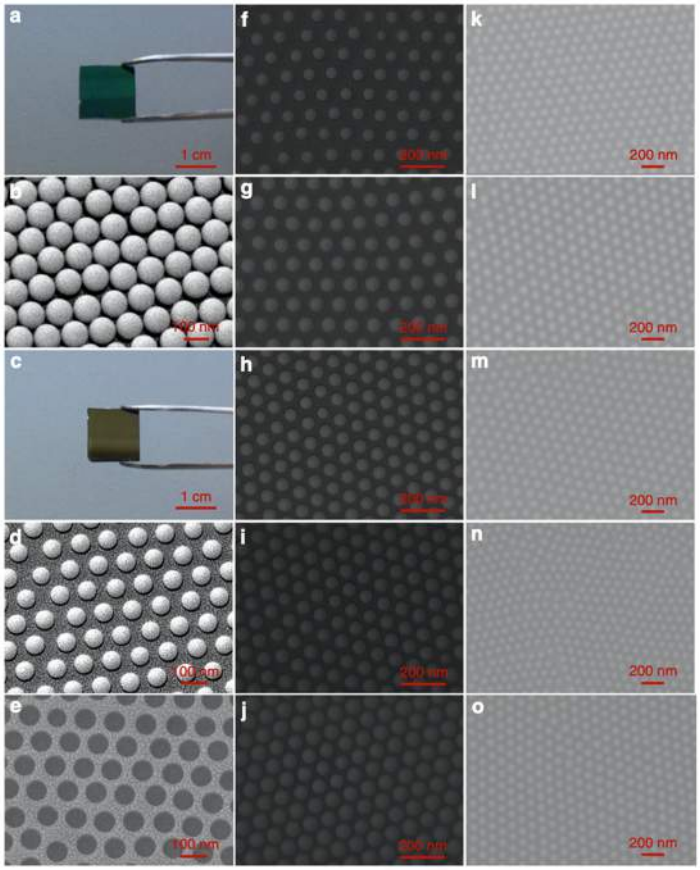

Figure 2.8 Photograph and SEM of polystyrene (PS) nanoballs coated on SiO_2/Si substrate. (*47*)

Liming Wang and co-workers reported a pliable composite composed periodic nanophase figured via lithography technology. (Figure 2.8) In this hybrid system, the dimension of PS nanospheres were varied from 10 to 100 nm.(*47*) In this system, the Bi_2Te_3 nanoballs were discretely dispersed in the continuous conductive polymer individually, the resulting hybrid film was uniform without aggregation. And the as-prepared film shown a highly PF of ~1350 μW m^{-1} K^{-2} , a decreasing in-plane thermal conductivity of 0.7 W m^{-1} K^{-1}. Finally, the calculated room temperature ZT was about 0.6, exceeding all organic materials and organic-inorganic hybrids reported so far. Moreover, after bending 100 cycles, the change

of thermoelectric performance of the film was neglectable, demonstrating superior mechanical flexibility.

Recently, Tian *et al* (*48*) have prepared PEDOT nanowires, and used Bi_2Te_3 powders filling with PEDOT nanowires to promote the power factor up to 9.06 $\mu W/(mK^2)$, which containing 10 wt% Bi_2Te_3 NWs at room temperature. Coincidentally, Wang(*47*) *et al* demonstrated flexible organic-inorganic hybrids in which varied dimension of Bi_2Te_3 nanoparticles were interruptedly dispersed in the patterned conducting polymer matrix. These hybrid matrix demonstrated superhigh power factor of ~1350 $\mu W/(mK^2)$ and fairly low thermal conductivity of ~0.7W/(mK), since the cyclical Bi_2Te_3 particles effectively decentralized phonons while continuous PEDOT:PSS matrix allowed electronic transport. The resulting ZT was about 0.6 at around room temperature, exceeding all reported flexible materials so far. Also, this material shown the superior mechanical flexibility after 100 bending duration without thermoelectric properties variation. In addition, Wan(*49*) *et al* demonstrated a strategy for an optimal carrier semiconductor superlattice of TiS_2 $[tetrabutylammonium]_x[hexylammonium]_y$ hybrid. In this hybrid, the organic parts were consisted of a disorder compound of tetrabutylammonium and hexylammonium. When the hybrids were heated at the propriate temperature, some lower boiling point hexylammonium molecules fled from the layers, which decreased the carrier concentration based on the electroneutrality. On the other hand, the higher boiling point of tetrabutylammonium molecules could hold the superlattice structure. Thus, the reduction of carrier concentration leaded to a high Seebeck coefficient and high power factor of 904 $\mu W/(mK^2)$ at 300 K, comparable with the performance of conventional inorganic thermoelectric materials.

2.4 Flexible N-type Thermoelectric Materials

2.4.1 N-type graphene-based materials

Graphene is a 2D material with monoatomic layer thickness. This material has special layer crystal material and unique physical and chemical properties. Substantial studies show that the graphene possess superior electrical performance, super large specific surface area and various boundary structures which are benefit to the coordinated regulation between thermal and electrical performance.(*50*) As discussed in the section 2.31., Travis G. Novak and co-workers(*44*) fabricated the p-type graphene films for flexible TEGs. Coincidentally, in their work, n-type flexible graphene film was also prepared by changing the adsorbed surfactant polyvinylpyrrolidone. The thermoelectric properties of the films are remarkable with a Seebeck coefficient of -45.5 μV K^{-1}, highly electrical conductivity of 3010 S cm^{-1}, and enhanced power factors of 621 μW m^{-1} K^{-2}. A complete all-graphene thermoelectric device is constructed, generating several nW under a given temperature difference of 50 K.

One problem of graphene or rGO based materials is irreversible aggregation, forming the wrinkle structure during fabricating process. This folding will damage the advantage of laminated structure, therefore, hard to modify properties. For the GO, unlike graphene or rGO, the hydrophilic groups (-OH, -C(O)C-, -C＝O, -COOH, -COO-) boost the film deposition via electrostatic or hydrogen bonding. An instance, air-stable n-type DWNT(double-walled carbon nanotubes)-PEI(polyethylenimine)/GO is fabricated by Chungyeon Cho and co-workers.(*51*) This film was prepared by layer-by-layer assembling, alternately exposing Si-wafers substrate to the DWNT-PEI and GO mixtures. The film grow up gradually followed by the double-walled CNTs-PEI/GO sequence,

resulting the exceptional electrical conductivity of 27.3 S cm^{-1} and a Seebeck coefficient of -30 μV K^{-1}, a power factor of 2.5 μW m^{-1} K^{-2}. The superior performance of these n-type nanocomposites can be allied to the following reasons: 1) stabilizer PEI providing the electrons, 2) the effective reduction from GO to rGO, and 3) the thermal treatments lead to three dimensional framework formation. PEI acted as the stabilizer to form 3D network. 4) the electron donation to convert the type of carriers from holes to electrons. The evidence of Fermi level shift near to the LUMO.

2.4.2 N-type organic conducting materials

While p-type flexible organic conducting TE materials have witnessed rapid advancement, the developing progress of n-type ones still lags behind due to the challenges in n-type regulating. As we all know, a considerable amount of n-type conducting polymers are unstable when exposing in air condition, severely affecting the adhibition of semiconducting polymers in practice. The conducting polymers are liable to oxidize due to the lessened polymer chain and counter-cations. Remarkable efforts are devoted to solve this essential problem.

One typical kind of these n-type flexible examples are doped-conjugated polymers. Comparing with p-type polymers, which up to 1000 S cm^{-1} of electricity are obtained in these materials, whereas only few n-type ones,(*52*) limited values of 1 S cm^{-1} are improved. However, this performance only could maintain at oxygen-free environment. The latest reported n-type N-DMBI ((4-(1,3-dimethyl-2,3-dihydro-1Hbenzoimidazol-2-yl)phenyl)dimethylamine) doped- P(NDIOD-T2) (poly((N,N′-bis(2-octyldodecyl)-naphthalene-1,4,5,8-bis(dicarboximide)-2,6-diyl)-alt-5,5′-(2,20 bithiophene)) is found to

have a high Seebeck coefficient of -850 μV K^{-1}, while have a low electrical conductivity of 8×10^{-3} S cm^{-1}.(*53*) Thus, the N-DMBI doped P(NDI2OD-T2) sample displayed a limited PF of 0.6 μW $m^{-1}K^{-2}$.(*53*) Despite some conducting polymers show considerable Seebeck coefficients to that of inorganic semiconductors, the fatal electrical performance still need to strengthen.(*53-56*)

Another well-studied n-type conducting polymer are the benzodifurandione-phenylenevinylene (BDPPV) derivatives, which the lowest unoccupied molecular orbital (LUMO) had been adjusted to as low as -4.0 eV, presenting the most electron-deficient conjugated polymers. Pei and co-workers prepared the halogen-substituted polymers ClBDPPV (LUMO: -4.30 eV) and FBDPPV (LUMO: -4.17eV), doping with N-DMBI then spin casting on the glass substrates as the thin films. In these systems, the excess N-DMBI molecules acted as the impurities.(*56*) However, because of the intrinsic insulating property, the electricity of the N-DMBI-doped ClBDPPV and N-DMBI-doped FBDPPV film were reduced with the increasing dopant concentration. The electrical conductivity of FBDPPV film was 14 S cm^{-1}, and the maximal PF was 28 μW m^{-1} K^{-2}. But these indexes only kept stable under N_2 atmosphere. For the air-stable issue, Katz and co-workers(*57*) fabricated the 25 mol% TBAF-doped CIBDPPV thin film with 130 °C annealing treatment, showing the high electrical conductivity of 0.62 S cm^{-1} when the sample was fresh. Furthermore, after exposing in the air for about 7 days, the performance of this product was still maintained at the same order of magnitude. Correspondingly, this air-stable TBAF-doped CIBDPPV thin film demonstrated a Seebeck coefficient of -99 μV K^{-1}, a PF of 0.63 μW m^{-1} K^{-2}.

2.4.3 N-type inorganic-organic materials

Another important class of the elastic n-type TE materials are polymer-based composites. PEDOT:PSS is one of the most promising candidates for n-type thermoelectric because of environmental friendly, and structure flexibility. To our best knowledge, there is no reported compete n-type polymer so far. Katz et al.(*58*) incorporated both p- and n-type Bi_2Te_3 ball-milled powders with PEDOT:PS S(commercialized PEDOT:PSS products CLEVIOS PH1000 and FE-T), respectively, achieving enhanced power factor of around 47 $\mu Wm^{-1} K^{-2}$ and 30 $\mu Wm^{-1} K^{-2}$ for both composites.(*58*) Cho *et al* reported screen-printed PEDOT:PSS-coated Bi_2Te_3 (n-type) film, with enhanced flexibility and thermoelectric property. The slightly enhanced Seebeck coefficient attained -137mV/K and the final ZT reached up to 0.16.(*59*)

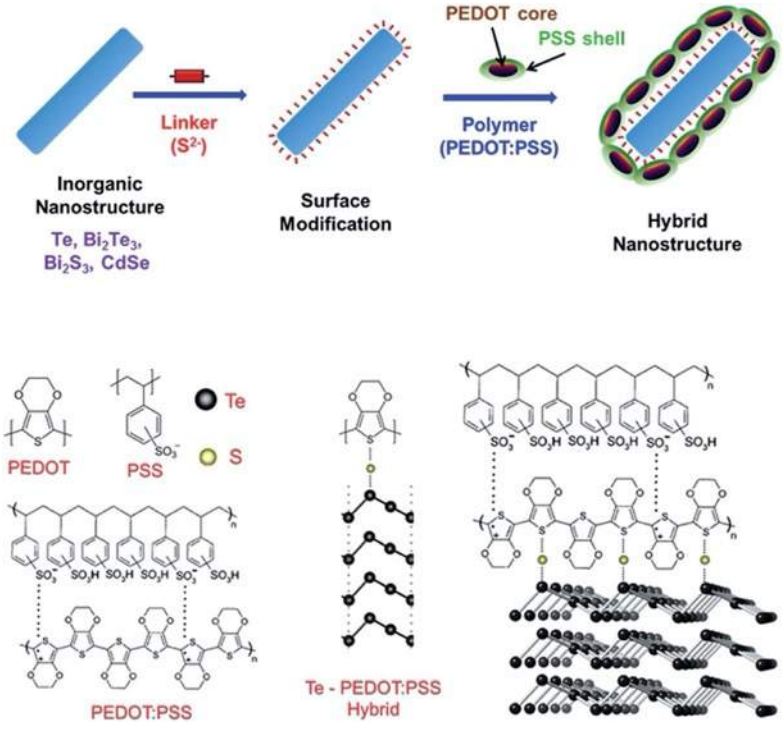

Figure 2.9 Illustration of inorganic nanostructure-PEDOT:PSS hybrids. A representative hybrid comprising of tellurium and PEDOT:PSS is demonstrated in the scheme.(*60*)

Urban and co-workers prepared p- and n-type flexible TE materials based on the PEDOT:PSS, exhibiting outstanding properties with optimizing fabrication strategy. Different from the physical mixture, these samples were synthesized with a designed lego-like approach. As shown in Figure 2.9, semiconductor telluride was linked to PEDOT:PSS through interface engineering strategy, resulting a robust TE-PEDOT:PSS hybrid. This strong structure interaction induce the highly electrical performance when comparing with their individual components.

2.5 Flexible Thermoelectric Generators

A practical thermoelectric device consists of p/n-pairs, closed with ceramic substrates at top and bottom ends. For the FTEGs, the structures have more variety owing to the unique nature. In other words, the systems are considered to be ergodic.

2.5.1 Thermal resistance and electronic connectors

Thermal performance is one of the most critical factors in TE performance. As we mentioned above, for thermoelectric materials, in order to achieve high ZT values, high seebeck coefficient and high electricity are required, whilst low thermal conductivity is needed. Recent studies have witnessed momentous development on heat transfer issues of TE field(*61-63*). For the materials, great efforts have been invested to reduce the material thermal conducting ability. For traditional TE materials, there are two routes, alloying(*64*) and introducing phonon rattlers(*24*), used to lower thermal conductivity by atomic disorder. Nano-structuring is another direction to enhance ZT. In spite of robust performance of TE materials, there are still time-lag remained here to covert these materials in practice. Since

heat loss in system hinder not exclusively the efficiency but also the dependability of devices. In electronic fabrication, one should emphasis heat conduction existed in whole thermoelectric device. Here is the standard structure of thermoelectric devices. Take a little bit closer observation to the contact area between device surface and heat/ cold side, some air gaps are observed between this contact region, which will impede the heat flux flow in it. Therefore, the device could not large temperature difference for high power output.(*65*) For the sake of the reduced thermal contact resistance between electronic packaging and a heat sink, a variety of thermal filling glues have been applied. For example, metallic conductive adhesive, phase-change materials(*66*) or commercial conducting tapes are widely used. Both these materials share the same idea, reducing or eliminating the porous insulation regions by filling the uneven surfaces.

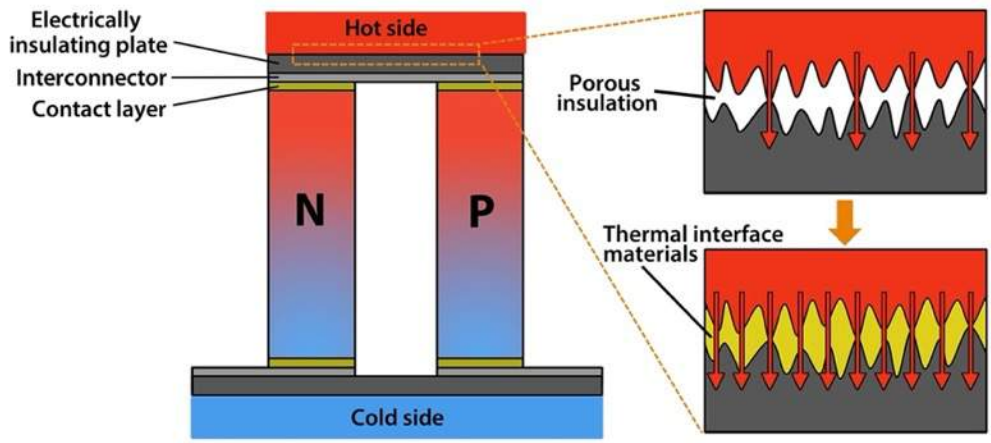

Figure 2.10 Thermal contact resistance of thermoelectric system and typical interface layers between the thermoelectric pellet and interconnector.

2.5.2 Development of flexible thermoelectric generators

Self-powering wearable electronic devices are recognized as one of the staple strategies to prospect smart portable electronic facilities. Minimalist and integrated designs of electronics facilitate the development of wearable TEGs and medical implantable devices. Battery, as the traditional powering way, need the periodic replacement and maintain which are inconvenience and cost. Therefore, the idea of wearable TEGs seems exciting and potential to recover waste human heat, realizing self-powering function. For the structures, there are two major prototypes, namely, sandwich structure, and film structure.

Recently, screen printing strategy have been used in minimalist and integrated electronic designs, including FTEGs. Compared with other techniques, like deposition, photolithography, or patterning, the printing strategy is one of the favorable technique for the flexible devices fabrication because of the material saving, one-shot synthesis, structural flexibility. In addition, screen printing not only can used on the flat, but also can applied on the special structure surface. Cho's group has proposed several flyweight FTEGs.(*15*) In their works, Bi_2Te_3 and Sb_2Te_3 were used to make printing pastes and screen printed on glass woven fabrics, followed by annealing at 530 ^oC in N_2 atmosphere for crystallization and thickening of the TE materials. Although glass fibers allow this annealing temperature, they are brittle, easily break and impose potential hazards to human thus not suitable for wearable applications. Furthermore, the TE performance was not good either. The absolute Seebeck coefficients of these TE materials containing Bi_2Te_3 and Sb_2Te_3 were 141 μV/K and 98 μV/K, about half of those for the bulk TE materials, respectively. Moreover, the three-layer sandwiched-like structure of FTEG have limited functional temperature differences. To our best knowledge, the temperature difference range of these FTEGs is from 5 to 50 K,(*67-69*) which hinders their practical applications.

Alternatively, FTEG consisted of TE legs in a fiber- or strip-shaped film may provide a solution.(*70, 71*) A thin film TE devices incorporated of n-type and p-type TE nanoparticles by inject printing was reported to be coiled up without obvious crack or peeling.[11] However, for wearable applications, this type of FTEG cannot endure the continued movement of the body although it can function under large temperature difference range of 70 K.

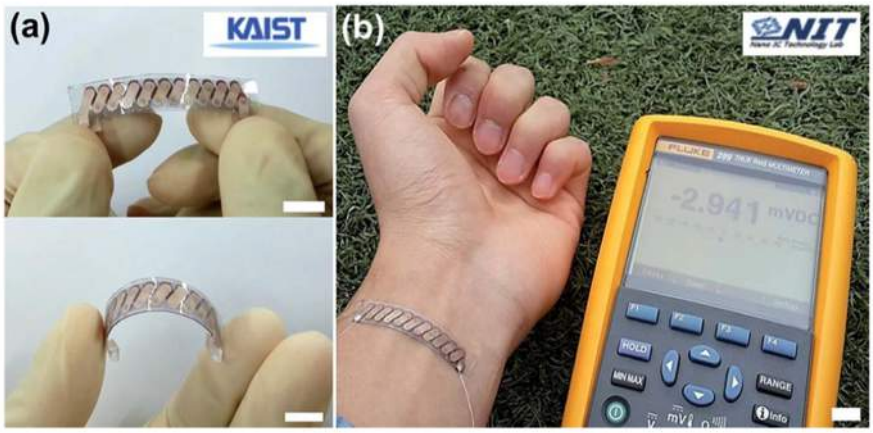

Figure 2.11 (a) Photos of the thermoelectric bracelet, Scale bar, 1 cm.(*15*)

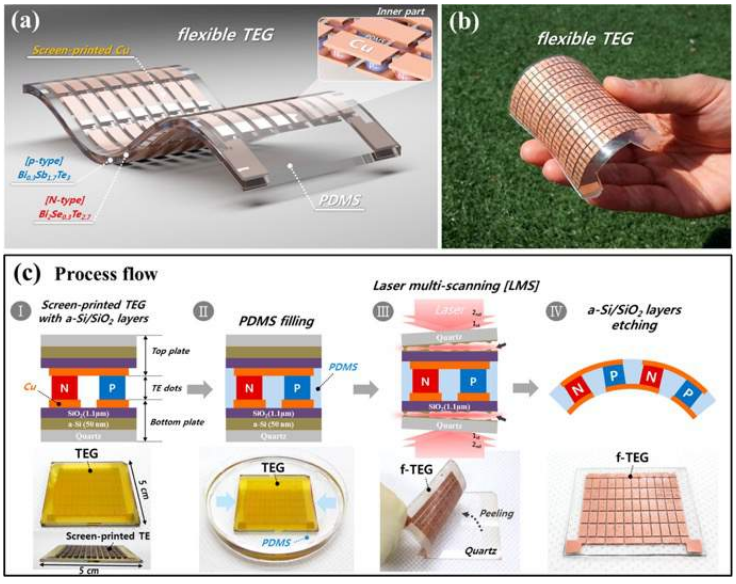

Figure 2.12 (a,b) Schematic illustration and actual model of f-TEG. (c) Process flow of a freestanding f-TEG.(*72*)

Lately, Cho's group prepared a FTEG n a SiO_2/a-Si/quartz through the screen printing method as well. In initial process, the device was packed with rigid quartz substrate, which was skilfully departed in the following laser multi-scanning lift-off process.(*72*) This freestanding FTEG is lightweight and bendable. In this sense, screen printing technology is available to various substrates, benefiting to the FTEGs fabrication.

Similarly, Son's group also used printing technique to fabricate flexible or shape-conformable TEGs lately.(*16, 17*) In their study, the group presented the new type of high-performance flexible TE materials and prototyped into different structure FETGs designs. Both n-type and p-type materials were newly explored with shape-designability and geometrically compatibility that could be directly painted on any curve surface. In their previous work, TE materials was painted on the bullet base to generate power. Moreover, they then used the same ink employing 3D printing technique to produce conformal cylindrical TEG in which series of half rings were connected by the electrodes. Clever design let the hot water flow past the tube below as the heat source. Three-dimensional printed materials with different geometric construction presented coessential TE performances, and their comparable dimensionless figure-of-merit can reach as high as 0.9 (p-type) and 0.6 (n-type), respectively. They also created a theoretical model to simulate the temperature and electrical potential distributing in the pipe TEGs. The calculated results indicated that the performance of the conformal TE device was superior than that of traditional flat geometry ones.

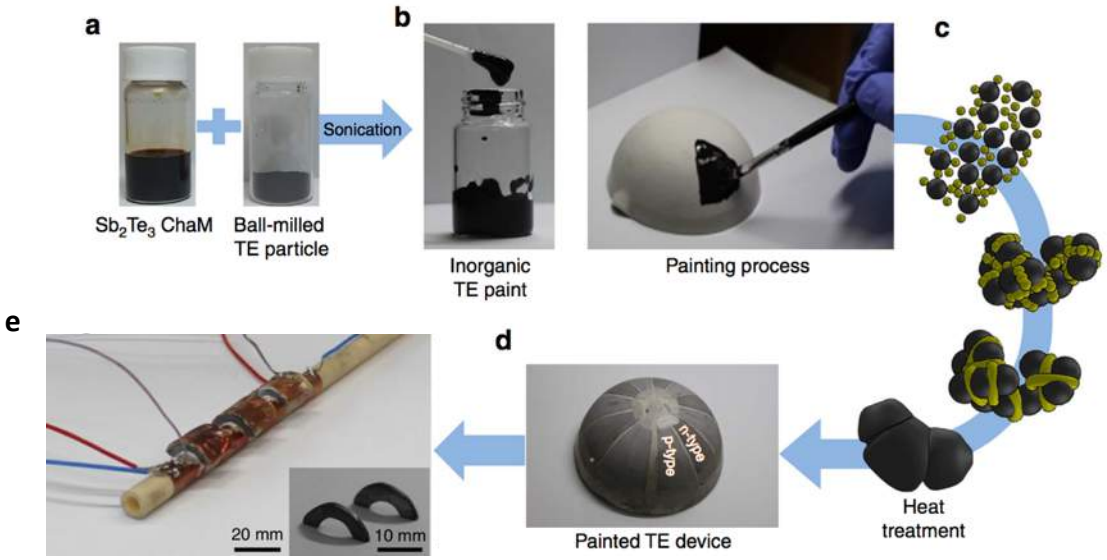

Figure 2.13 (a-e) Schematic illustrating the process flow of painted or printed TE devices with Bi_2Te_3-based pastes.(*16, 17*)

2.5 Summary

After a brief introduction to the thermoelectric effect, the traditional and flexible TE materials are also reviewed, followed by electrode connectors and printing technique for FTEGs, as well as the development of FTEGs. To our best knowledge, despite of the high performance of the traditional inorganic materials, polymer materials demonstrate outstanding flexibility which can meet the FTEGs design and fabrication. Preparing superior flexible TE materials for the FTEGs remain challenge with limited progress reviewed above. In addition, thermal performance is one of the most critical factors in TE performance. Compared to rapid development of TE materials, the progress of FTEGs is quite slow. Most of the FTEGs are still made by inorganic materials. Many obstacles such as low efficiency, structure defect need to be overcome. Thus, more studies on the FTEGs based on inorganic-organic materials are needed.

Chapter 3 THERMOELECTRIC PERFORMANCE OF P- BISMUTH TELLURIDE/PEDOT:PSS COMPOSITES

3.1 Introduction

In a recent FTEG work, (*15*) Bi_2Te_3 and Sb_2Te_3 were used to make printing pastes that were screen printed on glass woven fabrics, followed by annealing at 530 ^oC in N_2 atmosphere for crystallization and thickening. Although glass fibers allow this annealing temperature, they are brittle, easily break and impose potential hazards to human thus not suitable for wearable applications. Furthermore, the TE performance was not good either. The absolute Seebeck coefficients of these TE materials were 141 μV/K (p-type) and 98 μV/K (n-type), respectively about half of those for the bulk TE materials, respectively. Moreover, the three-layer sandwiched-like structure of FTEG have limited functional temperature differences. To our best knowledge, the temperature difference range of these FTEGs is from 5 to 50 K,(*73*) which hinders their practical applications. Alternatively, FTEG consisted of TE legs in a fiber- or strip-shaped film may provide a solution. A thin film TE devices incorporated of n-type and p-type TE nanoparticles by inject printing was reported to be coiled up without obvious crack or peeling observed.(*74*) However, for wearable applications, this type of FTEG cannot endure the continued movement of the body although it can function under a large temperature difference range of 70 K.

Bi_xTe_y-(*75, 76*) and Sb_xTe_y-(*77, 78*) type materials have excellent room temperature TE performance, potentially suitable for FTEGs for wearable applications. However, these materials are rigid, hard, incapable of enduring long-term dynamic deformation and normally require high temperature treatments.(*78*) Thus, it is very hard to incorporate these solid inorganic materials to achieve fine TE device with flexibility. Incorporating inorganic particles into a conducting polymer matrix is an ideal strategy to obtain both TE and mechanical performance required by FTEGs. Furthermore, this facile synthesis inorganic-polymer strategy is consistent with requirements of cost-effective low- or room-temperature printing or coating due to the solution processibility. The favourable organic or polymer TE materials include poly(3,4-ethylenedioxythiophene)-poly (styrene sulfonate) (PEDOT:PSS),(*79-81*) polyaniline (PANI),(*82, 83*) and others.(*28*) One key advantage of this class of materials is their amenability to solution processing at low- or room-temperature. In this work, PEDOT/Bi_2Te_3 hybrid was selected as an example for systematic study. The superior performance of PEDOT:PSS and Bi_2Te_3 and similar work functions of these two materials together form the carrier supernal pathway through the interfances. (*47, 84, 85*)

Three dimensional (3D) disperse printing has been intensively explored to rapidly fabricate precise structure devices for energy storage,(*86*) tissue engineering,(*87*) 3D evaporators,(*88*) and functional hydrogels.(*89*) 3D printing technique was used to fabricate cylindrical rigid TEGs, which could conform to any shape of heat sources. Yet, the technique has not been widely explored in fabrication of FTEGs.

Based on these considerations, a new strategy is proposed and investigated by employing Bi_2Te_3/PEDOT:PSS composite as TE materials for FTEGs. Hybrid ink paste containing Bi_2Te_3 particles and PEDOT:PSS will be synthesized and used for disperse printing on an

elastomer substrate or a paper substrate at room temperature, followed by annealing process at moderate temperature. The structure and thermoelectric properties of the composites will be investigated for screen printing and 3D disperse printing of FTEG devices, which will be presented in Chapter 5.

3.2 Experimental

3.2.1 Materials

p-type Bi_2Te_3, (99.99%, KYD Materials), poly(3,4-ethylenedioxythiophene) polystyrene sulfonate (PEDOT:PSS, 5.0 wt. %, Sigma Aldrich), dimethyl sulfoxide (DMSO, 99.9% %, VWR Chemicals), ethanol (EtOH, 99.8%, VWR Chemicals), α-terpineol (96%, Alfa Aesar), isopropanol (AR, UNI-CHEM), neutral silicone (100%, Ele-wintex), tetrahydrofuran (99.9%, VWR Chemicals), silver conductive paste (75%, Sigma Aldrich), were purchased commercially and used without any further purification.

3.2.2 Preparation of p-Bi_2Te_3/PEDOT:PSS hybrid ink paste

The TE ink was prepared based on a well-dispersed mixture of p-Bi_2Te_3 and PEDOT:PSS, with addition of DMSO, isopropanol and α-terpineol. During the mixing process p-Bi_2Te_3 particles and PEDOT:PSS were immersed into organic solvent, forming a homogeneous paste. The ink paste consists of 3.07 g p-type Bi_2Te_3, 0.4 g DMSO, 2.0 g PEDOT:PSS, 0.43 g isopropanol and 0.46 g α-terpineol. The pastes were mixed for 12 h using a magnetic stirrer. The solvent maintained the viscosity of ink paste at a desired level and used to the printing. The viscosity of the paste was measured by DV-E Viscometer, Brookfield.

3.2.3 Sample preparation for characterization and tests of TE properties

All the p-Bi_2Te_3, p-Bi_2Te_3/PEDOT:PSS samples were prepared as the pellets. Then the pellet samples were annlead at 423 K, 593 K, 623 K, 673 K using the tube furnace under argon atmosphere for 3 h before the measurements.

3.2.4 Structural characterization

The morphology of TE materials was characterized by scanning electron microscopy (Tescan VEGA3). Raman spectra measurements were carried out on a Raman spectrometer (BaySpec's Nomadic™ Raman microscope 3-in-1, λ_{exc}=532 nm), FT-IR spectra of TE materials were recorded on Perkin Elmer Spectrum 100 FT-IR and FT-IR Spectrometers. The crystalline structure of TE materials was obtained from Rigaku Smart Lab with Cu Kα radiation (λ = 1.5406 Å). Thermal stability analysis of TE materials was conducted on thermogravimetric analyzer (METTLER TOLEDO Thermal Analysis, STARe system) in an atmosphere of nitrogen. X-ray photoelectron spectrometry (XPS) analysis was measured by Physical Electronics 5600 multi-technique system, using monochromatic Al-alpha source.

3.2.5 Evaluation of TE performance

The thermal stability of the samples was examined by Thermo-gravimetric analysis (TGA), under anitrogen atmosphere created by fluxing 50 ml/min of N_2 from 323K to 1200K at the heating rate of 10K/min..

Seebeck coefficient and electrical conductivity of the TE films were obtained by SBA 458 Nemesis® measurement Setup (NETZSCH Group, German). The thermal conductivity was measured by laser flash apparatus (LFA 457 MicroFlash®, NETZSCH Group,

German). Hall effect of TE samples were tested by pressure-assisted molybdenum contacts with 1T magnet, employing the van der Pauw technique.(*90*)

3.3. Results and Discussion

3.3.1 Formation of Bi_2Te_3/PEDOT:PSS composite

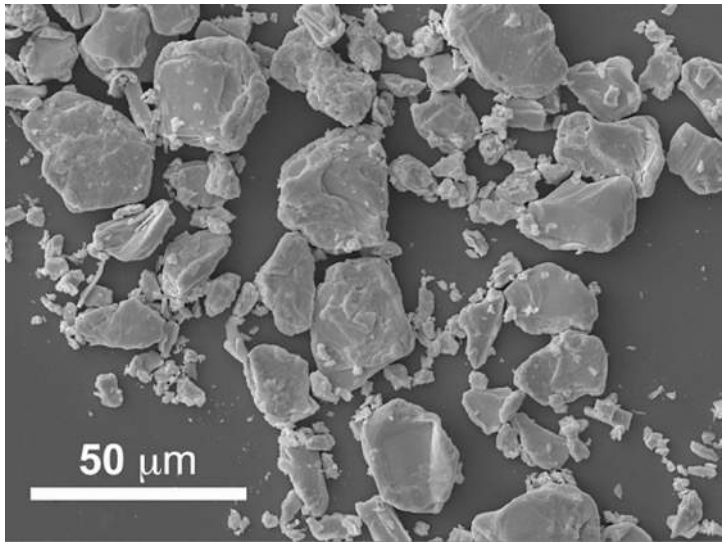

Figure 3.1 SEM Image of p-type Bi_2Te_3.

In this work, the used p-type Bi_2Te_3 ($Bi_{0.52}$ $Sb_{1.48}Te_3$) particles are of uneven size. The average size is roughly 20 μm (**Figure 3.1**). The small granular p-Bi_2Te_3 are filled into the interspace of p-Bi_2Te_3 large particles, generating compact constituents. The constituent components serve different purposes: p-Bi_2Te_3 particles and PEDOT:PSS are engineered for TE function; DMSO is added to increase the electrical conductivity of PEDOT:PSS; Isopropanol and α-terpineol are used to adjust the paste viscosity.

Figure 3.2 Photograph of p-type Bi_2Te_3/PEDOT:PSS ink.

The p-Bi_2Te_3/PEDOT:PSS composite was formed from its precursor as a printing paste ink, then activated followed by solidification and annealing at moderate temperature. This viscoelastic ink is homogeneous, as shown in **Figure 3.2**. The viscosity of this ink is 32000 mPa·s. The major challenge for our strategy is to adjust the rheological property of the ink to guarantee the uniformity of extrusion structure without pinhead clogging. The rheological parameters of the TE materials significantly affect the following printing structures. This appropriate viscosity of p-Bi_2Te_3/PEDOT:PSS paste ink facilitates a good processability in continuous 3D disperse printing technique.

3.3.2 p-Bi_2Te_3/PEDOT:PSS composite characterization

Figure 3.3-3.5 provide the characterization results on composition of the p-Bi_2Te_3, PEDOT:PSS, p-Bi_2Te_3/PEDOT:PSS samples, respectively. As shown in **Figure 3.3**, the X-ray diffraction (XRD) spectra of p-Bi_2Te_3 particles, PEDOT:PSS film, and p-Bi_2Te_3 /PEDOT:PSS composite film indicate that the typical XRD pattern of the composite is in accordance with p-Bi_2Te_3 particles accompanied by spikes of amorphous matrix, which is due to the PEDOT:PSS. The Raman spectra of PEDOT:PSS film (bottom curve) and p-Bi_2Te_3/PEDOT:PSS film annealed at 423K (top curve), as shown in **Figure3.4**, illustrate

the band observed between 1300 and 1600 cm^{-1} have been accounted to PEDOT. The C–C stretching vibration of a quinoid structure can be observed at 1432, 1435 cm^{-1} in thiophene rings.(*91*) In the DMSO doped p-Bi_2Te_3/PEDOT:PSS composite film sample, the benzoid signal is suppressed while the peak is shifted to the red region slightly (top curve vs. bottom curve), illustrating the conversion from a coil shape to an entangled linear shape of PEDOT chains. This conformational change has a positive effect on electrical conductivity since linear molecular chain reduces the carrier jumping energy, promoting the carriers shifting through the p-conjugated PEDOT skeletons. Evolution of a double peak at 1578 cm^{-1} further indicates de-doping function of PEDOT:PSS, demonstrating that there is a charge transfer between p-Bi_2Te_3 and PEDOT:PSS.(*92*) Furthermore, the PEDOT:PSS can reduce the oxidization of the Bi_2Te_3 as well for XPS spectra, displaying the interaction between p-Bi_2Te_3 and PEDOT:PSS.

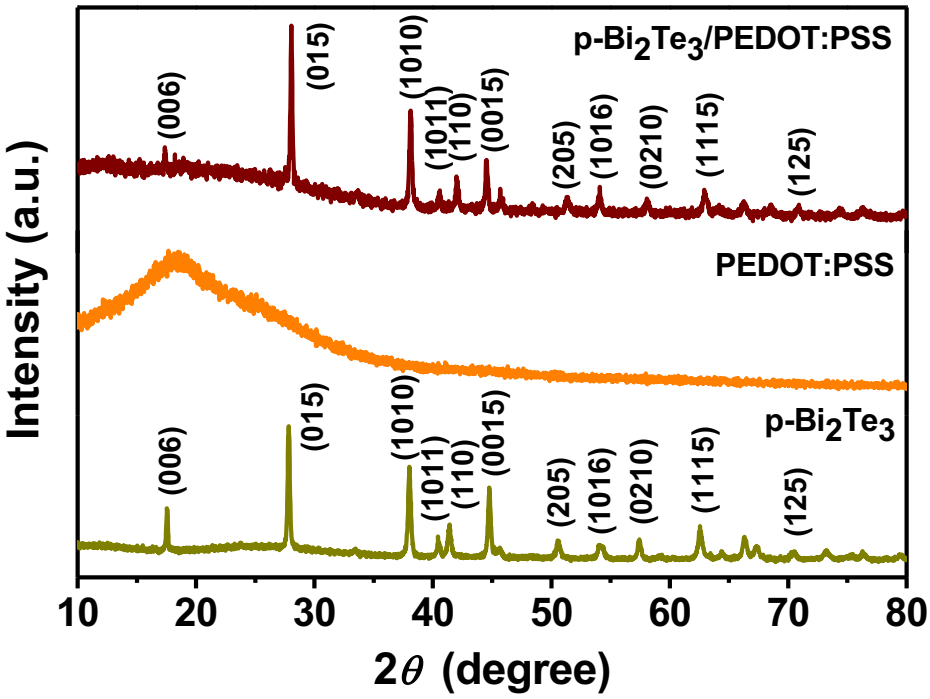

Figure 3.3 XRD spectra of p-Bi_2Te_3, PEDOT:PSS, p-Bi_2Te_3/PEDOT:PSS, respectively.

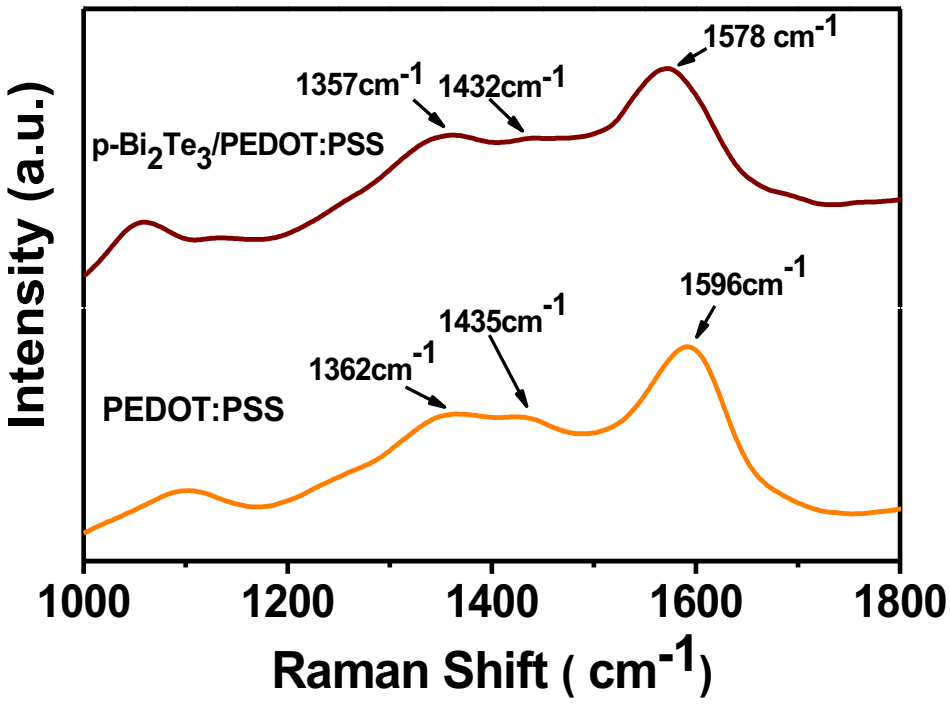

Figure 3.4 Raman spectra of PEDOT:PSS (bottom curve) and p-Bi_2Te_3/PEDOT:PSS (top curve).

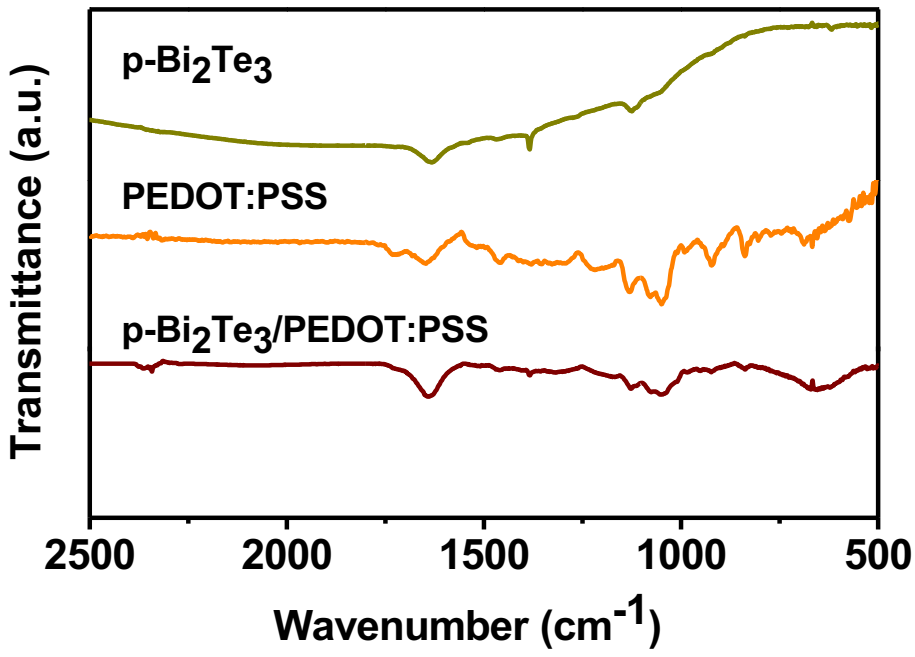

Figure 3.5 FTIR spectra of Bi_2Te_3, PEDOT:PSS, and Bi_2Te_3/PEDOT:PSS, respectively.

The infrared absorption of PEDOT:PSS can be clearly seen in FTIR spectrum of p-Bi_2Te_3 /PEDOT:PSS composite (**Figure 3.5**). The peak at 985 cm^{-1} refers to the C-S bond oscillations in the thiophene rings of PEDOT. Another two peaks of 1051 cm^{-1} and 1230 cm^{-1} are accounted to the extending vibration of the C-O=C in PEDOT.(*93*) Additionally, the broad peak positioned at 1213 cm^{-1} show the symmetric oscillation of the -SO_3 group in PSS. The evolution of 1643 cm^{-1} may be ascribed to skeletal oscillation C=C bonds stemmed from aromatic structure. Another weaken signal positioned at 839 cm^{-1} accounts to C-H bonds from benzene ring of PSS. Meanwhile, characteristic peaks of both PEDOT and PSS are observed in Bi_2Te_3/PEDOT:PSS composite. The peak at 1635 cm^{-1} belongs to skeletal oscillation of stressed C=C linkage stemmed from aromatic structure in PSS. Moreover, the summit at 1050 cm^{-1} ascribes to symmetric oscillation of C-O=C bonds in PEDOT.(*93*)

3.3.3 Thermal treatment of p-Bi_2Te_3/PEDOT:PSS composites

Figure 3.6 shows the weight variation of these three samples, pure p- Bi_2Te_3, PEDOT/PSS and p-Bi_2Te_3/ PEDOT/PSS specimens upon heating. For the PEDOT:PSS curved line, in the initial stage up to 473 K owing to the losing of water, then following the disintegration of organic residual.(*94*) The de-composition of PSS starts from 538 K ends at 593 K with a weight loss of 25 wt%. The sulfonate groups split at this intermediate temperature range. The last decomposition begins with 623 K and goes t 873K with the weight loss of 10 wt%, is ascribed to rupture of main polymer chain, PEDOT.(*94*) It is worth noting that the residual is about 58%. For the p-Bi_2Te_3/ PEDOT/PSS sample, the composite shows little weight loss below 523 K because of the organic binder residual. Above 533 K, a slightly weight loss starting with 450K, and this loss continues to increase with the temperature

goes to 800K. The sulfonate groups and PEDOT split at this intermediate temperature range.Then the sample comes in the platform till 900K. After 973K, the sample of Bi_2Te_3 melt down. For pure Bi_2Te_3, the appropriate annealing treatment should be below 900K.(*95*)

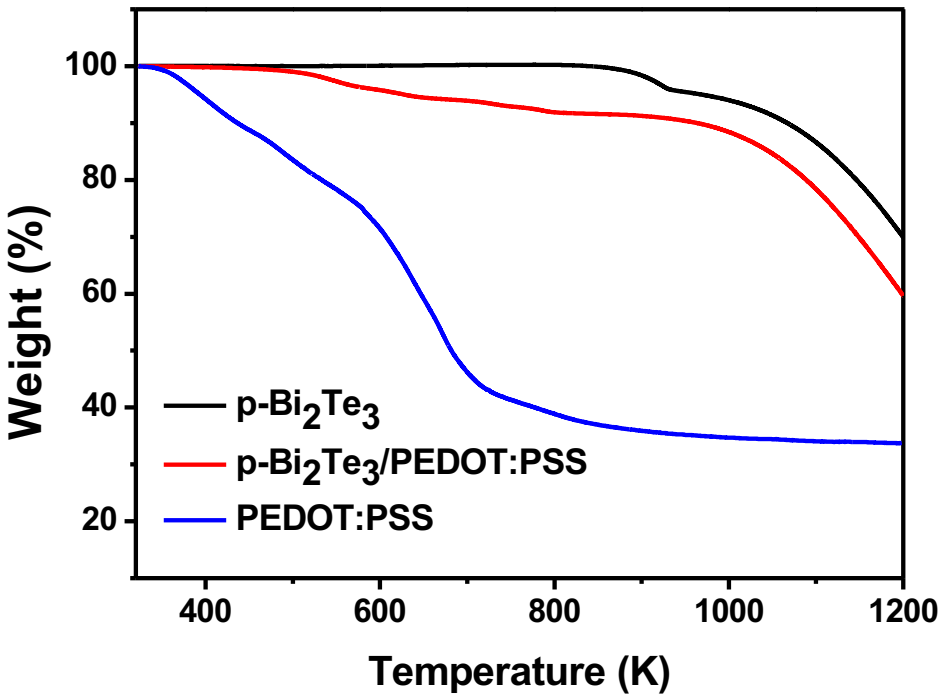

Figure 3.6 TGA of PEDOT:PSS, p-Bi_2Te_3, and p-Bi_2Te_3/PEDOT:PSS.

In order to study the annealing effects of TE properties of p-Bi_2Te_3/PEDOT:PSS composite, and to identify the optimal annealing condition, the samples were undergone annealing treatment at temperature at 423 K, 593 K, 623 K and 673 K.

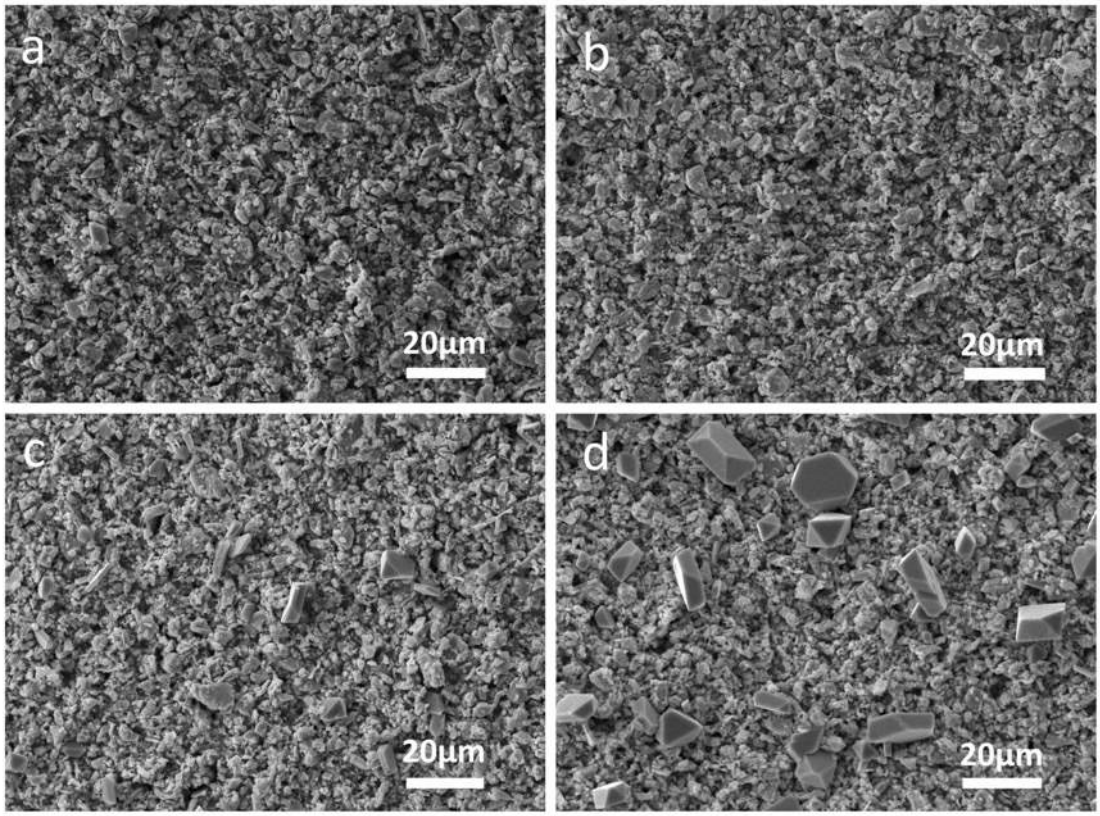

Figure 3.7 SEM images of p-Bi_2Te_3/PEDOT:PSS composite samples annealed at (a) 423 K; (b) 593 K; (c) 623 K; (d) 673 K.

Figure 3.7 shows surface SEM images of Bi_2Te_3/PEDOT:PSS samples annealed at various temperature, namely, 423 K, 593 K, 623 K and 673 K, respectively. It seems that the film samples annealed at 423 K and 593 K have higher density than the 623 K and 673 K annealed samples. Interestingly, compared with 423 K and 593 K samples, larger ordered crystals are observed in the samples annealed at 623 K and 673 K. With the increasing annealing temperature, the grains will grow up. Combined with the following cross-section SEM images of different annealing p-Bi_2Te_3/PEDOT:PSS composite samples, the schistose particles generate in 593K annealing sample initially, and then grow up with the raising temperature (**Figure 3.8**). In the 623 K and 673 K samples, the schistose particles

becomes more and some of the polyhedral particles reach about 20 μm. These ordered structures will affect the physical properties of samples accordingly.

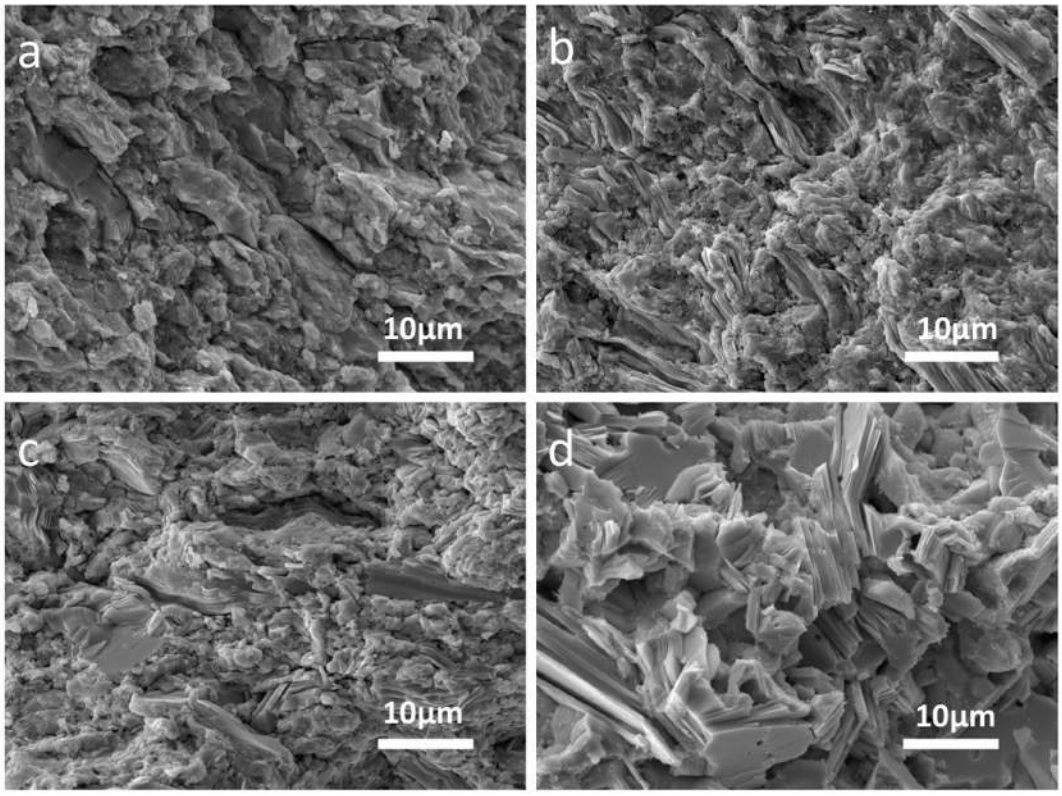

Figure 3.8 Cross-section SEM images of p-Bi_2Te_3/PEDOT:PSS composite samples annealed at (a) 423 K; (b) 593 K; (c) 623 K; (d) 673 K.

These structures are likely to affect the conductivities of the samples. For the 623 K and 673 K annealed samples, the apertures in the samples will act as the blockers, leading to favorable low thermal conductivity while poor electrical conductivity of the TE composites when comparing the traditional bulk Bi_xTe_y-type materials. For the 423 K and 593 K annealed ones, poor thermal conductor PEDOT:PSS will weaken the composite thermal conductivity of the composites. The TE performance results of both p-Bi_2Te_3 and p-Bi_2Te_3/PEDOT:PSS will be explored in the following section.

Table 3.1

Composition of p-Bi_2Te_3 alloy samples annealed at 423 K, 593 K, 623 K, 673 K.

Samples	Constituent Ratio
p-type Bi_2Te_3	$Bi_{0.52}$ $Sb_{1.48}Te_3$
p-type Bi_2Te_3 - 423K	$Bi_{0.52}$ $Sb_{1.48}Te_3$
p-type Bi_2Te_3 - 593K	$Bi_{0.52}$ $Sb_{1.48}Te_{2.98}$
p-type Bi_2Te_3 - 623K	$Bi_{0.52}$ $Sb_{1.44}Te_{2.97}$
p-type Bi_2Te_3 - 673K	$Bi_{0.52}$ $Sb_{1.39}Te_{2.96}$

As discussed before, the temperature annealing treatment plays a significant impact on compositions of p-Bi_2Te_3/PEDOT:PSS composites. **Table 3.1** demonstrates element analysis of p-Bi_2Te_3/PEDOT:PSS composite samples annealed from 23 K to 673 K, respectively. With increasing the annealing temperature, the S will decrease due to the gradationally decomposition of PEDOT:PSS. Similarly, the Te reduces as the aggravating thermal treatment, the reason is that Te tends to vaporize more easily than Bi during high temperature annealing process. Thus, the annealing treatment plays an role in the structure and composition of the composites but also the TE properties which will be discussed in

the follow section.

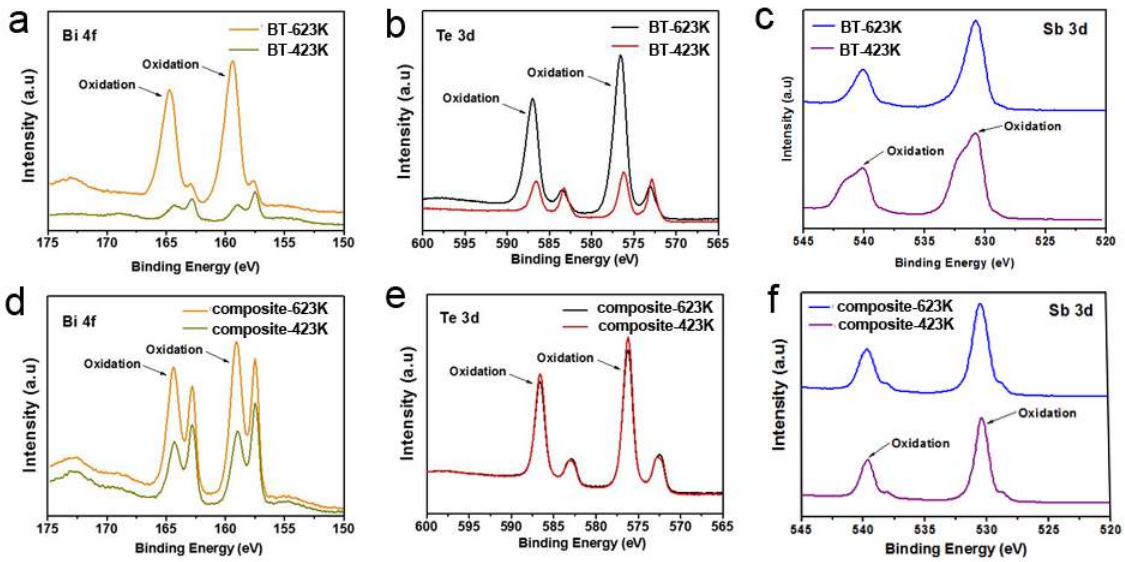

Figure 3.9 XPS spectra of pure (a-c) Bi_2Te_3 and (d-f) Bi_2Te_3/PEDOT:PSS samples annealed at 423K and 623K.

To further study the interaction between the p-Bi_2Te_3 and the PEDOT:PSS in the composite system, the 423 K and 623 K annealed p-Bi_2Te_3 and p-Bi_2Te_3/PEDOT:PSS samples are analyzed by XPS. Figure 3.8 reveals Te 3d and Bi 4f main peaks of pure Bi_2Te_3 in Bi_2Te_3/PEDOT:PSS samples annealed at 423 K and 623 K. A resolution scan of the Bi 4f range of pure Bi_2Te_3 samples (**Figure 3.9 (a,c)**) shows peaks at about 162.9, 162.8 and 157.6, 157.5 eV, which are attributed to the Bi 4f 5/2 and Bi 4f 7/2 of Bi_2Te_3, respectively.(*96*) For the Bi_2Te_3/PEDOT:PSS composites, Bi 4f 5/2 and Bi 4f 7/2 are described as 162.8 and 157.5 eV, respectively. Moreover, another four peaks in the Te 3d region display signals at 583.4, 583.3 and 572.9, 573.1 eV, which are fitted with the Te 3d 3/2 and Te 3d 5/2 of the Bi_2Te_3.(*96*) For the Bi_2Te_3/PEDOT:PSS composites, Te 3d 3/2

and Te 3d 5/2 are presented as 582.9, 583.1 and 572.7, 572.5 eV, respectively. Apart from this, in the pure Bi_2Te_3 and Bi_2Te_3/PEDOT:PSS spectra, it is evident that the Bi_2O_3 and TeO_2 are present on the surface as a result of oxidation of Bi and Te atoms. Interestingly, compared with the 423 K-annealed p-Bi_2Te_3 and p-Bi_2Te_3/PEDOT:PSS samples, the oxidation of Bi in p-Bi_2Te_3/PEDOT:PSS sample can be effectively alleviated owing to the PEDOT:PSS. Also, it can be seen in XPS spectra, where the content of Te of 623 K- annealed samples is slightly lower than that of 423 K- annealed one. This is because the sublimation energy of Bi and Te is 104.80 kJ/mol and 52.55 kJ/mol, respectively, demonstrating that Te tends to sublime easier than Bi when in the high temperature annealing process.(*97*)

3.3.4 Thermoelectric properties of p-Bi_2Te_3/PEDOT:PSS composites

After confirming the structure of p-Bi_2Te_3/PEDOT:PSS composites, and the pretreatment conditions, TE performance of p-Bi_2Te_3/PEDOT:PSS sample will be studied in this section. To fully understand the TE behavior of p-Bi_2Te_3/PEDOT:PSS composites, both TE performance of p-Bi_2Te_3 and p-Bi_2Te_3/PEDOT:PSS, annealing at various temperatures (423K, 593K, 623K, 673K), measuring from RT to 423K, are compared and evaluated.

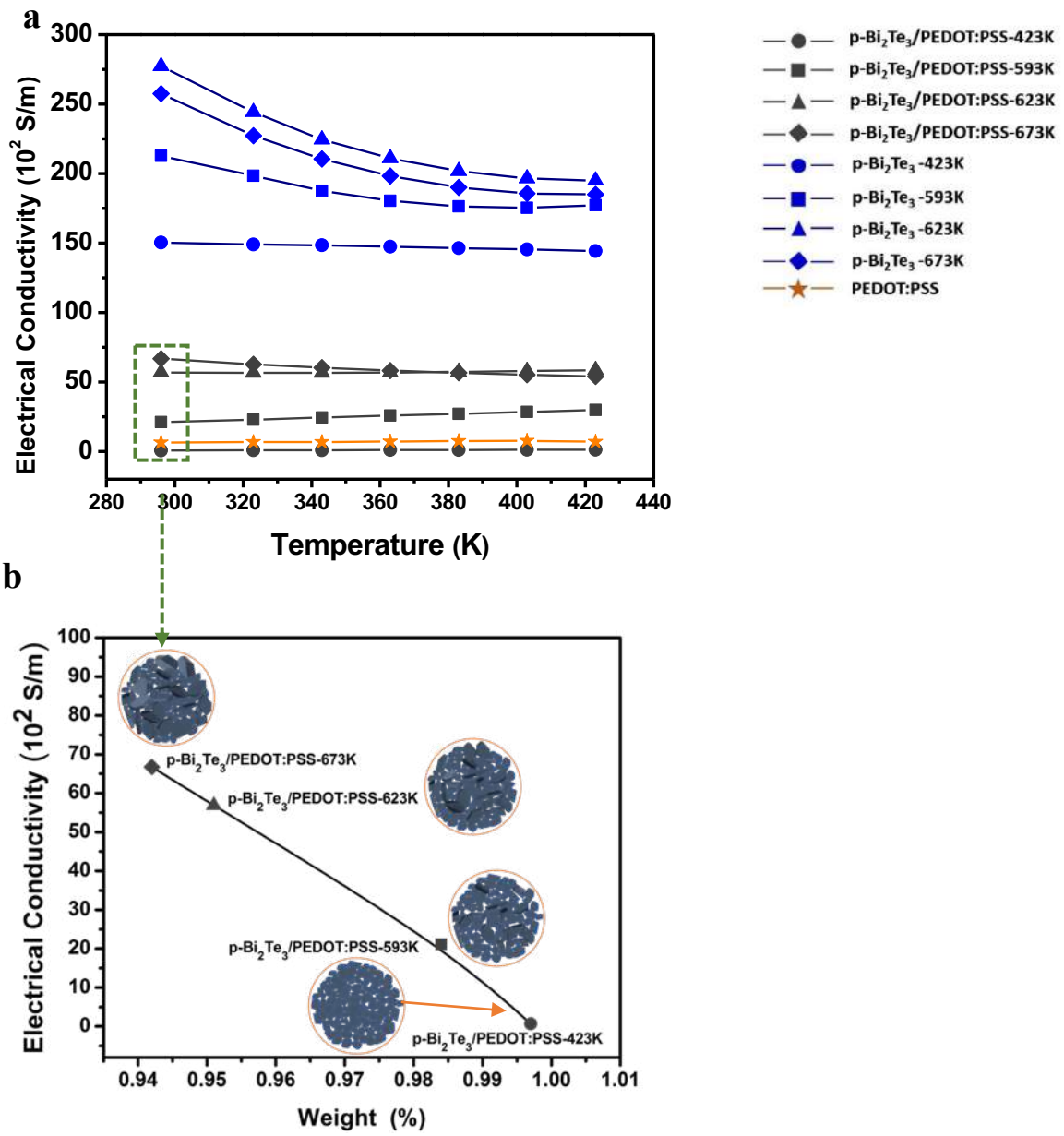

Figure 3.10 (a) Measured temperature-dependent electrical conductivity of p-Bi_2Te_3, p-Bi_2Te_3/PEDOT:PSS, and PEDOT:PSS, respectively. (b) Measured Room Temperature electrical conductivity of p-Bi_2Te_3/PEDOT:PSS with the weight variance under annealing, respectively.

The temperature-dependent electrical conductivity of p-Bi_2Te_3, p-Bi_2Te_3/PEDOT:PSS, and PEDOT:PSS are displayed in **Figure 3.10 (a)**, respectively. All the electrical conductivities of the samples are measured from RT to 423K. On one hand, regardless of the annealing

temperature, p-Bi_2Te_3 samples always have higher electrical conductivity than the composites. And the electrical conductivities of all these four pretreatment samples weaken with the increasing measuring temperature up to 423K, demonstrating degenerate semiconducting behaviour.(*98*) One the other hand, the electrical conductivity of the PEDOT:PSS keeps stable without large change from the room temperature to 423K, the average electrical conductivity is 6.96×10^2 S/m.

For the p-Bi_2Te_3/PEDOT:PSS composites, the electrical conductivities enhance with the increasing annealing temperature treatment. And the performance do not change a lot from RT to 423K. The electrical conductivity near room temperature of the composites is enhanced from 0.70×10^2 S/m to 66.8×10^2 S/m, with the annealing temperature from 423K to 673K. We can use the percolation-like theory to interpret this phenomenon.(*99, 100*) Considering the conductive path of the compound system, the conductivities of p-Bi_2Te_3/PEDOT:PSS composites are influenced by the intrinsic conductivity of the p-Bi_2Te_3 and PEDOT:PSS matrix, and also influenced by the polymer-filler interactions. Combined with the TGA data discussed above, the measured room temperature electrical conductivity of p-Bi_2Te_3/PEDOT:PSS is derived with the weight variance under annealing pre-treatment.

Figure 3.10 (b) illustrates the four stages of the formation of the p-Bi_2Te_3/PEDOT:PSS composites. The first stage involves the precursor consists of p-Bi_2Te_3 particles, PEDOT:PSS and few organic insulated binders (p-Bi_2Te_3/PEDOT:PSS-423K). The electrical conductivity of the 423K-annealed sample at room temperature is 0.697×10^2 S/m, showing the lowest among the composite samples even lower than pure PEDOT:PSS. This result is deemed reasonable due to the presence of the PEDOT:PSS which can fill up the pores in Bi_2Te_3 matrix, increasing the flexibility of the sample while receding electrical property. In a polymer matrix, the carriers can flow through the contact conducting particles,

forming a continuous path. (*101, 102*) When the annealing temperature up to 593K, the composite comes to the second stage. At this stage, the low-boiling-point binders evaporate when the samples are heated at or above 423K and the electrical conductivity of sample increases to 21.12× 10^2 S/m. Apart from the reduction of organic binders, the decomposition of insulated PSS also facilitated this performance. Then, the compact microstructure can be found in the third (p-Bi_2Te_3/PEDOT:PSS-623K) and four (p-Bi_2Te_3/PEDOT:PSS-673K) stage. The near room temperature electrical conductivity of 623K- and 673K- annealed samples are 56.81× 10^2 S/m, and 66.76× 10^2 S/m, respectively. The solid composite is formed with p-Bi_2Te_3 particles in an electrically conductive PEDOT:PSS matrix, when annealed under 673K. PEDOT:PSS may be partially degraded at temperature below 663K. The degradation and re-orientation of the PEDOT:PSS may affect the electrical conductivity, and the PEDOT acts as the bridges to couple the Bi_2Te_3 particles, forming the crisscross circulation network between the particles, which facilitates the charge transport. The small particles of p-Bi_2Te_3 grow up and occupied the interspace between the bulky particles, enhancing the system packing density, thus increasing the conductivity. When the annealing temperature increases at or above 673K, the electrically conductive PEDOT degrade a lot thus p-Bi_2Te_3 particles form their own connected network in the composite. The electrical performance enhanced with grain building and particle compaction. Overall, this hard data here explain the effectiveness of the enhancing annealing treatment for the p-Bi_2Te_3/PEDOT:PSS composites.

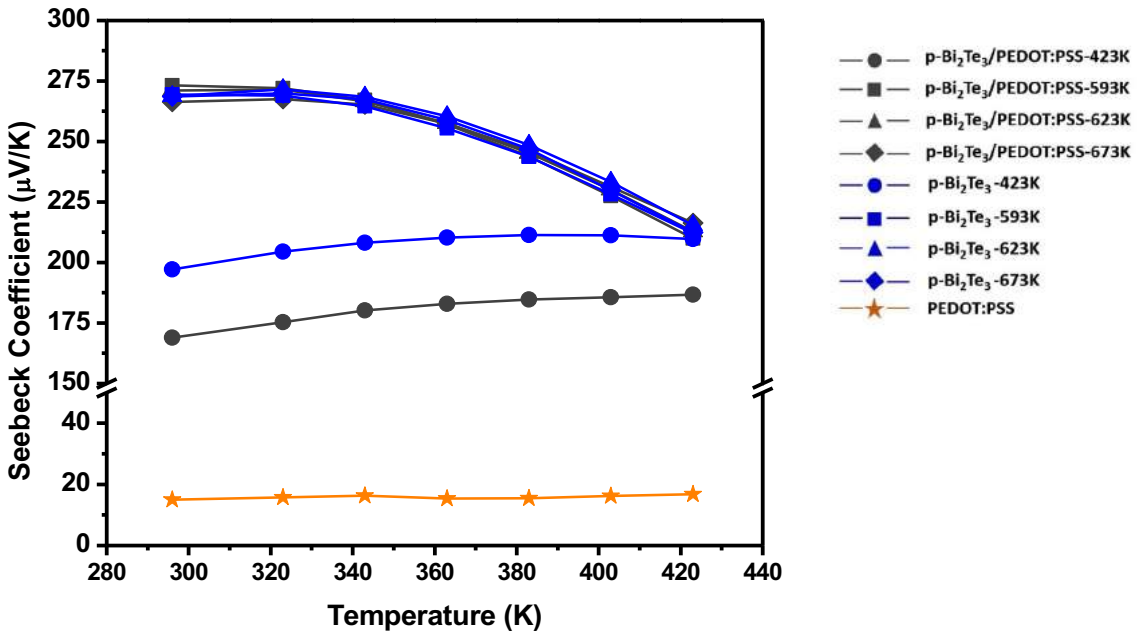

Figure 3.11 Measured temperature-dependent Seebeck Coefficient of p-Bi_2Te_3, p-Bi_2Te_3/PEDOT:PSS, and PEDOT:PSS, respectively.

The Seebeck coefficient results are displayed in **Figure 3.11**. For the PEDOT:PSS sample, the Seebeck coefficient of the PEDOT:PSS do not change much from the room temperature to 423K, the average Seebeck coefficient is 18.54 μVK^{-1}. However, after cooperating with the p-Bi_2Te_3, the Seebeck Coefficient of Bi_2Te_3/PEDOT:PSS composites significantly improve. The raising annealing temperature drastically enhances the Seebeck coefficient of the p-Bi_2Te_3/PEDOT:PSS composites from 168.9 $\mu VK^{-1}$to 273.3 μVK^{-1} at room temperature. Surprisingly, the Seebeck coefficient of the composites reaches the same level as that of the pure Bi_2Te_3 in the room temperature range,. If annealed above 593K, both the composites and Bi_2Te_3 show the same linear declination with the temperature from 296 K to 423 K, and the maximum value of 273.3 μVK^{-1} at 296 K. This is partly due to the partial removal of the poor TE performance of PEDOT:PSS in the composite, left more Bi_2Te_3. In addition, the formation of conducting channel between the inorganic and organic constituents is required because Seebeck coefficient is hinged on the conductivity of

individual paths. Thermal conductivity is also influenced by the morphology via scattering mechanism.(*21*)The maximum Seebeck coefficient of annealed Bi_2Te_3 is 270 μV/K, slightly lower than that of the composite. The corresponding changes brought to Bi_2Te_3 are similar but smaller. In general, both the p-Bi_2Te_3 and p-Bi_2Te_3/PEDOT:PSS samples exhibit considerably high Seebeck Coefficients when benchmarks performance with other contemporary works (See Table 3.1and Table 3.2). To further explore this interesting phenomenon, hall measurements are taken to further verify the relation between the composite morphological evolution and the electrical properties. As we all know, Seebeck coefficient reflects intrinsic electron transport.(*103*) In general, the Seebeck coefficient can be described with carrier (electrons or holes) concentration, n and effective mass, m*.(*103*)

$$s = \frac{8\pi^2 \kappa_B^2 T}{3eh^2} m^* \left(\frac{\pi}{3n}\right)^{2/3}$$

Where n is carrier concentration, S is Seebeck coefficient, κ_B represents Boltzmann constant, e means unit charge, h is Planck constant, m* is effective mass. Seebeck Coefficient is concerned with measuring temperature (T), which in the positive way, also related to the carrier concentration (n), which in the negative way. For the Bi_2Te_3/PEDOT:PSS composites, these relatively high-Seebeck coefficients could be benefited from the low carrier concentrations with the range from 2.54×10^{17} to 1.60×10^{18} cm^{-3} for the 593K, 623K, 673K- annealed samples. Because the positive Seebeck coefficient will lower carrier concentration somehow. As aggravating thermal treatment, the Seebeck coefficients of these equivalents enhanced gradually. However, the electrical conductivity (σ) is related to the carrier concentration (n) and carrier mobility (μ) as follows $\sigma = ne\mu$, where e is the electron charge.(*103*) From this point of view, increasing electrical conductivity and Seebeck coefficient simultaneously seems hard and challenge.

Here, the increase of both electrical conductivity and Seebeck coefficient indicate the effectiveness of annealing treatment.

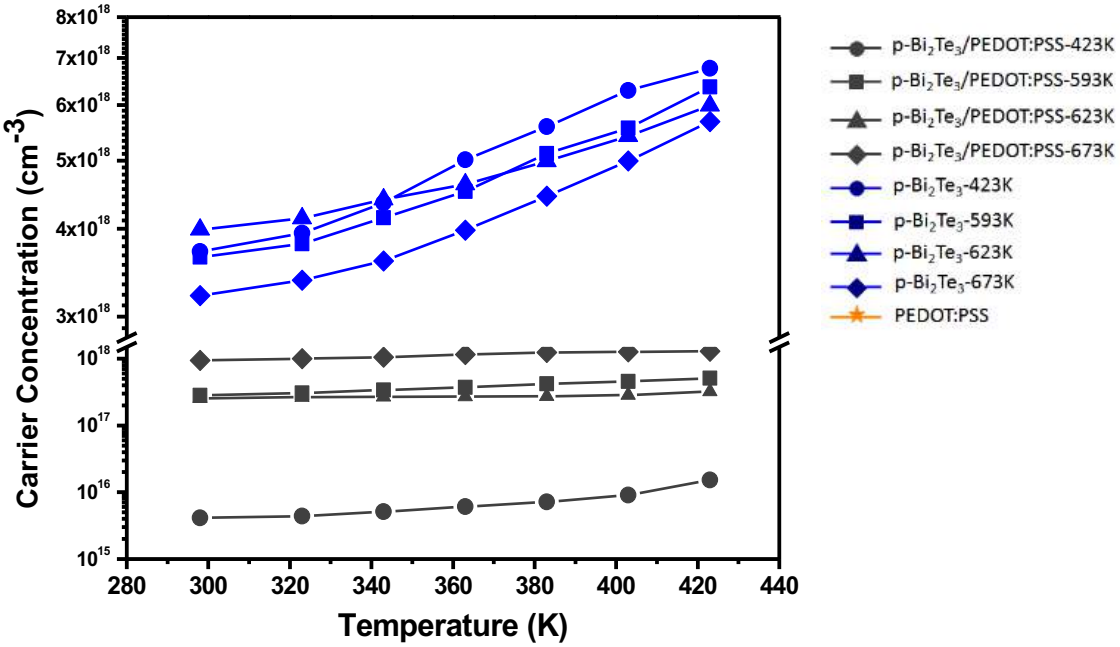

Figure 3.12 Measured properties of carrier concentration of p-Bi_2Te_3/PEDOT:PSS and p-Bi_2Te_3 as a function of temperature.

For the p-Bi_2Te_3 samples, the carrier concentrations of the p-Bi_2Te_3 samples are above 3×10^{18} cm^{-3}. These figures were relatively lower compared with 1×10^{19} cm^{-3}-3×10^{19} cm^{-3} of typical bulk Bi_2Te_3-based materials. However, although this is not good for the electrical conducting performance, this outcome is advantageous to the Seebeck coefficient. The lattice structure of Bi_2Te_3 consists of quintuple layers, which connected with Van der Waals force. Each quintuple layer compose Te(1)-Bi-Te(2)-Bi-Te(1). In Bi_2Te_3, the major charge carriers are hole, generated by Te_{Bi} antisite defects.(*104*) The evaporation energy of Bi and Te are 104.80 kJ/mol and 52.55 kJ/mol, respectively, demonstrating that Te tends to vaporize more easily than Bi during high temperature annealing process.(*105*) Compared with the carrier concentration of 623K and 673K annealed Bi_2Te_3 samples, the carrier

concentration of 623K annealed sample was higher than that of 673K annealed one, indicating that a small number of tellurium was vaporized during the high temperature annealing process.

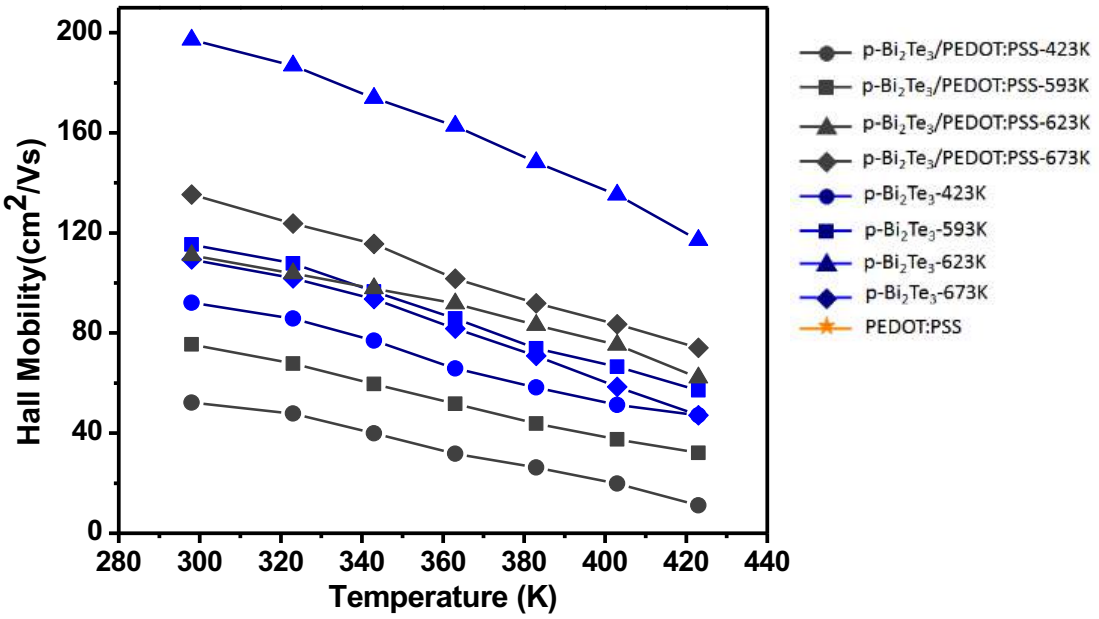

Figure 3.13 Measured properties of hall mobility of p-Bi_2Te_3/PEDOT:PSS and p-Bi_2Te_3 as a function of temperature.

Apart from carrier concentration, we also use hall mobility to decipher the electrical properties of the samples. **Figure 3.13** presents the changes of mobility (μ_H) of annealed TE samples as a function of temperature. The results show that the hall mobility was weakened with increasing temperature while the carrier concentration show the opposite tendency. For the TE samples, the carrier mobility dominates electrical conductivity with the temperature range. As illustrated in **Figure 3.13**, cooperating with p-Bi_2Te_3 can improve the low mobility of PEDOT:PSS (reported works: 2.5 $cm^2/V{\cdot}s$, 1.7 $cm^2/V{\cdot}s$), (*106, 107*) but for the 623K annealed samples, the corresponding μ_H value decreases in composites with PEDOT:PSS. The possible reason is that more phonons in the p-Bi_2Te_3/PEDOT:PSS composite than that of pure Bi_2Te_3, and thus increases carrier

scattering, which tends to reduce mobility. The carrier mobility of the Bi_2Te_3 is increased from 26.7 $cm^2/V \cdot s$ up to 146.28 $cm^2/V \cdot s$ at room temperature by the annealing treatment. High temperature annealing caused a reduction in grain boundary and scattering center, which provide a long effective mean free path of carriers, attributing to the mobility enhancement.(*16*)

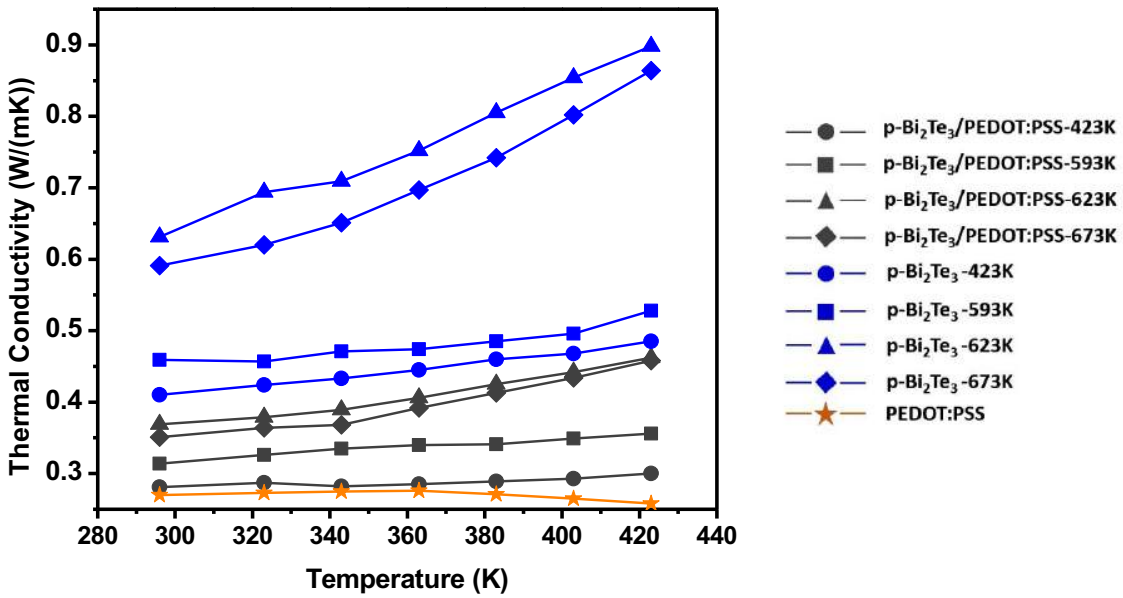

Figure 3.14 Measured temperature-dependent thermal conductivity of p-Bi_2Te_3, p-Bi_2Te_3/PEDOT:PSS, and PEDOT:PSS, respectively.

Figure 3.14 shows the thermoelectric properties of p-Bi_2Te_3/PEDOT:PSS composite films and p-Bi_2Te_3 particle samples annealed at 423K, 593K, 623K, 673K for 3 h, respectively. The annealing treatments have increased the thermal conductivity of all samples, as illustrated in **Figure 3.14**. The higher the annealing temperature, the greater the thermal conductivity. The composites have lower thermal conductivity in all the cases than p-Bi_2Te_3 samples. In this composite system, the lowest thermal conductivity was 0.28 $Wm^{-1}K^{-1}$ (annealed at 423K), owing to the thermally insulating PEDOT:PSS polymer of ~0.27 $Wm^{-1}K^{-1}$, formation of pores and interface between the particle and matrix. The highest

thermal conductivity of composite is 0.462 $Wm^{-1}K^{-1}$, annealed at 673K, which is still lower than all the pure Bi_2Te_3 particles. The reason of the low thermal conductivity of 423K, 593K annealed composite samples is because of the thermal insulated PEDOT:PSS. This is different from the 623K and 673K annealed samples, the porous act as the thermal blockers instead. On the other hand, the limited phonon mean free path in this composite system can effectively reduce its thermal conductivity. The thermal conductivity, κ, of a material can be divided into two heat carriers, phonons of the lattice, κ_l, and electrons, κ_{elec}. The phonon thermal conductivity, κ_l, is expressed by the Boltz-mann equation,(*21*) $\kappa_l = \frac{1}{3}\sum_{\lambda\kappa} C_{\lambda\kappa}\, v_{\lambda\kappa}\Lambda_{\lambda\kappa}$, where $C_{\lambda\kappa}$, is specific heat, $v_{\lambda\kappa}$is group velocity, $\Lambda_{\lambda\kappa}$ is mean free path, respectively.(*108*) The limited phonon mean free path in this composite system can effectively reduce its thermal conductivity. Thermal conductivity is also influenced by the morphology via scattering mechanism. By adding scattering centers, or by heat-induced degradation of PEDOT:PSS, or by inducing micro-rough surface due to annealing, the thermal conductivity will be further reduced.(*108*)

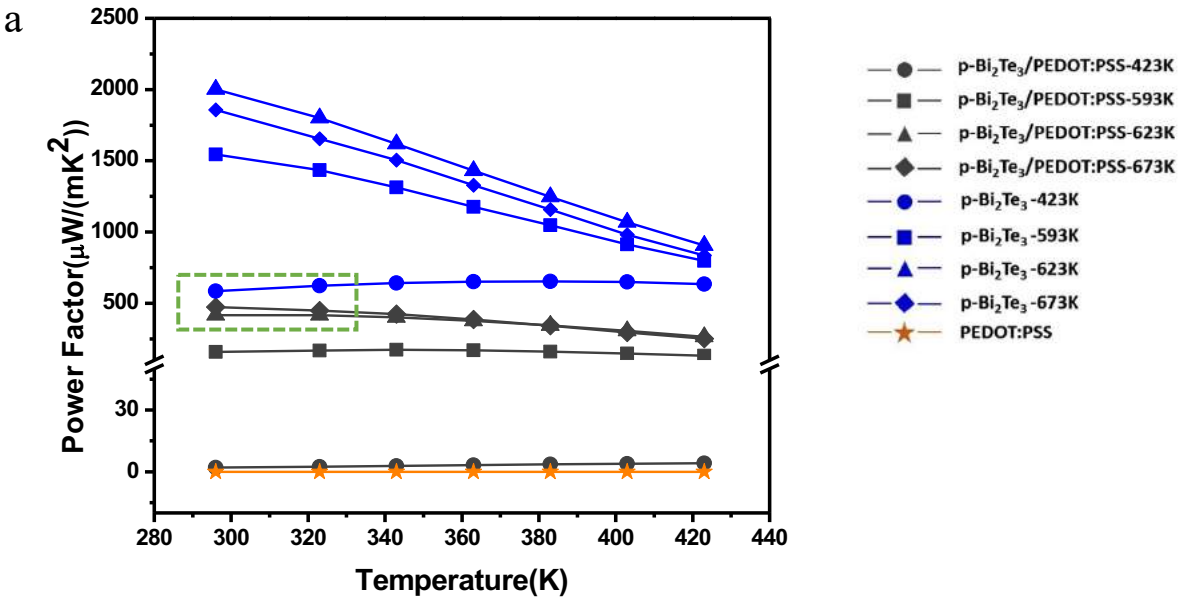

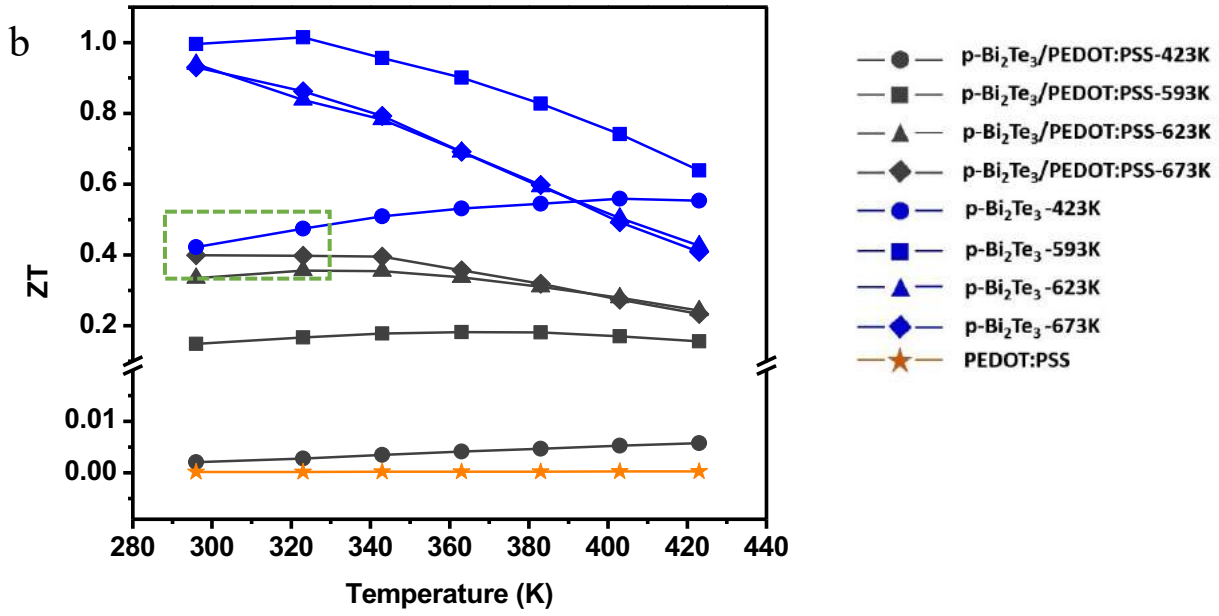

Figure 3.15 Measured properties of (a) Power factor and (b) Figure of merit of Bi_2Te_3, Bi_2Te_3/PEDOT:PSS, respectively.

The power factor and figure of merit (ZT) are plotted in **Figures 3.15 (a)** and **(b)**, respectively. The power factor of PEDOT:PSS is about 0.175 μW/(m·K^2), and the corresponding value of p-Bi_2Te_3 in this work is about 2000 μW/(m·K^2) at room temperature. The maximum power factor of the p-Bi_2Te_3/PEDOT:PSS composite is 473.5 μW/(m·K^2), obtained from the sample annealed at 673K. The ZT value of the composite at room temperature increases from 0.002 to almost 0.4. These promising ZT values of the composite samples originate in high electrical conductivities and ultra-low thermal conductivities. Under 673K annealed temperature, the PEDOT:PSS would decompose and the electrical of this sample was a little bit higher than that of the rest composite ones. However, due to the lower thermal conductivity of the composite, the performance of samples annealed 623K is comparable to that of 673K. Interestingly, for the Bi_2Te_3 subgroup, ZT of the samples annealed at 623K and 673K decreases from 0.94 and 0.93 at 296 K to 0.43 and 0.41 at 423 K, respectively. Though the power factor of 423K annealed

Bi_2Te_3 is the lowest, its ZT value increases with annealing temperature while the others decrease within the same temperature range. This is partially attributed to the relatively low thermal conductivity brought by low-temperature annealing. Generally, the power factor and ZT of the composites are always lower than those of the pure p-Bi_2Te_3, respectively. It is reasonable as a homogeneous composite composed of disparate ingredients working separately cannot have a higher power factor or ZT than that of any single component. However, the highest power factor and ZT of the composite samples are comparable to the bulk p-Bi_2Te_3 samples near room temperature (refer to the green gridlines) while the composites fully demonstrate highly flexibility. In terms of the power factor, the fairly high Seebeck coefficient of the composites benefit to power performance. On the part of ZT value, the low thermal conductivity resulted in high peak ZT values for p-Bi_2Te_3/PEDOT:PSS material. Our results deconvolve that inorganic-organic strategy is eminently suitable for high-performance flexible TE generators compared with the established protocols.

3.3.5 Comparison with previously reported work

Table 3.2 Thermoelectric performance of the p-Bi_2Te_3 composites compared with other related works at the room temperature.

Table 3.2 Thermoelectric performance of the p-Bi_2Te_3 composites compared with other related works at the room temperature.

Sample	**Carrier Type**	**S (μV K^{-1})**	**σ(10^2 S m^{-1})**	**κ (W m^{-1}K^{-}**	**PF (μ W m^{-1} K^{-2})**	**ZT**	Ref.
Bi_2Te_3-	p	197.13	150.4	0.41	584.4	0.42	
Bi_2Te_3-	p	269.42	212.8	0.459	1544.6	0.10	
Bi_2Te_3-	p	268.69	277.3	0.631	2002.2	0.94	
Bi_2Te_3-	p	268.58	257.4	0.591	1857.0	0.93	
Bi_2Te_3	p	218.2	829	1.40		~0.82	(*109*)
Bi_2Te_3	p	213.1	723	~0.90		~1.10	
Bi_2Te_3	p	214.2	659	~0.90		~0.95	
Bi_2Te_3	p	231.1	581	~0.90		~1.20	
Bi_2Te_3	p	226.0	586	~0.90		~0.98	
Bi_2Te_3	p	218.0	500	~1.20	4.5	~0.60	(*110*)
Bi_2Te_3	p	255.0	450	~0.92		~1.00	
Bi_2Te_3	p	140.0	1667	1.30		0.80	(*111*)
Bi_2Te_3	p	217.0	~940	~1.35		~0.98	(*112*)
Bi_2Te_3	p	~235.0	~620	~1.05		~0.98	
Bi_2Te_3	p	~232.0	~700	~0.92		~1.22	
Bi_2Te_3	p	~235.0	~720	~0.70		~1.70	

Table 3.2 Thermoelectric performance of the p-Bi_2Te_3 compound compared with other related works at the room temperature.

Sample Composition	**Carrier Type**	**S (μV K^{-1})**	**σ(10^2 S m^{-1})**	**κ (W $m^{-1}K^{-}$**	**PF (μ W m^{-1} K^{-2})**	**ZT**	Ref.
Bi_2Te_3	p	122.3	~2400	~2.15		0.51	(*113*)
Bi_2Te_3	p	138.4	~1900	~1.75		0.63	
Bi_2Te_3	p	150.6	~1700	~1.60		0.72	
Bi_2Te_3	p	166.9	~1400	~1.35		0.87	
Bi_2Te_3	p	177.5	~1200	~1.25		0.93	
Bi_2Te_3	p	200.0	~900	~1.20		0.96	
Bi_2Te_3	p	213.2	~800	~1.00		0.99	
Bi_2Te_3	p	237.0	~500	~1.00		0.78	
Bi_2Te_3	p	243.2	~300	~1.00		0.45	
Bi_2Te_3	p	~250	~40	~0.85		0.95	(*114*)
Bi_2Te_3	p	~250	~40	~0.82		0.95	
Bi_2Te_3	p	~250	~40	~0.78		1.02	
Bi_2Te_3	p	~250	~40	~0.80		1.01	
Bi_2Te_3	p	~260	~40	~0.83		1.08	
Bi_2Te_3	p	~170	~67	~1.00		0.55	
Bi_2Te_3	p	~225	~50	~0.92		0.82	

Table 3.3 Thermoelectric performance of the p-Bi_2Te_3/PEDOT:PSS composites compared with other related works at the room temperature.

Table 3.3 Thermoelectric performance of the p-Bi_2Te_3/PEDOT:PSS composites compared with other related works at the room

Sample Composition	Carrier Type	S (μV K^{-1})	σ(10^2 S m^-	κ (W $m^{-1}K^-$	PF (μ W m^{-1} K-	ZT	Ref.
Bi_2Te_3/PEDOT:PSS-423K	p	168.967	0.697	0.281	1.99	0.0021	
Bi_2Te_3/PEDOT:PSS-593K	p	273.26	21.14	0.314	157.85	0.15	
Bi_2Te_3/PEDOT:PSS-623K	p	271.03	56.81	0.369	417.31	0.335	
Bi_2Te_3/PEDOT:PSS-673K	p	266.307	66.76	0.351	473.47	0.4	
PEDOT:PSS/Bi_2Te_3	p	14.2-18.6	421	0.07□0.02	9.9	0.04	
Bi_2Te_3/PEDOT:PSS/Bi_2Te_3	p	15.3	403.5	0.169-		0.0172	(*115*)
10% Clevios PH1000/Bi_2Te_3	p	~150	~55	~0.558	131	0.08	
17% Clevios PH1000/Bi_2Te_3	p	~110	~75	0.553	113	0.06	
23% Clevios PH1000/Bi_2Te_3	p	~105	~100	0.543	119	0.07	
20% Clevios P/Bi_2Te_3	P	~140	~15	/	~27	/	(*58*)
38% Clevios P/Bi_2Te_3	p	~115	~20	/	~22	/	
48% Clevios P/Bi_2Te_3	P	~75	~35	/	~17	/	
30% Clevios FE-T/Bi_2Te_3	p	~110	~65	/	70	/	
45% Clevios FE-T/Bi_2Te_3	P	~95	~70	/	50	/	
55% Clevios FE-T/Bi_2Te_3	p	~70	~80	/	30	/	

Table 3.3 Thermoelectric performance of the p-Bi_2Te_3/PEDOT:PSS composites compared with other related works at the room temperature.

Sample Composition	Carrier Type	S ($\mu V K^{-1}$)	$\sigma(10^2$ S m^-	κ (W $m^{-1}K^-$	PF (μ W m^{-1} K-	ZT	Ref.
L-ab	**p**	14.9	222	/	5.0	0.11105	(*116*)
h-ab	p	16.3	401	/	10.6	0.0011	
p-ab	p	54	12.4	/	3.6	0.003	
2wt%Bi_2Te_3/PEDOT:PSS-drop cast film	p	~13	~1000	/	~17	/	(*117*)
2wt%Bi2Te_3/PEDOT:PSS-spin coated film	p	~20	~300	/	~10	/	
4wt%Bi_2Te_3/PEDOT:PSS-drop coated film	p	~16	~1300	/	~32	/	
4wt%Bi_2Te_3/PEDOT:PSS-spin coated film	p	~20	~250	/	~8	/	
8wt%Bi_2Te_3/PEDOT:PSS-drop coated film	p	~16	~1200	/	~30	/	
8wt%Bi_2Te_3/PEDOT:PSS-spin coated film	p	~30	~250	/	~25	/	
10wt%Bi_2Te_3/PEDOT:PSS-drop coated film	P	~16	~1200	/	~30	/	
10wt%Bi_2Te_3/PEDOT:PSS-spin coated film	p	~48	~100	/	~25	/	
Irradiated n- Bi_2Te_3/PEDOT:PSS	P	48.24□ 3	1390□ □ □	0.31□ □ □ □		0.28±0.04	(*118*)
Bi_2Te_3/PEDOT:PSS	p	25	300	/	20	/	(*119*)
20% p-Bi_2Te_3/PEDOT:PSS	P	15	~600	/	18	/	(*60*)
0.8% p-Bi_2Te_3/PEDOT:PSS-Glycerol	p	11.9	17.9	/	0.26	/	(*120*)

The Seebeck coefficient and ZT of both pure p-Bi_2Te_3 and p-Bi_2Te_3/PEDOT:PSS composites are compared with the previously reported work, as shown in **Table 3.2 and 3.3**, respectively. The highest Seebeck coefficients from the current work have been demonstrated for both pure Bi_2Te_3 and Bi_2Te_3/PEDOT:PSS composites. The pure p-Bi_2Te_3 annealed at 593 K exhibits the highest Seebeck coefficient of ~270 μV/K, among those reported values, that is, p-type Bi_2Te_3 alloys by spark plasma sintering (216 μV/K),(*121*) and improved bulk Bi_2Te_3 alloys (~218 μV/K, ~235 μV/K, ~230 μV/K, ~235 μV/K) by engineering through grain boundary and point-defect scattering,(*109*) Bi_2Te_3 prepared by ultra-fast thermally induced reaction (average 183.2 μV/K),(*113*) and others.(*111, 112, 114, 122*) Moreover, the as-fabricated p-Bi_2Te_3/PEDOT:PSS composite has achieved the highest Seebeck coefficient of 273.3 μV/K among all other Bi_xTe_y/PEDOT:PSS composite materials reported so far, demonstrating approximately 5.8 times higher than the reported Bi_2Te_3 alloy nanosheet/PEDOT:PSS composite fabricated by spin coating and drop casting techniques (47.5 μV/K),(*117*) 9.6 multiples higher than that of PEDOT:PSS/p-Bi_2Te_3-nanowires (14.9 μV/K, 16.3 μV/K, 54 μV/K) prepared by drop-cast method,(*116*) 1.8 times of Bi_2Te_3/PEDOT:PSS powder composites(~150 μV/K)(*58*) and et al.(*115, 123*)

3.4 Conclusion

In this Chapter, flexible solution processible p-Bi_2Te_3 /PEDOT:PSS TE materials are studied. p-type Bi_2Te_3/ PEDOT:PSS TE composites were fabricated and annealed at different temperature (423 K, 593 K, 623 K, 673 K). The measured thermal conductivity of the resultant composites is within the range from 0.28 to 0.46 W/(m·K), and their Seebeck coefficient from 168.9 to 273.3 μV/K with power factors from 4.12 to 473.5 μW/(m·K^2) near room temperature, respectively. The composites reach the same high

Seebeck coefficient value as that of the pure Bi_2Te_3, reduce their thermal conductivity and electrical conductivity. The first two effects bring out positive benefits to TEG performance, however, the reduced electrical conductivity is not desirable. In this work, the achieved highest figures of Seebeck coefficient and power factor are 273.3 μV/K and 473.5 $\mu W/(m \cdot K^2)$, respectively. They outweigh by a large margin over other previously reported works on TE composites. The outstanding TE performance of the solution-processible p-type Bi_2Te_3/ PEDOT:PSS composites have demonstrated the great application potentials and advantages not available to conventional rigid inorganic thermoelectric devices.

Chapter 4 THERMOELECTRIC PERFORMANCE OF N- BISMUTH TELLURIDE/PEDOT:PSS COMPOSITES

4.1 Introduction

As aforementioned in Chapter 3, the flexible p-Bi_2Te_3/PEDOT:PSS material is introduced, emerging as a novel promising class of flexible p-type TE materials. In FETGs, mutual collaboration of p- and n-types is needed, therefore, the organic/inorganic tactic will be used to obtain the high-powered counterpart as well. While p-type flexible TE materials have witnessed rapid advancement, the developing progress of n-type ones still lags behind owing to the difficulties in n-type doping of organic conducting polymers. N-type doping is a valid method to regulate the interface and carrier concentration, realizing the enhanced performance of typical semiconductors. Nevertheless, n-type dopant as reductive agent, it is hard to reconcile the doping ability and the needs of stability. After doping, n-type dopant become positive ion, which shows poor miscibility in the conducting polymers. Hence, finding an effective, homogeneous and stable tactic is always the research hotspot in the TE field. As we all know, most n-type organic semiconductors are not unstable in air, which significantly hinders the utilization of conducting polymers in TEGs. Reduced polymer chain and counter-cations which can oxidized by O_2 make the n-type conducting polymer unstable in air. In addition to the poor air-stability , the classical n-doped polymers usually low electricity. Remarkable trials are devoted to solve this essential problem.

PEDOT:PSS is also a very promising candidate for n-type thermoelectrics due to advantages including it being environmentally stability, and mechanical flexibility. Katz et

al. incorporated both p- and n-type Bi_2Te_3 ball-milled powders with PEDOT:PSS(commercialized PEDOT:PSS products CLEVIOS PH1000 and FE-T), respectively, achieving enhanced power factor of around 47 $\mu Wm^{-1} K^{-2}$ and 30 $\mu Wm^{-1} K^{-2}$ for both composites.(*58*) Cho and co-workers reported screen-printed PEDOT:PSS-coated Bi_2Te_3 (n-type) film, with improved flexibility and thermoelectric performance. The slightly enhanced Seebeck coefficient attained -137mV/K and the figure of merit ZT reached up to 0.16.(*59*)

Despite these achievements, low carrier concentration and electrical conductivity are still the bottleneck problems for most polymers. The adjustment should be judiciously optimized to obtain high-performance thermoelectric device. It is of interest to determine whether the same strategy can improve n-type conductivity as well. In spired by the work in Chapter 3, we also use the PEDOT:PSS as the conducting polymer, cooperating with n-Bi_2Te_3 particles, forming the homogenous flexible n-type TE material. Integration of solution-printability, air stability, and flexibility makes the as-assembled n-Bi_2Te_3/PEDOT:PSS hybrids a new class of flexible high-performance thermoelectric materials for wearable self-powering.

4.2 Experimental

4.2.1 Materials

n-type Bi_2Te_3 (99.99%, KYD Materials), poly(3,4-ethylenedioxythiophene) polystyrene sulfonate (PEDOT:PSS, 5.0 wt. %, Sigma Aldrich), dimethyl sulfoxide (DMSO, 99.9% %, VWR Chemicals), ethanol (EtOH, 99.8%, VWR Chemicals), α-terpineol (96%, Alfa

Aesar), isopropanol (AR, UNI-CHEM), neutral silicone (100%, Ele-wintex), tetrahydrofuran (99.9%, VWR Chemicals).

4.2.2 Preparation of n-Bi_2Te_3/PEDOT:PSS hybrid ink paste

The TE ink was prepared based on a well-dispersed mixture of n-Bi_2Te_3 and PEDOT:PSS, with addition of DMSO, isopropanol and a-terpineol. During the mixing process n-Bi_2Te_3 particles and PEDOT:PSS were immersed into organic solvent, forming a homogeneous paste. The ink paste consists of 3.07 g n-type Bi_2Te_3, 0.4 g DMSO, 2.0 g PEDOT:PSS, 0.43 g isopropanol and 0.46 g α-terpineol. The pastes were mixed for 12 h using a magnetic stirrer. The solvent maintained the viscosity of ink paste at a desired level and used to the printing. The viscosity of the paste was measured by DV-E Viscometer, Brookfield.

4.2.3 Sample preparation for characterization and tests of TE properties

All the Bi_2Te_3, Bi_2Te_3/PEDOT:PSS samples were prepared as the pellets. Then the pellet samples were annlead at 423 K, 593 K, 623 K, 673 K using the tube furnace under argon atmosphere for 3 h before the measurements.

4.2.4 Structural characterization

The morphology of TE materials was characterized by scanning electron microscopy (Tescan VEGA3). The crystalline structure of TE materials was obtained from Rigaku Smart Lab with Cu Kα radiation (λ = 1.5406 Å). Thermal stability analysis of TE materials

was conducted on thermogravimetric analyzer (METTLER TOLEDO Thermal Analysis, STARe system) in an atmosphere of nitrogen.

4.2.5 Evaluation of TE performance

Seebeck coefficient and electrical conductivity of the TE films were obtained by SBA 458 Nemesis® measurement Setup (NETZSCH Group, Ge rman). The thermal conductivity was measured by laser flash apparatus (LFA 457 MicroFlash®, NETZSCH Group, German). Hall effect of TE samples were tested by pressure-assisted molybdenum contacts with 1T magnet, empolying the Van der Pauw technique.(*90*) (Lakeshore 8400)

4.4 Results and Discussion

4.4.1 Formation of n-Bi_2Te_3/PEDOT:PSS composites

In this work, as mentioned in the introduction, we also want to develop the flexible n-type TE ink to ensure the printability of the film structure. The major challenge for this strategy is to adjust the rheological property of the ink to guarantee the uniformity of extrusion structure without pinhead clogging. Also, the high stability of the materials avoids problems of nozzle clogging which might arise from particle sedimentation. In light of this consideration, PEDOT:PSS is also employed as the matrix to form the n-Bi_2Te_3 ($Bi_2Te_{2.68}Se_{0.32}$)/PEDOT:PSS. The used n-type Bi_2Te_3 particles are also of uneven size. The average size is roughly 5 μm. (**Figure 4.1**). The TE ink is prepared based on a well-dispersed mixture of n-Bi_2Te_3 and PEDOT:PSS, with addition of DMSO, isopropanol and α-terpineol.(**Figure 4.2**) During the mixing process, n-Bi_2Te_3 particles and PEDOT:PSS

were immersed into organic solvent, forming a homogeneous paste. The small granular n-Bi_2Te_3 were filled into the interspace of n-Bi_2Te_3 large particles, generating compact constituents. This constituent components served different purposes: n-Bi_2Te_3 particles and PEDOT:PSS were engineered for TE function; DMSO was added to increase the conductivity of PEDOT:PSS; Isopropanol and α-terpineol were used to adjust the paste viscosity.

The n-Bi_2Te_3/PEDOT:PSS composite was formed from its precursor as a printing paste ink, followed by solidification and annealing at moderate temperature. The viscosity of this ink is 24000 mPa·s, which is lower than that of the p-Bi_2Te_3/PEDOT:PSS (32000 mPa·s). One possible reason is that an increased particle loading enhances the probability of agglomeration phenomena, resulting an increase of ink viscosity. Larger particles, which endow greater inertia on interaction, are momentarily retarded and then accelerated. It requires high energy for dissipation, results in the phenomenon of larger viscosity. In a case of a constant volume fraction, the particle with larger size will increase the surface charge, the adsorption layer around these particles will greatly increase the effective hydrodynamic diameter of the particles, leading to the higher viscosity.

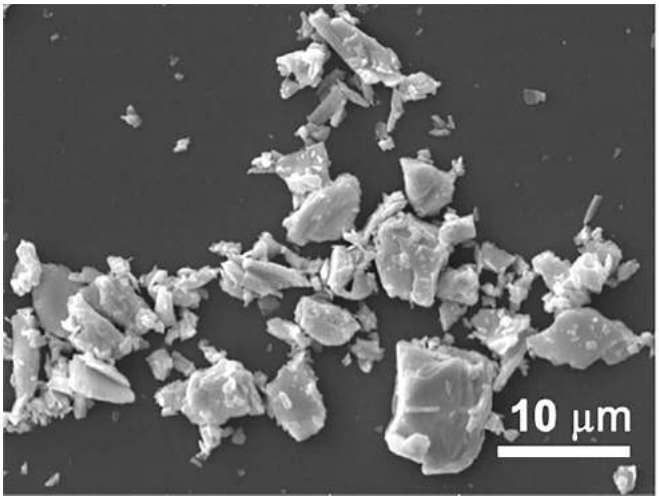

Figure 4.1 SEM Image of n-type Bi_2Te_3.

Figure 4.2 Photograph of p-type Bi_2Te_3/PEDOT:PSS ink.

4.4.2 n-Bi_2Te_3/PEDOT:PSS composites characterization

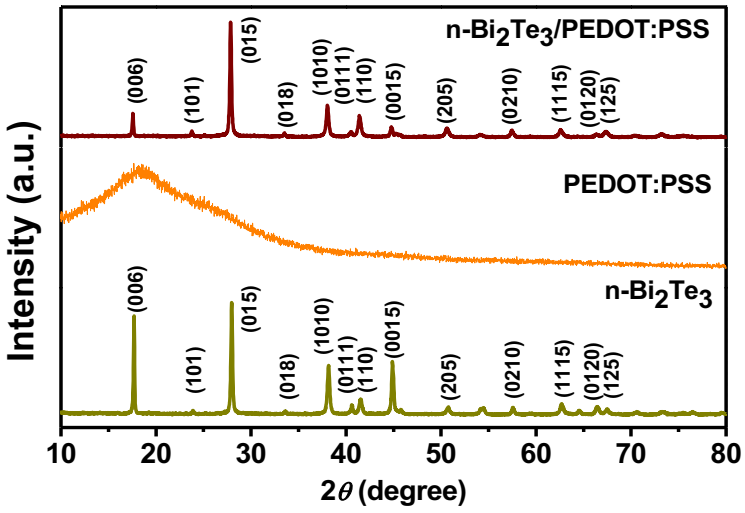

Figure 4.3 X- ray diffraction spectra of n-Bi_2Te_3, PEDOT:PSS, n-Bi_2Te_3/PEDOT:PSS, respectively

Figure 4.3 shows the XRD results of n-Bi_2Te_3, PEDOT:PSS, n-Bi_2Te_3/PEDOT:PSS, respectively. The peaks of n-Bi_2Te_3 in the XRD patterns are in accordance with a standard

card, Bi_2Te_3, PDF #08-0027. Also, the XRD patterns of n-Bi_2Te_3/PEDOT:PSS corresponds to the n-Bi_2Te_3 particles accompanied by spikes of amorphous matrix, which is due to the PEDOT:PSS.

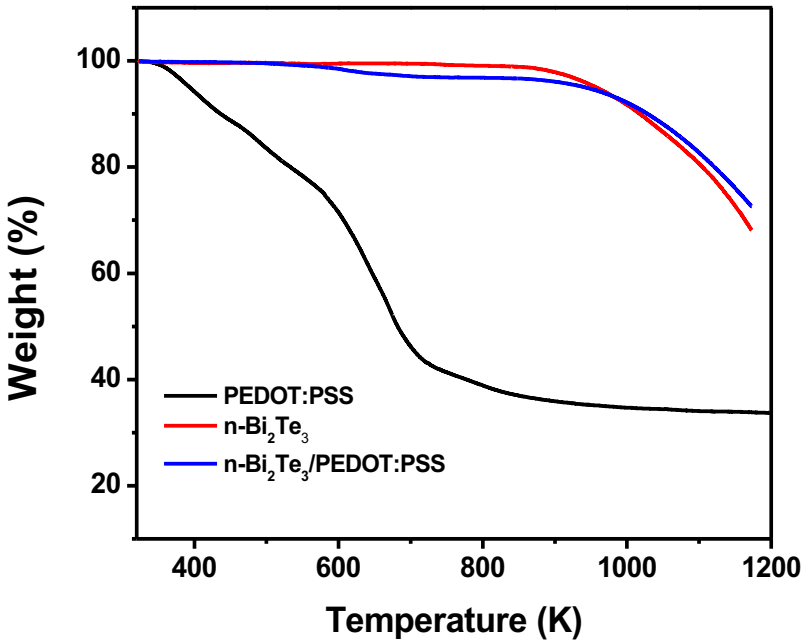

Figure 4.4 Thermogravimetric analysis (TGA) of n-Bi_2Te_3, PEDOT:PSS, n-Bi_2Te_3/PEDOT:PSS, respectively.

Figure 4.4 shows the weight variation of these three samples, pure n- Bi_2Te_3, PEDOT/PSS and n-Bi_2Te_3/ PEDOT/PSS specimens upon heating. For the PEDOT:PSS curved line, in the initial stage up to 473 K owing to the losing of water, then following the disintegration of organic residual.(*94*) The de-composition of PSS starts from 538 K ends at 593 K with a weight loss of 25 wt%. The sulfonate groups split at this intermediate temperature range. The last decomposition begins with 623 K and goes t 873K with the weight loss of 10 wt%, is ascribed to rupture of main polymer chain, PEDOT.(*94*) It is worth noting that the residual is about 58%. For the n-Bi_2Te_3/ PEDOT/PSS sample, the composite shows little weight loss below 523 K because of the organic binder residual. Above 533 K, a slightly

weight loss starting with 450K, and this loss continues to increase with the temperature goes to 800K. The sulfonate groups and PEDOT split at this intermediate temperature range.Then the sample comes in the platform till 900K. After 973K, the sample of Bi_2Te_3 melt down. For pure Bi_2Te_3, the appropriate annealing treatment should be below 900K.(*95*)

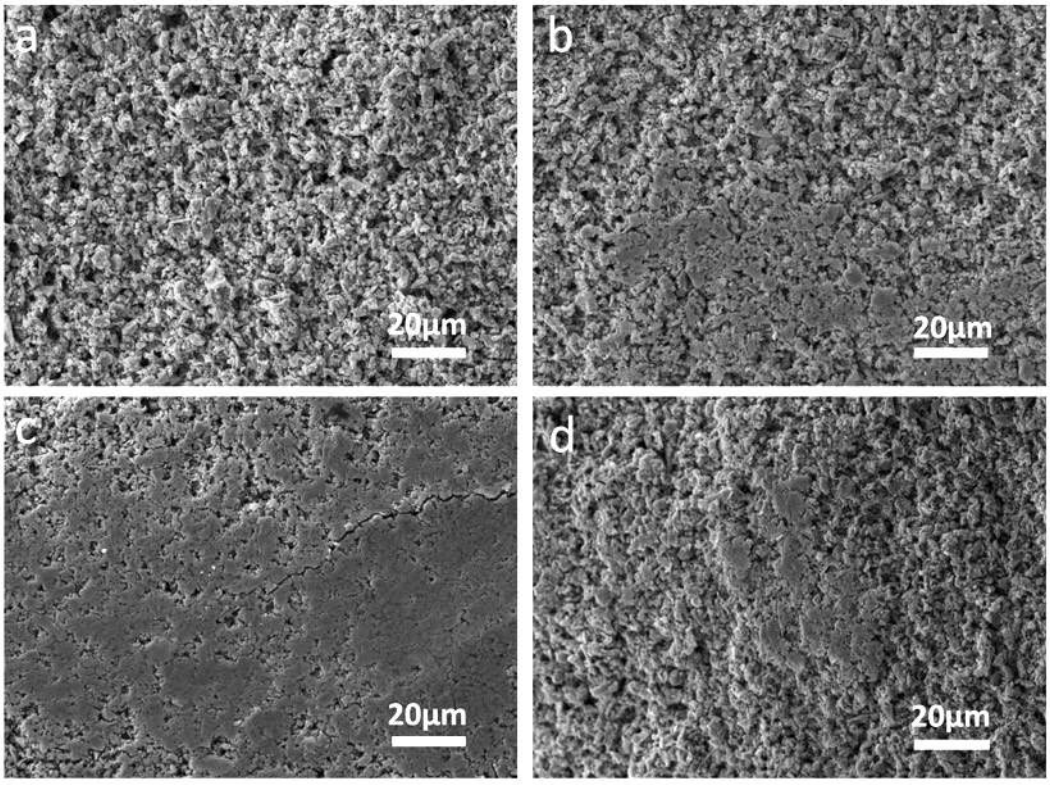

Figure 4.5 Surface SEM images of n-Bi_2Te_3/PEDOT:PSS composite samples annealed at (a) 423 K; (b) 593 K; (c) 623 K; (d) 673 K.

Figure 4.5 demonstrates the surface SEM images of n-Bi_2Te_3/PEDOT:PSS composite samples annealed at 423 K, 593 K, 623 K and 673 K, respectively. Different from the p-type composites materials, n-type composite particles tend to merge together with the increasing temperature treatments. The form of the particles are still random instead of aligned structure. The presence of PEDOT:PSS may affect this phenomenon. When temperature increases up to 593 K and 623 K, the PEDOT:PSS can connect the particles.

However, when the temperature reaches the 673K, the degradation of the polymers cannot combined the particles more, left some porous inside. Combined with the element analysis in **Table 4.1**, similar to the p-Bi_2Te_3/PEDOT:PSS composites, the temperature annealing treatment plays a significant role in compositions of p-Bi_2Te_3/PEDOT:PSS composites. The element analysis results show that the Se doping conducing to the p-type semiconducting formation. With increasing the annealing temperature, the S will decrease due to the gradationally decomposition of PEDOT:PSS. Identically, the Se reduces as the enhancing thermal treatment, the reason is that Se tends to vaporize during high temperature annealing process. Thus, the annealing process has an effects on the structure and composition of the composites but also the TE properties. The following influencing factors will be discussed in section 4.4.3.

Table 4.1 Composition of n-Bi_2Te_3 alloy samples annealed at 423 K, 593 K, 623 K, 673 K.

Samples	Constituent Ratio
n-type Bi_2Te_3	$Bi_2Te_{2.68}Se_{0.32}$
n-type Bi_2Te_3 - 423K	$Bi_2Te_{2.68}Se_{0.32}$
n-type Bi_2Te_3 - 593K	$Bi_2Te_{2.64}Se_{0.22}$
n-type Bi_2Te_3 - 623K	$Bi_2Te_{2.61}Se_{0.15}$
n-type Bi_2Te_3 - 673K	$Bi_2Te_{2.55}Se_{0.13}$

4.4.3 Thermoelectric performance of n-Bi_2Te_3/PEDOT:PSS composites and n-Bi_2Te_3 under different annealing temperature treatments

For the n-Bi_2Te_3/PEDOT:PSS composites, the annealing treatment is essentially the same for the p-type ones. Before the TE properties measurements, both n-Bi_2Te_3/PEDOT:PSS and pure n-Bi_2Te_3 samples have undergone the annealing processes at argon environment

with 423 K, 593 K, 623 K, 673 K for 3h, respectively. In this section, the temperature-dependent TE performance of all the n-Bi_2Te_3/PEDOT:PSS, n-Bi_2Te_3 and PEDOT:PSS samples are evaluated and analysed.

The temperature-dependent electrical conductivity of n-Bi_2Te_3, n-Bi_2Te_3/PEDOT:PSS, and PEDOT:PSS are displayed in **Figure 4.7 (a)**, respectively. All the electrical conductivities of the samples are measured from 298 K to 423 K. As the same in the Chapter 3, the mean electrical conductivity of PEDOT:PSS is 6.96×10^2 S/m. For the pure n-Bi_2Te_3 materials, in spite of the annealing temperatures, n-Bi_2Te_3 samples always exhibited advanced electrical performance when comparing with the composites. Generally, for the n-type materials, the degenerate semiconducting behavior is evident from the decrease in electrical conductivity for 593 K, 623 K, 673 K annealed n-Bi_2Te_3 samples with the increase in temperature. The electrical conductivities of all these four pretreatment n-Bi_2Te_3 samples are enhanced gradually with the increasing temperature annealing treatments. In light of the room temperature performance, the electrical conductivity are improve significantly from 169.45×10^2 S/m to 1255.60×10^2 S/m. In addition, the electrical conductivity of 673 K and 623 K- annealing samples are weaken with the increasing measuring temperature up to 423K, demonstrating a degenerate semiconductor behavior. On the contrary, the variations of electrical conductivity of 423 K,593 K-annealing samples become more gentle from room temperature to 423 K. One possible reason is accounting to the vaporization of Selenium (Se).(*124, 125*)

$$Bi_2Te_{(3-x)}Se_x = \left(2-\frac{2}{5}z\right)Bi_{Bi}^{X} + (x-y)Se_{Se}^{X} + ySe(g)\uparrow + yV_{Se}^{2+} + 2ye^- + (3-x-z)Te_{Te}^{X} + zTe(g)\uparrow + \left(\frac{2}{5}zV_{Bi}^{3-} + \frac{3}{5}zV_{Te}^{2+}\right) + \frac{2}{5}zBi_{Te}^{-} + \frac{2}{5}zh^+$$

With increasing the annealing temperature, the concentration improves, indicating the vacancies devote more electrons than the holes from the antisite defects. This is accounting

to the evaporation of Se during the high temperature process. In SEM figures, we know that the n-type material growth slower than the p-type ones, this crystal growth rate is conducive to improve the uniformity of macrostructures. However, once the growth rate lower to a certain degree, another affluent Te phase will occur in the n-type Bi_2Te_3, which will damage the performance of Seebeck coefficient. Regarding this point, this phenomenon did not happen in our pure Bi_2Te_3 and composite samples.

For the electrical conductivities of n-Bi_2Te_3/PEDOT:PSS composites, we also can use the percolation-like theory to analyze the connectivity in this disordered systems.(*101, 126-129*) Conductive composite is an complex material system, which made of conductive filler, according to the shape, which can be divided into particles, fibers, flakes, and polymer matrix (single or mixed group). There are many kinds of guides to explain the electrical path, however, the route formation models are not yet perfect, and there are more or less defects. It is necessary to make an analysis direct at the formation of the actual conductive polymer composite material system.

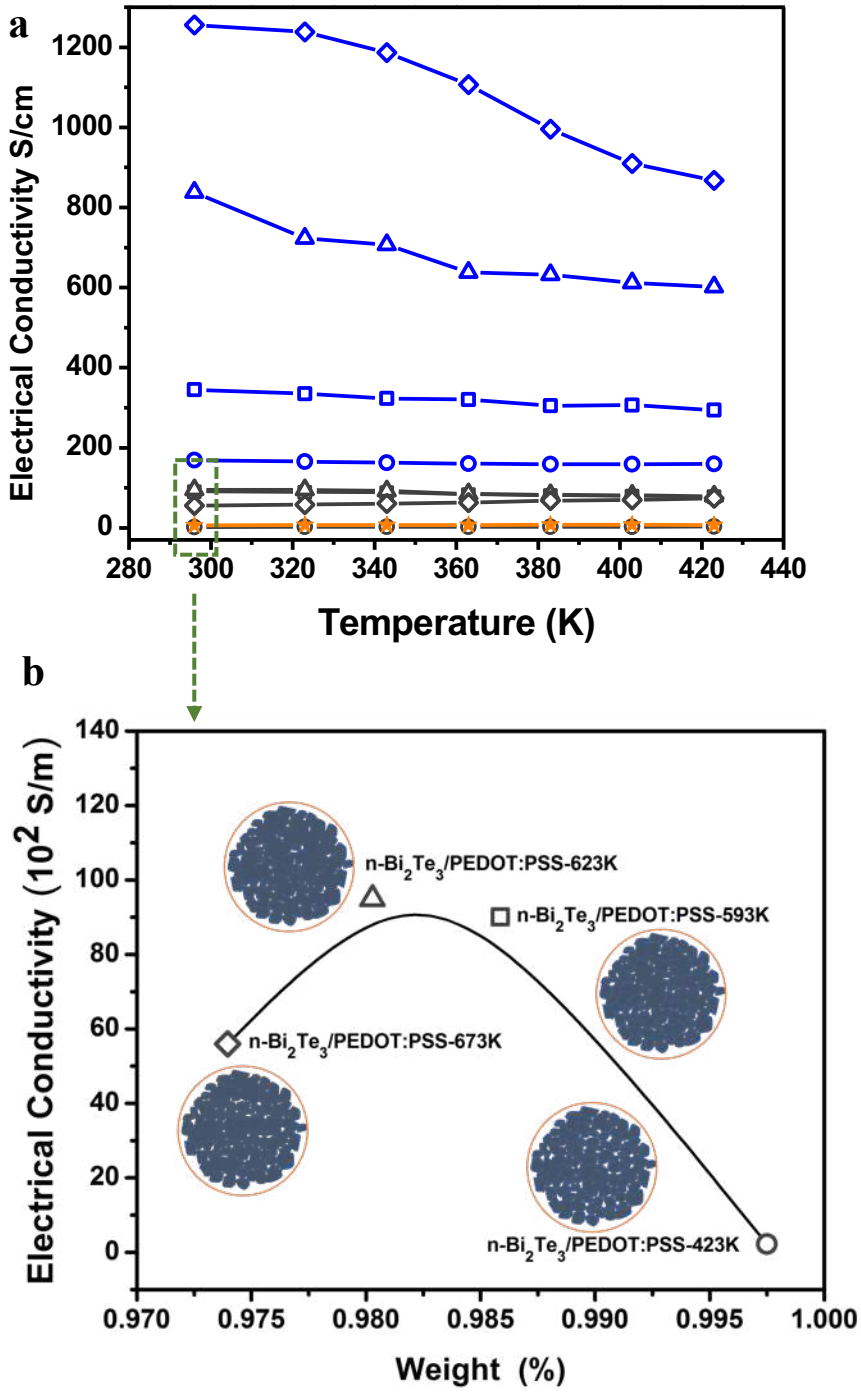

Figure 4.6 (a) Measured temperature-dependent electrical conductivity of n-Bi_2Te_3, n-Bi_2Te_3/PEDOT:PSS, and PEDOT:PSS, respectively. (b) Measured Room Temperature electrical conductivity of n-Bi_2Te_3, n-Bi_2Te_3/PEDOT:PSS, and PEDOT:PSS with the weight variance under annealing, respectively.

The conductivities of n-Bi_2Te_3/PEDOT:PSS composites produce an effect on the intrinsic properties of the n-Bi_2Te_3 and PEDOT:PSS matrix, and also influenced by the polymer-filler interactions. Combined with the TGA data discussed above, the measured room temperature electrical conductivity of n-Bi_2Te_3/PEDOT:PSS is derived with the weight variance under annealing pretreatment. **Figure 4.6 (b)** illustrates the four stages of the formation of the n-Bi_2Te_3/PEDOT:PSS composites. The first stage involves the precursor consists of n-Bi_2Te_3 particles, PEDOT:PSS and few organic insulated binders (p-Bi_2Te_3/PEDOT:PSS-423 K). The electrical conductivity of the 423 K-annealed sample at room temperature is 2.23×10^2 S/m, showing the lowest among the composite samples even lower than pure PEDOT:PSS. This result is deemed reasonable due to the presence of the PEDOT:PSS which can effective increase the initial density of the TE materials by filling up pores, promoting the flexibility of the sample while receding electrical property. When the annealing temperature up to 593 K, the composite comes to the second stage. At this stage, the low-boiling-point binders evaporate when the samples are heated at or above 423 K and the electrical conductivity of sample increases to 90.09×10^2 S/m. Apart from the reduction of organic binders, the decomposition of insulated PSS as the sulfonate groups disassociate from styrene also facilitated this performance. Then, the compact microstructure can be found in the third (p-Bi_2Te_3/PEDOT:PSS-623 K) and fourth (p-Bi_2Te_3/PEDOT:PSS-673 K) stage. Interestingly, unlike the pure n-Bi_2Te_3 materials, the best annealing condition with the highest performance of the n-Bi_2Te_3/PEDOT:PSS composites is 623 K. The room temperature electrical conductivity of 623 K- and 673K-annealed composite samples are about 94.89×10^2 S/m and 55.97×10^2 S/m, respectively. When the material gone through from first stage to third stage, the electrical conductivity enhances gradually and then reduces as the material arrive at the fourth stage. From first stage to third stage, with the increasing annealing temperature, the insulation PSS degrades

stage by stage. The degradation and re-orientation of the PEDOT:PSS may affect the electrical conductivity, and the PEDOT acts as the bridges to couple the Bi_2Te_3 particles, forming the crisscross circulation network between the particles, which facilitates the charge transport. In contrast with 673K- annealed p-Bi_2Te_3/PEDOT:PSS sample, the remain weight percentage of 673K- annealed n-Bi_2Te_3/PEDOT:PSS (97.4%) is higher than the p-Bi_2Te_3/PEDOT:PSS one (94.%). That means more PEDOT:PSS is left at this stage, in the meanwhile, more porous are occur because of the Se evaporation. The electrical performance are blunted since the PEDOT:PSS impeded grain growth instead. The reduced carrier mobility also confirmed this influence. Finally, the maximal percolation value is reached, at which peak, more adding fillers could not push carrier movement any further. As a whole, the evidences demonstrate the effectiveness of the enhancing annealing treatment for the n-Bi_2Te_3/PEDOT:PSS composites.

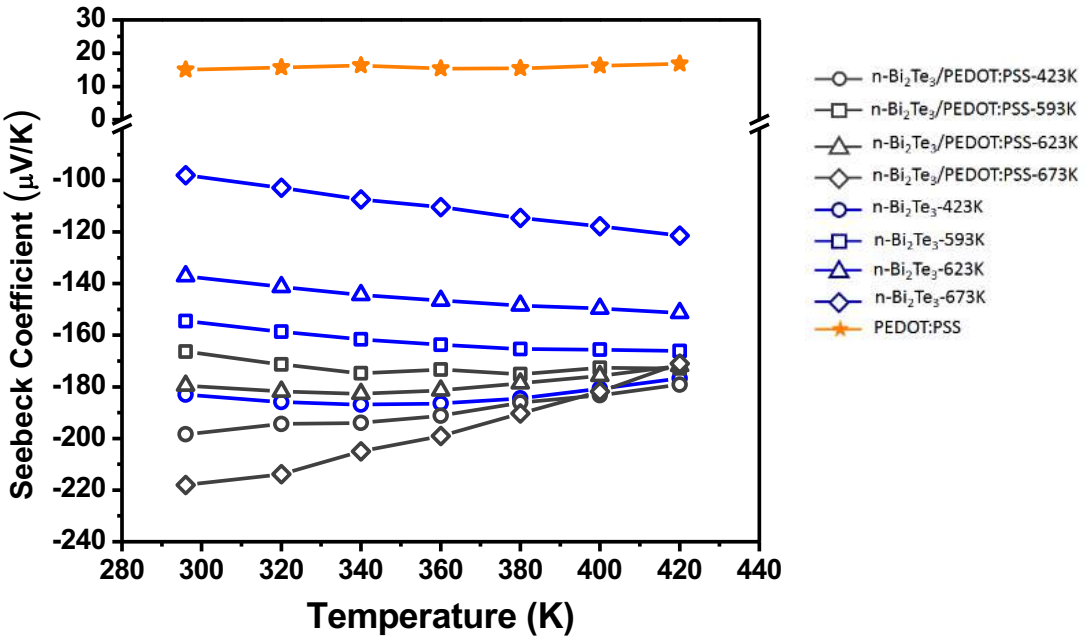

Figure 4.7 Measured temperature-dependent Seebeck coefficient of n-Bi_2Te_3, n-Bi_2Te_3/PEDOT:PSS, and PEDOT:PSS, respectively.

The temperature-dependent Seebeck coefficient of the n-Bi_2Te_3, n-Bi_2Te_3/PEDOT:PSS, and PEDOT:PSS samples from room temperature to 423K are shown in **Figure 4.7**. Traditionally, PEDOT:PSS is a representative p-type polymer, combining a strong n-type inorganic bulk material, for example SnSe, could not obtain high n-type performance.(*58*) Nevertheless, taking advantage of the high flexibility of PEDOT:PSS chains, noting that the PEDOT:PSS can potentially be de-doped by Bi_2Te_3 through electron transfer show the potential for inverting the nature of the majority charge carrier (from holes to electrons) in PEDOT:PSS, in principle, obtain n-type hybrids with promising TE properties. Here is found that, after cooperating with n-type Bi_2Te_3, the composites demonstrate n-type material behaviour and the Seebeck coefficient of the composites are greatly improved. Interestingly, with the same annealing temperature, the Seebeck coefficient of each composite is higher than the pure n-Bi_2Te_3. And the corresponding maximum value can be reached up to -218.0 μVK^{-1}, ascribing to the 673K- annealing composite sample. In general, the estimated near room temperature Seebeck coefficient of n-Bi_2Te_3 is found to vary from -98.0 μVK^{-1} to -183.0 μVK^{-1} and then further enhanced after addition of PEDOT:PSS as the composite. Differ from the p-Bi_2Te_3 ones, the raising annealing temperature drastically diminishes the Seebeck coefficient of the n-Bi_2Te_3 samples from -183.0 μVK^{-1} to -98.0 μVK^{-1} as the annealing temperature from 423K to 673K. If annealed above 593 K, the performance of n-Bi_2Te_3 show the improvement with the temperature from 296 K to 423 K. Surprisingly, for the n-Bi_2Te_3/PEDOT:PSS, the Seebeck coefficient of the composites reaches the same level as that of the pure n-Bi_2Te_3 which reported in other related works. This is partly due to the reduction of the carrier concentration. As we all know, Seebeck coefficient reflects intrinsic electron transport. Generally, the Seebeck coefficient can be predicted by the theory for metals and degenerate semiconductors with a parabolic band

and energy-independent charge carrier scattering depends on the carrier concentration of electrons or holes, n, and the effective mass, m*. (*126*)

$$s = \frac{8\pi^2 \kappa_B^2 T}{3eh^2} m^* \left(\frac{\pi}{3n}\right)^{2/3}$$

Where n is carrier concentration, S is Seebeck coefficient, κ_B represents Boltzmann constant, e means unit charge, h is Planck constant, m* is effective mass. Seebeck Coefficient directly depends on the measuring temperature (T) and inversely depends on the carrier concentration (n). Also, the electrical conductivity (σ) is related to the carrier concentration (n) and carrier mobility (μ) as follows $\sigma = ne\mu$, where e is the electron charge. In the low temperature range, the samples of 673 K- and 423 K- annealed exhibit exceeding performance comparing to the 623 K- and 593 K- ones. This propensity is in accordance with electrical performance. Owing to this intrinsic contradiction between S and s, the electrical conductivity and Seebeck coefficient of a material are seldom increased simultaneously. Here, the increase of electrical conductivity will lesson Seebeck coefficient of the samples.

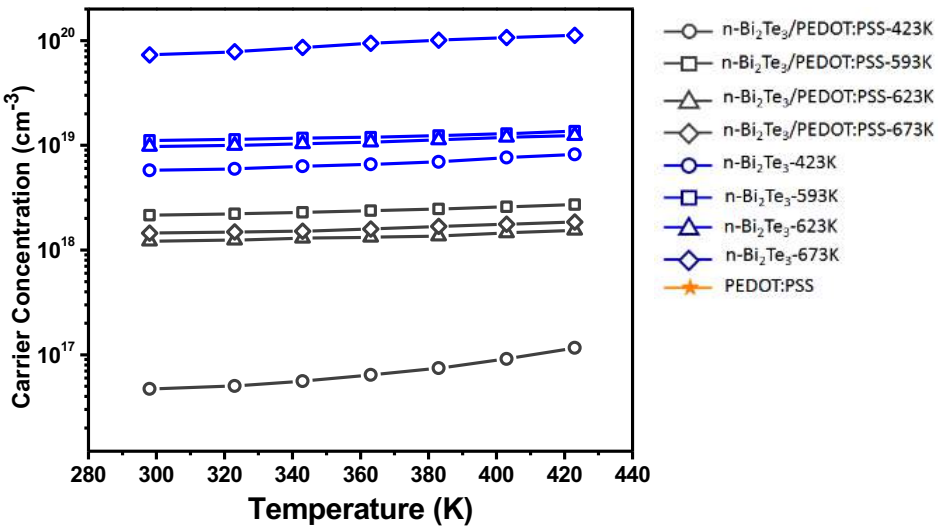

Figure 4.8 Measured temperature-dependent carrier concentration of n-Bi_2Te_3 and n-Bi_2Te_3/PEDOT:PSS, respectively.

It is well known that the electrical transport properties are sensitive to carrier concentration (n) and mobility (μ). For the n-Bi_2Te_3 samples, the carrier concentrations of the n-Bi_2Te_3 samples are above 1.45×10^{18} cm^{-3}. For the 423K-, 593K- annealed samples, the values are relatively low (1.45×10^{18} cm^{-3}-1×10^{19} cm^{-3}) compared to typical bulk Bi_2Te_3-based materials, which is responsible for the comparatively poor electrical conductivity of n-Bi_2Te_3 samples to the 623K-, 673K- annealed samples, as well as other related bulk materials. It is well studied that carrier concentration in $Bi_2Te_{3-x}Se_x$ is determined by the antisite defects (providing holes) and vacancies (providing electrons). With increasing the annealing treatment temperature, the concentration improves, indicating the vacancies contribute more electrons than the holes from the antisite defects. This is accounting to the evaporation of Se during the high temperature process. Se vacancies are more easily to be formed because of lower evaporation energy of Se (37.70 kJ/mol) than that of Te (52.55 kJ/mol), and thus provide electrons. On the contrary, the composites present relatively low concentration contrast to the pure n-Bi_2Te_3, which attributing to the high Seebeck coefficient.

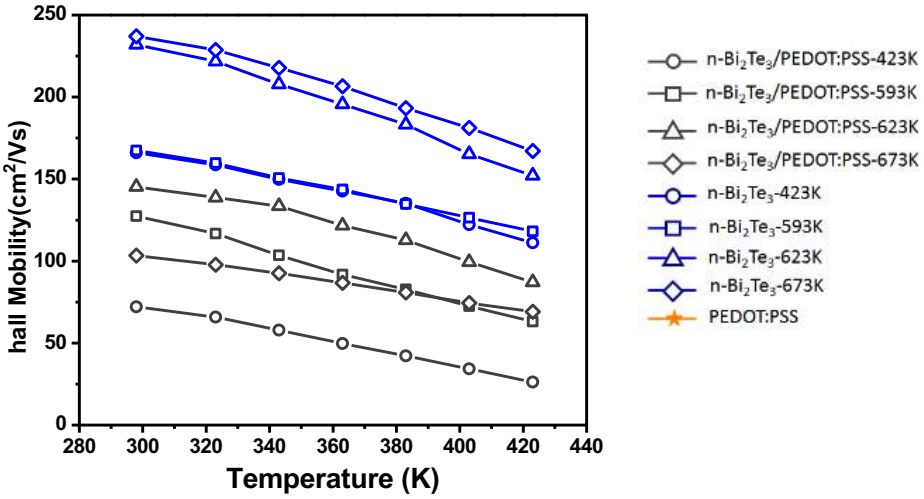

Figure 4.9 Measured temperature-dependent hall mobility of n-Bi2Te3 and n-Bi2Te3/PEDOT:PSS, respectively.

Apart from carrier concentration, we also use hall mobility to decipher the electrical properties of the samples. **Figure 4.10** presents the changes of mobility (μ_H) of annealed TE samples. The pores play an important role in charge carrier transport. (*130*) The whole inner mobility of the materials affected by the scattering, including phonon scattering, impurity scattering, defect scattering and etc. (*131*) The Matthiessen's rule below can explain this integrative action.(*132*)

$$\frac{1}{\mu_{tot}} = \frac{1}{\mu_{bulk}} + \frac{1}{\mu_{impurity}} + \frac{1}{\mu_{boundary}} + \frac{1}{\mu_{pore}}$$

The carrier mobility of the n-Bi_2Te_3 is varied from 72.1 $cm^2/V{\cdot}s$ up to 145.3 $cm^2/V{\cdot}s$ at room temperature according to the annealing treatment. Increasing annealing temperature process will facilitate the grain growth, thus attributing to the high mobility of the n-Bi_2Te_3 samples. Also, high temperature annealing caused a reduction in grain boundary and scattering center, which provide a long effective mean free path of carriers, attributing to the mobility enhancement. For the n-Bi_2Te_3/PEDOT:PSS, the case is more complicated. During the 423 K- to 623 K- annealed samples, the mobility is enhanced gradually. Cooperating with the low mobility of PEDOT:PSS (reported works: 2.5 $cm^2/V{\cdot}s$, 1.7 $cm^2/V{\cdot}s$),(*106, 107*) the corresponding μ value decreases in composites. The possible reason is that more phonons in the Bi_2Te_3/PEDOT:PSS composite than that of pure Bi_2Te_3, and thus increases carrier scattering, which tends to reduce mobility. The enhancement of the mobility is attributed to the presence of PEDOT and the Bi_2Te_3, providing the conducting path at the interfaces. However, when the temperature raising to the 673 K, the mobility reduce owing to the high porosity. Consequently, the relatively high number density of pores can result in the low electrical conductivity of 673 K- annealed composite sample.

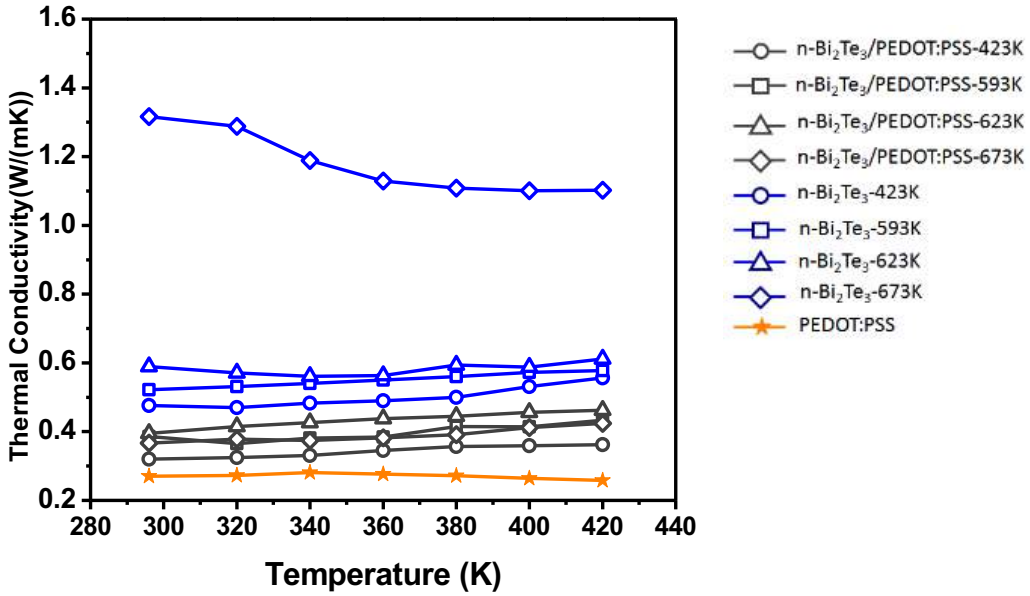

Figure 4.10 Measured temperature-dependent thermal conductivity of n-Bi_2Te_3, n-Bi_2Te_3/PEDOT:PSS and PEDOT:PSS, respectively.

The thermal properties of the n-Bi_2Te_3, n-Bi_2Te_3/PEDOT:PSS and PEDOT:PSS, respectively. are further discussed. The properties of n-Bi_2Te_3/PEDOT:PSS composites and n-Bi_2Te_3 samples annealed at 423 K, 593 K, 623 K, 673 K for 3 h, are investigated accordingly. In general, the annealing treatments have increased the thermal conductivity of all Bi_2Te_3 based samples, as illustrated in **Figure 4.10**. In addition, the thermal conductivity of PEDOT:PSS shows a weak temperature dependence, which phonon transport is dominant to the thermal conductivity.(*133*) The temperature-dependent thermal conductivity of the n-Bi_2Te_3 samples is 0.46 - 1.5 $Wm^{-1}K^{-1}$ over the entire measured temperature range, which is lower than that of the composite materials (0.32 - 0.54 $Wm^{-1}K^{-1}$). The higher the annealing temperature, the greater the thermal conductivity. In this composite system, the lowest thermal conductivity was 0.28 $Wm^{-1}K^{-1}$ (annealed at 423K), owing to the thermally insulating PEDOT:PSS polymer of ~0.32 $Wm^{-1}K^{-1}$,

formation of pores and interface between the particle and matrix. The highest thermal conductivity of composite is 0.53 $Wm^{-1}K^{-1}$, annealed at 623K. The reason of the low thermal conductivity of 423 K, 593 K annealed composite samples is because of the thermal insulated PEDOT:PSS. This is different from the 673 K annealed sample, the porous act as the thermal blockers instead. On the other hand, the limited phonon mean free path in this composite system can effectively reduce its thermal conductivity. The thermal conductivity, κ, of a material can be divided into two heat carriers, phonons of the lattice, κ_l, and electrons, κ_{elec}. The phonon thermal conductivity, κ_l, is expressed by the Boltz-mann equation,(*21*) $\kappa_l = \frac{1}{3}\sum_{\lambda\kappa} C_{\lambda\kappa}\, v_{\lambda\kappa}\Lambda_{\lambda\kappa}$, where $C_{\lambda\kappa}$, is specific heat, $v_{\lambda\kappa}$is group velocity, $\Lambda_{\lambda\kappa}$ is mean free path, respectively. The limited phonon mean free path in this composite system can effectively reduce its thermal conductivity. Thermal conductivity is also influenced by the morphology via scattering mechanism. By adding scattering centers, or by heat-induced degradation of PEDOT:PSS, or by inducing micro-rough surface due to annealing, the thermal conductivity can be effectively reduced.

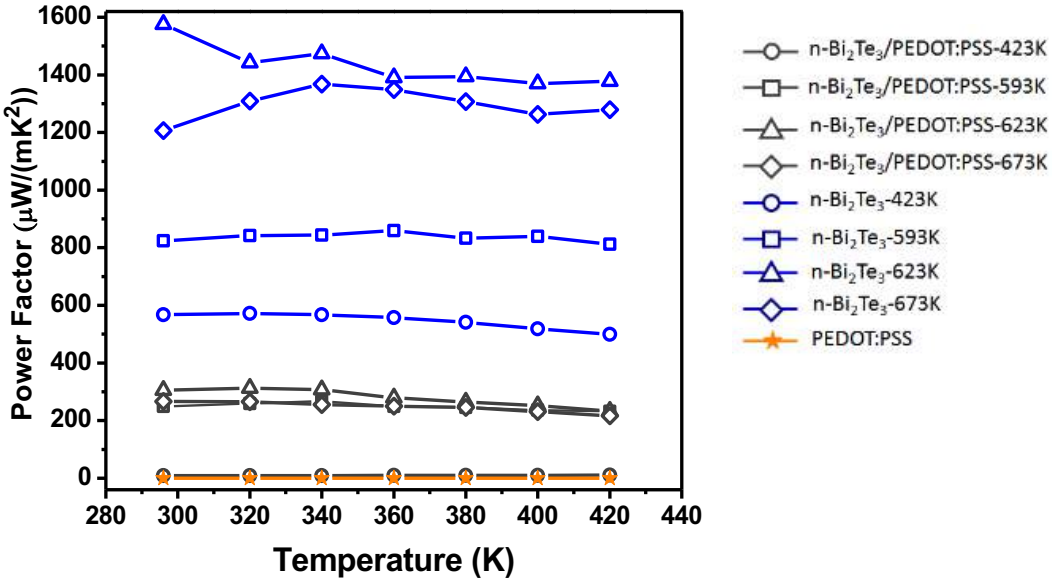

Figure 4.11 Temperature-dependent power factor of n-Bi_2Te_3, n-Bi_2Te_3/PEDOT:PSS, and PEDOT:PSS, respectively.

The power factor are plotted in **Figures 4.11**. The power factor (PF) for the sample can be obtained by using the relation of $PF = S\sigma^2$, where S and σ are Seebeck coefficient and electrical conductivity, respectively. The average power factor of PEDOT:PSS is about 0.175 $\mu Wm^{-1} K^{-2}$. The maximum power factor of the n-Bi_2Te_3/PEDOT:PSS composite is 306 $\mu Wm^{-1} K^{-2}$, obtained from the sample annealed at 623K. The power factor for n-type composite is from 9 $\mu W m^{-1} K^{-2}$ to 306 $\mu Wm^{-1} K^{-2}$ and this index is less than that of p-type congeneric materials (500-1575 $\mu Wm^{-1}K^{-2}$). However, the result is still very encouraging because previously reported n-Bi_2Te_3/PEDOT:PSS hybrid composite materials showed much inferior TE properties compared to that of original inorganic material. For the pure n-Bi_2Te_3 materials, the power factor ranges from 500 $\mu W m^{-1} K^{-2}$ to 1575 $\mu Wm^{-1} K^{-2}$. And the optimal power factor of 623 K annealed n-Bi_2Te_3 sample in this work is comparable to the traditional n-$Bi_2Te_{3-x}Se_x$ sample. This enhancement is attributed to the optimized carrier concentration and increased carrier mobility.

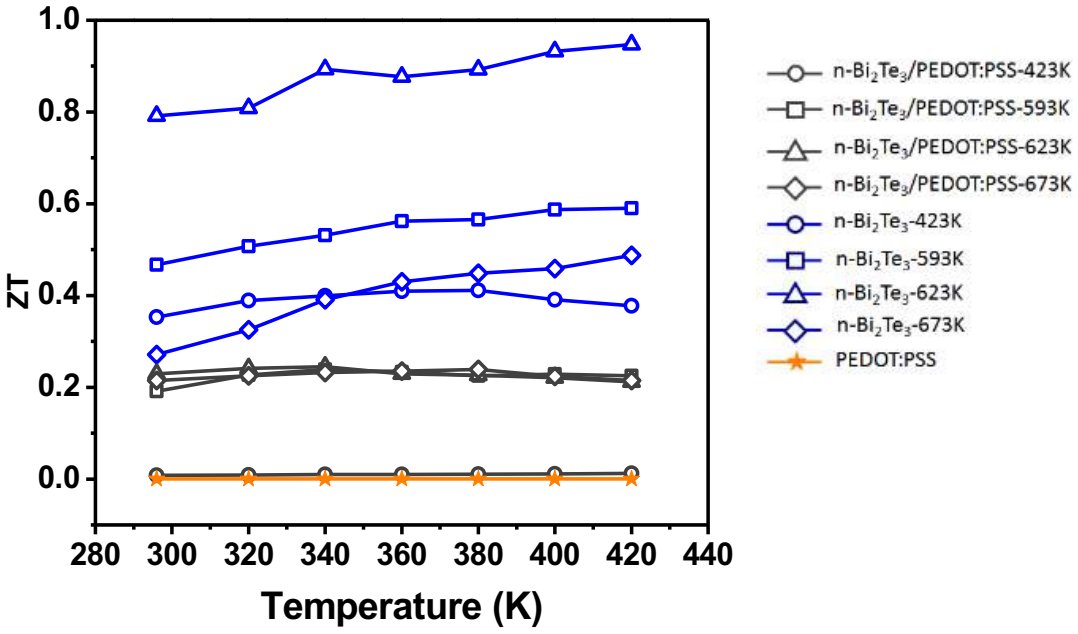

Figure 4.12 Temperature-dependent figure of merit of n-Bi_2Te_3, n-Bi_2Te_3/PEDOT:PSS, and PEDOT:PSS, respectively.

The low thermal conductivity and high Seebeck coefficient resulted in high peak ZT values of 0.26 for n-Bi_2Te_3/PEDOT:PSS TE materials.(**Figure 4.12**) Under 673K annealed temperature, the PEDOT:PSS would decompose and the electrical of this sample was a little bit higher than that of the rest composite ones. However, due to the lower thermal conductivity of the composite, the performance of samples annealed of 623K exhibits figure of merit of 0.23 at 296 K. Though the power factor of 423K annealed n-Bi_2Te_3 is the lowest, its ZT value increases with annealing temperature while the others decrease within the same temperature range. This is partially attributed to the relatively low thermal conductivity brought by low-temperature annealing. Generally, the power factor and ZT of the composites are always lower than those of the pure n-Bi_2Te_3, respectively. It is reasonable as a homogeneous composite composed of disparate ingredients working separately cannot have a higher power factor or ZT than that of any single component. However, the highest power factor and ZT of the composite samples are comparable to the bulk n-Bi_2Te_3 samples near room temperature (refer to the green gridlines) while the composites fully demonstrate highly flexibility. In terms of the power factor, the fairly high Seebeck coefficient of the composites benefit to power performance. On the part of ZT value, the low thermal conductivity resulted in high peak ZT values for n-Bi_2Te_3/PEDOT:PSS material. Our results deconvolve that inorganic-organic strategy is eminently suitable for high-performance flexible TE generators compared with the established protocols.

4.4.5 Comparison with previously reported work

Table 4.2Thermoelectric performance of the n-Bi2Te3/PEDOT:PSS composites compared with other related work in the literature at the room temperature

Table 4.2 Thermoelectric performance of the n-Bi_2Te_3/PEDOT:PSS composites compared with other related work in the literature at the room temperature.

Sample	Carrier	S /	σ/	κ /	PF /	ZT	Ref.
n-Bi_2Te_3/ PEDOT:PSS-423K	n	-198.35	2.23	0.32	8.79	0.0081	**This**
n-Bi_2Te_3/ PEDOT:PSS-593K	n	-166.35	90.09	0.35	249.29	0.21	**work**
n-Bi_2Te_3/ PEDOT:PSS-623K	n	-179.52	94.89	0.39	305.79	0.23	
n-Bi_2Te_3/ PEDOT:PSS-673K	n	-218.02	55.97	0.43	266.03	0.18	
n-Bi_2Te_3/ 10 vol% Clevios PH1000	n	~ -140	~50	/	80	/	(*58*)
n-Bi_2Te_3/ 17 vol% Clevios PH1000	n	~ -80	~100	/	70	/	
n-Bi_2Te_3/ 23 vol% Clevios PH1000	n	~ -70	~140	/	75	/	
n-Bi_2Te_3/ 30 vol% CLEVIOS FE-T	n	~ -80	~60	/	40	/	
n-Bi_2Te_3/ 45 vol% CLEVIOS FE-T	n	~ -40	~105	/	20	/	
n-Bi_2Te_3/ 55 vol% CLEVIOS FE-T	n	~ -10	~120	/	5	/	
80% n-Bi_2Te_3/ PEDOT:PSS	n	~ -70	16	/	~16	/	(*60*)
0.6wt% n-type Bi_2Te_3/	n	~ -15.7	7.78	/	0.19	/	(*120*)
n-Bi_2Te_3/ PEDOT:PSS	n	-137.8±2.8	73±0.04	0.25±0.01	137	0.16±0.01	(*59*)

The TE performance of n-Bi_2Te_3/PEDOT:PSS composites are compared with the previously reported work, as shown in **Table 4.2**. Although a few results of p-Bi_2Te_3/PEDOT:PSS materials were reported sporadically, the power factors of n-Bi_2Te_3/PEDOT:PSS materials are gradually improved in recent years. The best TE performance from the current work have been demonstrated for n-Bi_2Te_3/PEDOT:PSS composites. Zhang and co-workers fabricated a serious of n-type composites with commercial PEDOT products (CLEVIOS FE-T, PH1000) volume percent from 10% to 55% which have a power factor from 80 to 5 $\mu Wm^{-1}K^{-2}$.(*58*) The corresponding Seebeck coefficients are range from -140 to -10 mV/K. Another well studied flexible screen printed n-Bi_2Te_3/PEDOT:PSS TE film were first reported by We and co-workers, achieved a remarkable power factor of ~73 $\mu Wm^{-1}K^{-2}$, Seebeck coefficient of -137 mV/K.(*59*) Sahu et al. and Rahman et al. demonstrated the complex hybrid thermoelectric systems, obtaining a maximum power factor of 16 $mWm^{-1}K^{-2}$ by adding nearly 80% wt of Bi_2Te_3 in the composite. By comparing these related reported works, the as-fabricated 673K-annealed p-Bi_2Te_3/PEDOT:PSS composite has achieved the highest Seebeck coefficient of -218.02 $\mu V/K$ among all other Bi_xTe_y/PEDOT:PSS composite materials reported so far, demonstrating approximately 1.6~21.8 times higher than the reported Bi_2Te_3 alloy nanosheet/PEDOT:PSS composite fabricated by drop casting techniques (-140 to -10 $\mu V/K$), 1.59 multiples higher than that of PEDOT:PSS/Bi_2Te_3-nanowires (14.9 $\mu V/K$, 16.3 $\mu V/K$, 54 $\mu V/K$) prepared by screen printing method, 3.11 times of Bi_2Te_3/PEDOT:PSS by casting and dipping method. Also, the most improved power factor of 623K-annealed p-Bi_2Te_3/PEDOT:PSS composite achieves 305.79$\mu Wm^{-1}K^{-2}$.

4.6 Conclusions

In this Chapter, flexible solution processible n-Bi_2Te_3 /PEDOT:PSS TE materials are investigated. N-type Bi_2Te_3/ PEDOT:PSS TE composites were fabricated and annealed at different temperature (423 K, 593 K, 623 K, 673 K). The measured thermal conductivity of the resultant composites is within the range from 0.32 to 0.54 $Wm^{-1}K^{-1}$, and their Seebeck coefficient from -166.3 to -218.0 μV/K with power factors from 8.79 to 305.79 $\mu W/(m \cdot K^2)$ near room temperature, respectively. The composites reach the same high Seebeck coefficient value as that of the pure n-Bi_2Te_3, reduce their thermal conductivity and electrical conductivity. The first two effects bring out positive benefits to TEG performance, however, the reduced electrical conductivity is not desirable. In this work, the achieved highest figures of Seebeck coefficient and power factor are -218.02 μV/K and 305.8 $\mu W/(m \cdot K^2)$, respectively. They outweigh by a large margin over other previously reported works on TE composites and even comparable to the rigid pure n-Bi_2Te_3 near room temperature. The outstanding TE performance of the solution-processible n-type Bi_2Te_3/ PEDOT:PSS composites have demonstrated the great application potentials and advantages not available to conventional rigid inorganic thermoelectric devices. Both p-type Bi_2Te_3/ PEDOT:PSS and n-type Bi_2Te_3/ PEDOT:PSS composites will be designed to function practical applications of flexible and wearable TEG modules in Chapter 5.

Chapter 5 FLEXIBLE AND WEARABLE THERMOELECTRIC GENERATORS

5.1. Introduction

Harvesting thermal energy from three-dimensional complex shaped objects or human body requires a generator device with low rigidities of bending, in-plane shear and tensile deformation so that intimately close contacts and efficient heat transfer can be achieved between the generator and heat source. Therefore, light and flexible thermoelectric generators working at room- or low-temperature are much desirable for applications of wearable microelectronics, IoT, active microclimate controlling systems and waste heat utilization.(*7-12*)

An output power in the order of mini-watts from an FTEG, operating within a temperature difference of ~50 K, is required for driving common wearable microelectronic and IoT devices working at near room temperature. The FTEG output performance depends on its functional and structural materials, device structural design and fabrication process. At present, heavy and rigid semi-conductor functional and structural materials have been used to fabricate most thermoelectric generators that require annealing at high temperature, at which most polymers or fibers cannot survive. While the generators equipped with rigid thermoelectric (TE) semiconductors can reach the required output power, flexible polymeric TE materials do not offer such high performance and long-term stability. New high-performance flexible TE materials must be developed so that they can be processed via cost-effective operations at room- or low-temperature for FTEG fabrication. The state-

of-arts flexible TE precursor materials are in the solution form, which normally consists of inorganic semiconductors, organic binder or organic conducting polymers. They can be printed, painted, or drop casted, followed by drying or curing processes at an elevated temperature,[8] in order to form solid TE materials or structures. To fabricate FTEGs from such precursors, a great difficulty is that the inevitable organic-conducting binders residuals between the semiconducting particles bring down the TE performance. Compromise may be necessary to strike a balance between the flexibility and performance of FTEGs.

In Chapter 3 and 4, flexible p-type and n-type Bi_2Te_3/PEDOT:PSS materials were discussed. Sequentially, the application of these two materials will be presented in this chapter. Since the rigid and unwieldy TEGs are not suitable for wearable application, two types of device structures (film structure, sandwich-like structure) will be designed for self-powering. In the film structure FTEG, both flexible TE materials and substrates are needed. Different from the film design, sandwich-like configuration consists of rigid TE materials and flexible substrates. As discussion in the chapter 2, most TE materials used in works either focus on the film structure or sandwich-like configuration. To our best knowledge, up-to-date, no comparative work has reported on flexible TEG devices which are based on the same materials systems. This is important since this investigation can help the researchers to design optimal FTEGs based on different form of the materials.

The fabrication of thin film type FTEGs has been supported by technological advancement in recent years. Generally, film FTEG employs conducting polymers, inorganic/organic materials or graphene based flexible materials. Owing to their solution processability, printing technologies, such as 3D printing,(*17*) screen printing(*134*) and blade coating(*135*) have introduced a revolution in FTEGs manufacturing. In 3D printing, various patterns can be designed digital, then transform into physical subject by layer-by-layer building process.

After the printing process, patterned regions composed of resins, powders or inks are solidified to yield the desired object forms.(*136*)

J. Peng and co-workers(*127*) reported FTEG modules based on the n- or p-type Bi_2Te_3 inks fabricated by 3D printing technology, followed by the roller compression. The resulting film was compact and the power factors of both n- and p-type materials were improved up to 7 orders-of-magnitude after pressing solidification. These strategies promoted the electric conductivity of the materials by reducing the microporosity and partial aligning the micrograins. Both p-type and n-type threads were aligned on Kapton thin films connected by the in-plane or cross-plane electrodes, functioned in the parallel and transverse directions, respectively.

Blade coating is also a popular thin-film fabrication technique.(*137*) The solution can spread over the masked area between the blade and the substrate, forming the thin film. The final thickness of the film will be influenced by the viscoelastic properties of the materials and the speed of coating. Generally, this process is scalable, so this process can used to large-quantity of TE films on an industrial scale.(*138*)

For the sandwich-like structure, most devices consist of rigid semiconductors, and require high temperature post treatments. This is distinct from the film one. Cho's group(*15*) developed several lightweight wearable FTEGs via screen printing. In their work, both n-type (Bi_2Te_3) and p-type (Sb_2Te_3) TE pastes were printed through a glass fabric, which serves as the flexible and insulating substate, forming the wearable electronics. Bi_2Te_3 and Sb_2Te_3 printed dots were gone through annealing treatment at 530 ^oC in N_2 atmosphere for crystallization and densification of the TE materials. A high temperature tolerant substrate is required for the flexible and wearable TE applications if the integration of TE materials and electrodes are implemented before the thermal treatment. (*15, 139, 140*)

As discussed in Chapter 3 and 4, the annealing treatment played an important role in the TE performance as well as the flexibility. When the Bi_2Te_3/PEDOT:PSS composites go through 423 K treatment, the samples will exbibit highly flexibility while demonstrating relatively low TE performance. Then, the materials performance is enhanced with increasing treatment temperature while the flexibility is deteriorated. For the p-Bi_2Te_3/PEDOT:PSS, the figure-of-merit reaches a maximum under 673 K annealing process. For the n-Bi_2Te_3/PEDOT:PSS, the optimal property can be obtained with 623K annealing process. Thus in this Chapter, both the low temperature and high temperature treatment will be investigated for the film and sandwich type FTEGs.

5.2 Experimental

5.2.1 Preparation of materials

Preparation of p-/n-Bi_2Te_3/PEDOT:PSS hybrid ink paste: The materials used in Chapter 5 are identical to Chapter 3 and Chapter 4.

5.2.2 Fabrication of the film structure FTEGs

Fabrication of PDMS film substrate**:** Solid PDMS (supplier) (20 g) was dissolved in 250 mL tetrahydrofuran thoroughly. The resultant solution (24 mL) was vacuumed to remove air and then added slowly into a teflon holder (10 cm × 10 cm × 1 cm). In the holder, the film was cured at 23 ^{o}C for 24 h. After solidification, the resultant flexible silicone film was peeled off from the teflon holder. The film thickness was about 200 μm.

Fabrication of Bi_2Te_3/PEDOT:PSS film on flexible substrates via 3D printing: The Bi_2Te_3 (p-type and n-type)/PEDOT:PSS TE films were made by using a 3-D printing technique

(3D Bioplotter® Manufacturer Series). The noddle diameter used was 200 μm, the printing pressure was 0.2 bar, and the nozzle feed rate was fixed at 10mm/s. When the printing pressure was higher or lower than 0.2 bar, the ink could not be printed due to liquid spreading or nozzle clogging, respectively. Moreover, the viscose ink did not flow out of the needle in a heterogeneous material system. Various flexible substrates have been used in this fabrication, including PVA paper, PDMS paper, PI papers and fabrics.

The process consists of three steps: 3-D printing, drying and annealing. Firstly, p-type and n-type Bi_2Te_3/PEDOT:PSS paste were printed on the paper via 3-D printing (3D-Bioplotter® Manufacturer Series), respectively. The printing steps are as follows: p-type and n-type Bi_2Te_3/PEDOT:PSS paste was printed on a water-soluble paper using the low temperature head at 10 mm/s, under 0.2 bar pressure, with 0.2 mm one layer height, and 0.2 mm extrusion width. The printed film was dried at 70 ^oC for 15 min and 90 ^oC for 15 min to remove organic residues, and then underwent an annealing process at 150 ^oC for 5 min under vacuum.

Fabrication of Bi_2Te_3/PEDOT:PSS film on flexible substrates via blade coating: Blade coating is a technique that is well suited for large-scale coatings. The technique is also compatible for creating thicker films from a viscous solution. Varied flexible substrate based TE films were blade coated with p-type and n-type Bi_2Te_3/PEDOT:PSS pastes via K control coater (RK PrintCoat Instruments Ltd., UK). The control speed is 5m/min and the used bar is No.3.

Fabrication of PDMS-based p-Bi_2Te_3/PEDOT:PSS FTEG: The 3D printed TE film on water soluable paper was transferred and conglutinated onto a PDMS film. The 20% H_2SO_4 solution was added carefully on the reverse side of water-soluble paper to dissolve the paper substrate. After 10 s infiltration, the paper can be peeled off from TE materials. Thus, the

p-type Bi_2Te_3/PEDOT:PSS based TE film was transferred to the PDMS film substrate successfully. After that, a conductive silver thread was adhered on both ends of TE film to form the electrodes. In order to increase the conductivity of silver thread, nano Ag was deposited on the thread at room temperature by using a magnetron sputtering system (ZZG/JT-350). After electrode fabrication, a flexible PDMS film was conglutinated on the flexible TE film to make the sandwich-structured FTEG.

5.2.3 Fabrication of the sandwich-like structure FTEGs

Both p-Bi_2Te_3/PEDOT:PSS and n-Bi_2Te_3/PEDOT:PSS films were dried at 623 K under argon condition for about 3 h. Afterwards, the films became powders. Then, the sample powders were under hot pressing process to obtain the TE pillars. In this process, the powder was filled into a graphite die then placed in a hot-press system for the thermal treatment. The p-Bi_2Te_3/PEDOT:PSS sample were hot pressed at 673 K under a pressure of 1.2 GPa for 1 h in argon. The n-Bi_2Te_3/PEDOT:PSS sample were hot pressed at 623 K under a pressure of 1.2 GPa for 1 h in argon. Subsequently, the chamber was filled with Ar and the sample was heated with a rate of 5 K/min to the selected temperatures, and then was cooled down to room temperature naturally. The final products were ready for chips engineering. After TE pillars preparation, the p/n-type TE legs were connected by the flexible electrodes as shown in Figure 5.12. Finally, sandwich-type FTEG was completed.

5.2.4 Evaluation method of FTEG performance

The FTEG output performance was measured using a lab-made system that includes a Keithley 2700 multimeter, Whatlent TEC temperature Control, and Anbat AT4516

temperature detector together with a temperture difference unit using. The output voltages were measured by Keithley 2700 and temperature difference of self-assembled devicewas tested by Anbat AT4516 simultaneously.

Figure 5.1Measurement system of TEG performance

A lab-made TE measurement system was used to evaluate the TE performance of the FTEGs. A photograph of the whole test system is demonstrated in **Figure 5.1**. This system is used to determine the output power and efficiency of a flexible/commercial thermoelectric generator with a given temperature gradient. In the system, the volmeter and temperature detector are used for output voltage and temperature difference recording. A temperature control system including a pump and cooling water tank is used to cooling down the whole system. Heating is achieved by electric joule heating element. The resistor is loaded for measurement. A external load resistance is selected to match the internal device resistance to obtain the maximum power.

For the FTEG Demonstration, the whole demo system were assembled with FTEG module, LED lights, heat/cold sink, and reusable connectors. The demo setup can show us the

potential of FTEG, roughly predict how much energy generated from the device can be fully applied. Simply locate the FTEG on heat/cold sink, then offer the temperature difference on the top and bottom surface of the FTEG and watch the decorative LED light up in seconds.

The Kit includes Demo Board (LTC3108EDE-1 - Ultralow Voltage Step-Up Converter and Power Manager), FTEG, Decorative LEDs, four reusable connectors and temperature control.

5.3 The Flim Type FTEG

5.3.1 Fabrication process of flexible FTEG

The rheological properties of the TE inks plays an important role in the feasibility of 3D printing. The big challenge here is to fabricate the printable TE inks which can be squeezed out from the pinhead steadily and formed the desired structure. **Figure 5.2** illustrates viscosity of p-type and n-type TE ink at room temperature. As described in the experimental part, the proportion of p- and n-Bi_2Te_3/PEDOT:PSS ink systems is the same. However, the viscosity of n-Bi_2Te_3/PEDOT:PSS is 24000 mPa·s, which is lower than that of the p-Bi_2Te_3/PEDOT:PSS (32000 mPa·s). One possible reason is that an increased size particle of p-Bi_2Te_3 enhances the probability of agglomeration phenomena, resulting an increase of ink viscosity. Because the larger granules have greater inertia which induce the clustering. Interestingly, despite of the difference in viscosity, both p-Bi_2Te_3/PEDOT:PSS and n-Bi_2Te_3/PEDOT:PSS inks can execute the expected functions of 3D printing, as following the structure solidification.

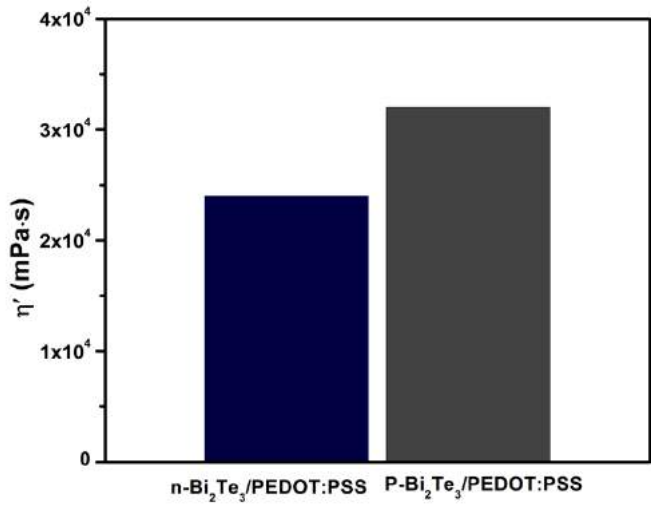

Figure 5.2 Viscosity of p-type and n-type TE ink.

The 3D printable TE ink pastes enable the FTEG prototype design and fabrication. **Figure 5.3a** shows the 3D printing machine (3D Bioplotter) and its enlarged image illustrates the p- and n-type Bi_2Te_3/PEDOT:PSS inks used for printing, respectively. The ink was prepared based on a well-dispersed mixture of Bi_2Te_3 powder and PEDOT:PSS, with addition of DMSO, isopropanol and α-terpineol. During the mixing process, Bi_2Te_3 powder and PEDOT:PSS were immersed into organic solvent, forming a homogeneous structure. The powder had various sizes such that the small particles of Bi_2Te_3 powder occupied the interspace between the bulky particles, enhancing the system packing density. The constituent components served different purposes: Bi_2Te_3 powders and PEDOT:PSS were engineered for TE function; DMSO was added to increase the conductivity of PEDOT:PSS; Isopropanol and α-terpineol were used to adjust the system viscosity. The parameters have been considered and adjusted including printing pressure, materials concentration, needle diameter and needle feed rate to ensure good printability.

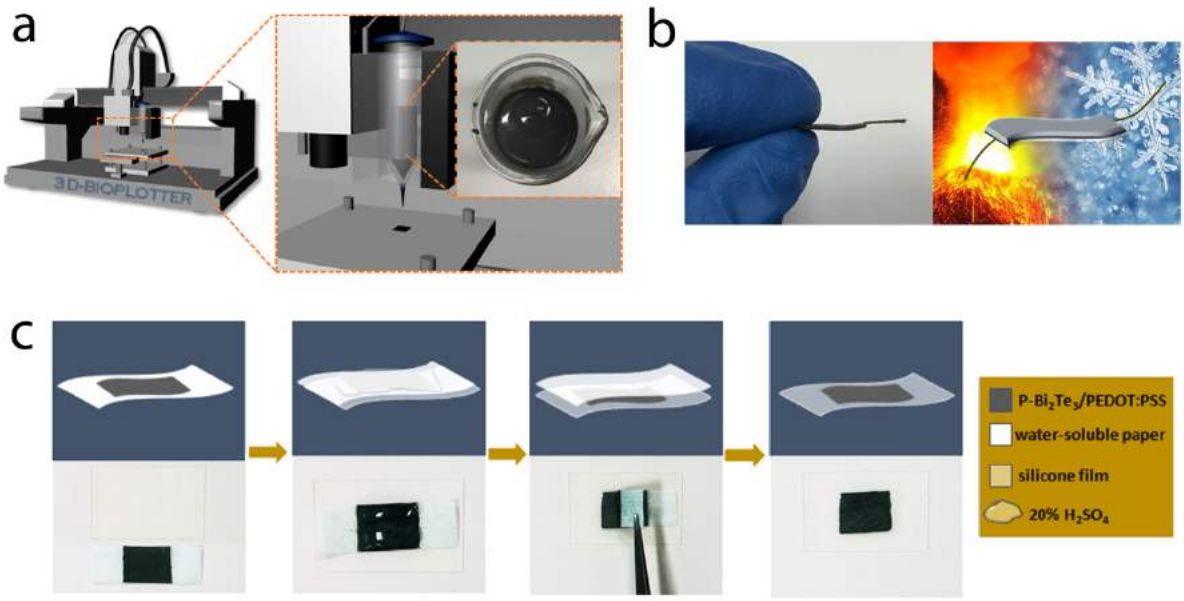

Figure 5.3 (a) Schematic illustration of 3-D printing process of TE film and p-Bi_2Te_3/PEDOT:PSS paste (inset). (b) Photographic image (left) and operation schematic diagram (right) of laterally sandwich-like FTEG. (c) Schematic diagram of substrate transfer of flexible TE film.

Figure 5.3 c describes the substrate transfer of the flexible TE film to PDMS substrate in the following steps: The prepared p-Bi_2Te_3/PEDOT:PSS ink was disperse printed on a water-soluble PVA paper, which acted as the precursor for FTEG (**Figure 5.3 a**). Then the TE film on PVA paper was transferred and conglutinated on the flexible PDMS film, 20% H_2SO_4 solution was added carefully on the reverse side of water-soluble PVA paper to separate the TE film from the paper substrate. After infiltration for 10 seconds, the paper was breezily peeled off from the TE film. Thus, the p-Bi_2Te_3/PEDOT:PSS film was transferred to the PDMS film successfully. Note that the infiltration time was vital to this seceding step. Finally, a conductive silver yarn was adhered by sliver paste on both ends of the TE film to form the electrode. TE films with a typical size of 30 mm × 15 mm × 0.2 mm were made. The printed TE microstructures provided a mechanically soft, robust

matrix and ensured the sub-sequential operation of substrate transfer. Finally, the laterally sandwich-like FTEG was achieved, which is demonstrated in **Figure 5.3 b**. The FTEG with the dimension of 3.0 mm × 10.0 mm × 0.7 mm was thin, lightweight and flexible.

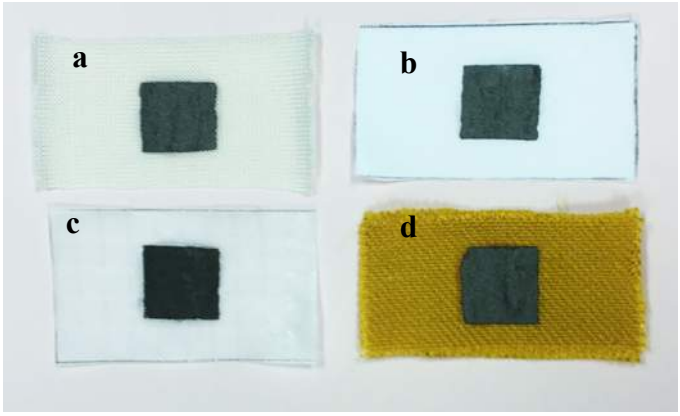

Figure 5.4 Image of flexible TE film fabricated on different substrates via subtract transfer. (a)PHBV-PLA fabric, (b) PET fabric, (c) Glass fabric, (d) Polyimide fabric.

Figure 5.5 Image of 5 layers of p-Bi_2Te_3/ PEDOT:PSS based flexible TE film.

Furthermore, this synthetic combination of inorganic-organic strategy and substrate transfer method were used to fabricate TE generators on various substrates, such as polyimide fabric and poly (3-hydroxybutyrate-co-valerate)/ polylactide (PHBV/PLA) filament and also can form the layer by layer structure. (**Figure 5.4, Figure 5.5**). The adhesion of the transfer TE film to substrates should be mentioned.

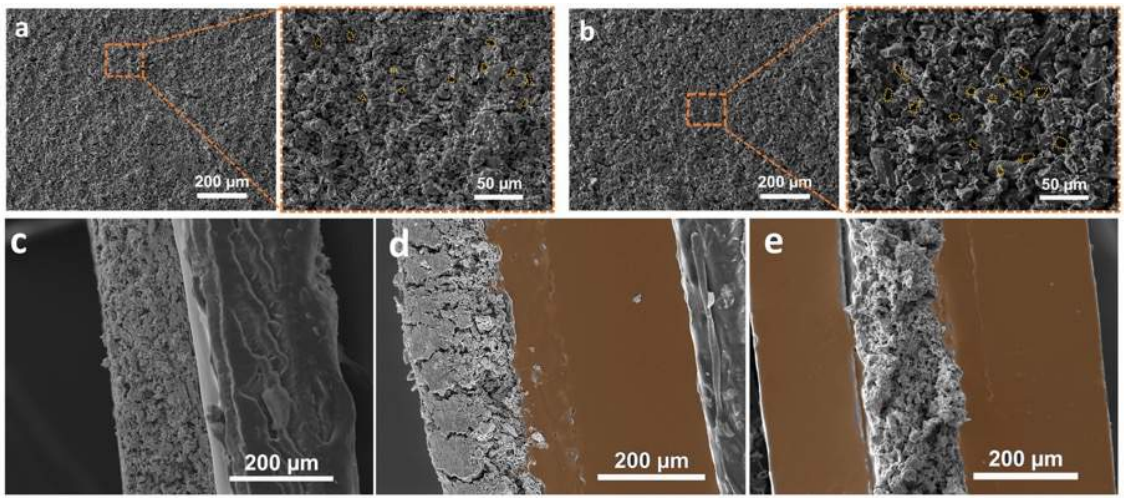

Figure 5.6 (a-b) SEM images of p-type TE materials printed on water-soluble paper and fabricated on a flexible silicone film via substrate transfer. (c-e) SEM images of cross-section of p-type TE film fabricated on a water-soluble paper; transferred to the silicone substrate; laterally sandwich-like FTEG (orange color: silicone substrate).

Continuous films of p-Bi_2Te_3/PEDOT:PSS composite were formed on the surface of both PVA paper and PDMS substrates. **Figure 5.6 (a-b)** show that the printed TE films were smooth and compact. The intricate structure of dispersion homogeneity of Bi_2Te_3 in the PEDOT:PSS matrix, enabled by 3D printing, providing a continuous network for charge transfer.

In addition, compared to the 3D printed film in **Figure 5.6a** inset, more and bigger pores were observed in the TE film after transferred to the PDMS film shown in **Figure 5.6b** inset. One possible explanation is that the H_2SO_4 treatment removed some PSS from PEDOT by the reduction of Coulomb interaction between them, thus optimized the electrical conductivity and Seebeck coefficient. Meanwhile, the thickness of TE film of the three samples was approximately 200 µm, as shown in **Figure 5.6 c-e**. The TE film was not only transferred to the PDMS substrate successfully, but also adhered to the PDMS film

tightly. After two electrodes were connected, another flexible PDMS film was conglutinated on the flexible TE film, forming the sandwich-like FTEG. For the FTEGs with aramid paper substrate (shown in **Figure 5.7**), and then annealed at 300°C for 5 minutes, nano Ag deposited silver threads were used to connect with these FTEG units in series

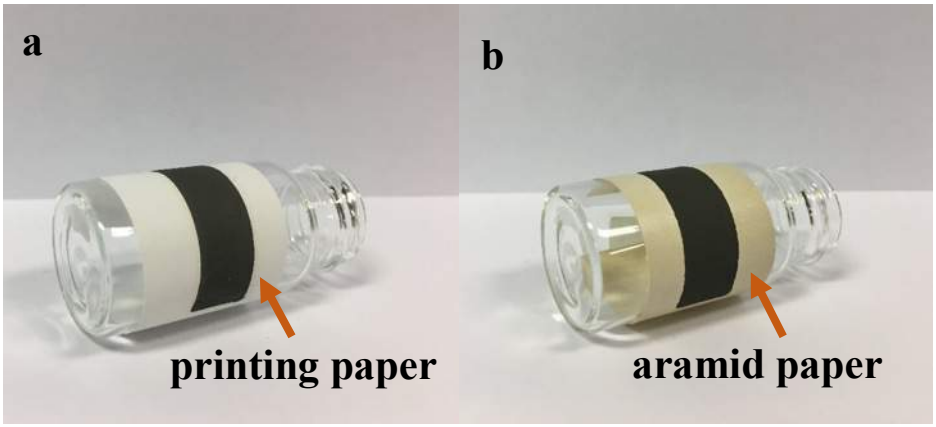

Figure 5.7 Image of 3D printed coated flexible TE film on printing paper (a) and aramid paper substrates (b).

5.3.2 Fabrication process of flexible p-n π film structure thermoelectric generators

The Fabrication process of flexible p-n π film structure FTEG was almost the same with the p-type TE film aforementioned. The printing process was carried out at room temperature and the p-type and n-type layers were printed interval on the aramid paper patterned with circuit. The printed material was dried at 323K for 12 h and then annealed at 423K for 1 h in vacuum.

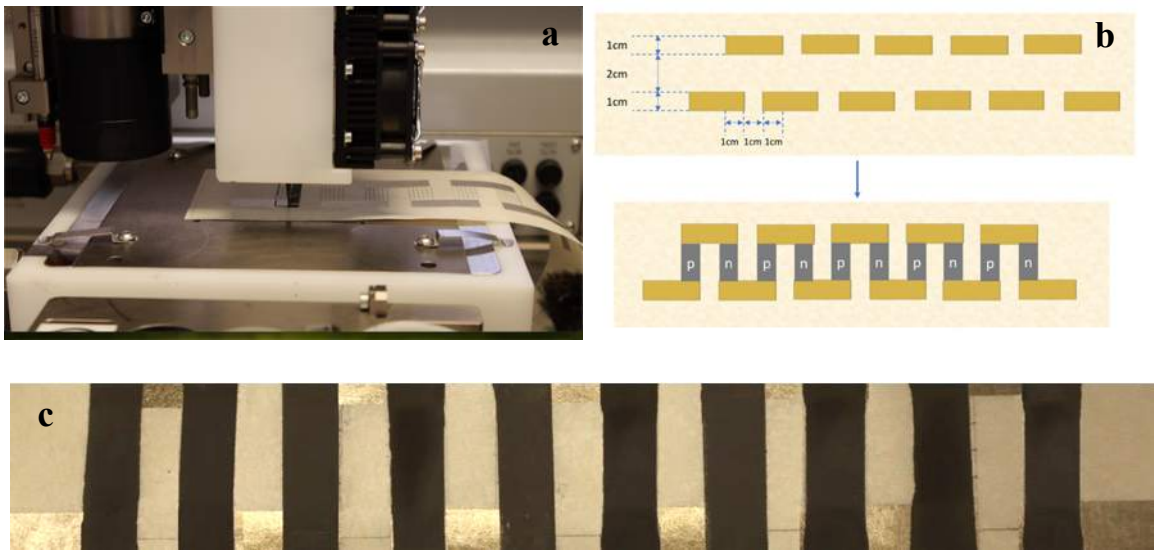

Figure 5.8 (a) Illustration of p-n film structure on aramid substrate. (b) Image of 3D printing process of TE materials on aramid paper with electrode pattern. (c) Image of completed five pairs of p-n film structure on aramid substrate.

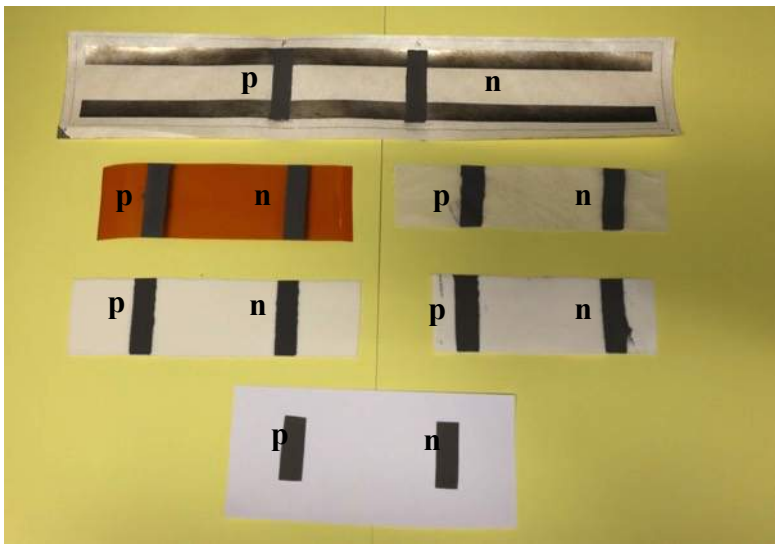

Figure 5.9 Image of bladed coated flexible TE film on varied substrates.

Blade coating is suitable for preparing large-area films but the orientations of film are not high enough as expected. In blade coating, an excess of TE material is applied to the substrate and the final amount or thickness of the coating layer is controlled by a metering

blade. This method was used to prepare the TE films with various flexible substrates shown in (**Figure 5.9**). The bladed coating thickness was about 24 □m. This method is difficult to be controlled precisely when compared with the 3D printing, nevertheless, it still has great potential for industrial production of TE films if better control is implemented.

5.3.2 Performance evaluation of film structure FTEG

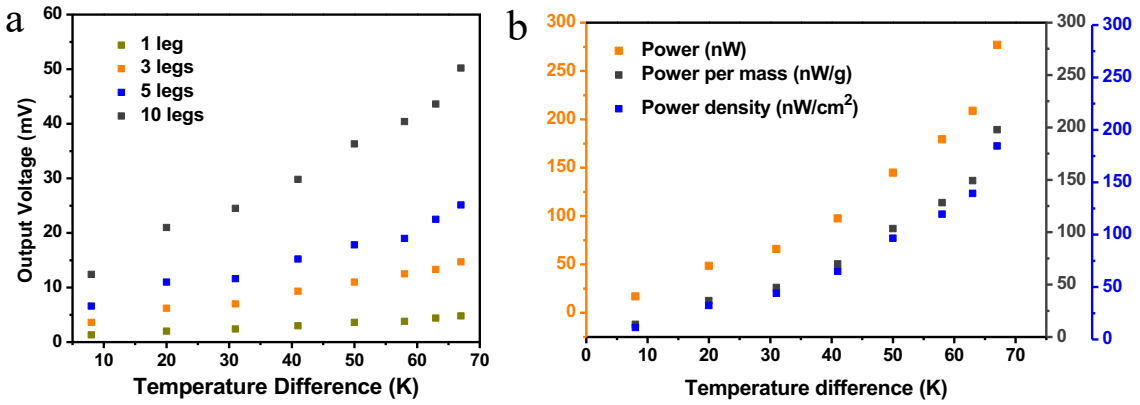

Figure 5.10 (a) Measured output voltage of 1-leg, 3-legs, 5-legs, 10-legs p-type FTEGs against temperature difference. (b) Output power (orange dots), output power per unit mass of 10-legs FTEG (red dots), and output power areal density (blue dots) of 10-legs p-type FTEG.

As shown in **Figure 5.10 a**, the measured output voltage of a single-leg p-Bi_2Te_3/ PEDOT:PSS FTEG, working from 281K to 348K, is nearly 5 mV with a temperature difference of 67 K. With 10 such units connected in series, approximately 50 mV has been achieved. **Figure 5.10 b** shows the power generated by the same device. With $\Delta T = 67$ K, the module with 10 FTEG units can generate a maximum output power of 279.6 nW. While the output power is not amenable for operating current portable or wearable micro-electronic devices such as smartphone or smartwatch, we believe that our work will orient more investigations in this field, eventually leading to the novel design and fabrication of

FTEGs. Furthermore, the FTEG is very light in term of maximum specific output power (~200 nWg^{-1}). The largest areal output power density is 184.6 nW/cm^2. The 3D printed FTEG has low weight, high flexibility, and ability to work at room to body temperature range, which are crucial for TE applications as various ubiquitous power sources.

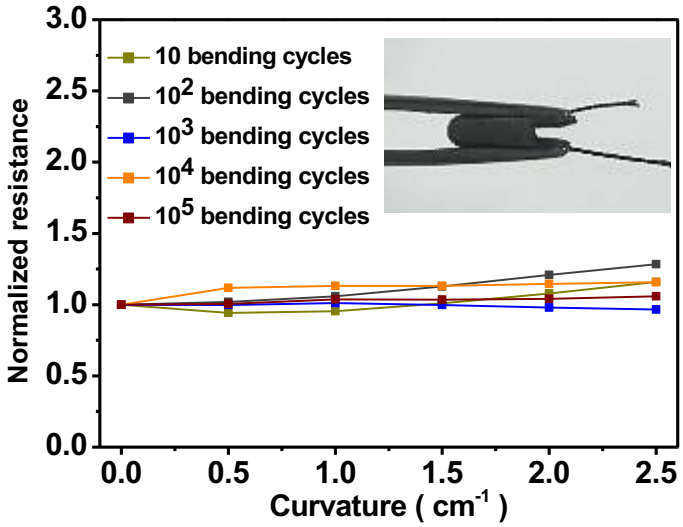

Figure 5.11 Bending test of p-Bi_2Te_3/PEDOT:PSS based FTEG.

Besides, the Bi_2Te_3/ PEDOT:PSS TEG shows great flexibility and durability in repeated bending test , as illustrated in **Figures 5.11**. The electrical resistance of the FTEG increases slightly with the bending curvature (from 0 to 2.5 cm^{-1}). The FTEG exhibits excellent fatigue resistance when it was repeatedly bent for 100,000 cycles, and its resistance recovered after released. Mechanically, the FTEG also reverted back to its original state when released. In this regard, the intricate structure of dispersion homogeneity of Bi_2Te_3 in PEDOT:PSS provides the flexible, robust and continuous networks for TE application. To our knowledge, this is the first FTEG that shows no sign of fracture when subjected to repeated large deformation of a "U" up to 100,000 times. These results declare that the FTEG can be crimped and attached on curved body for thermal collecting.

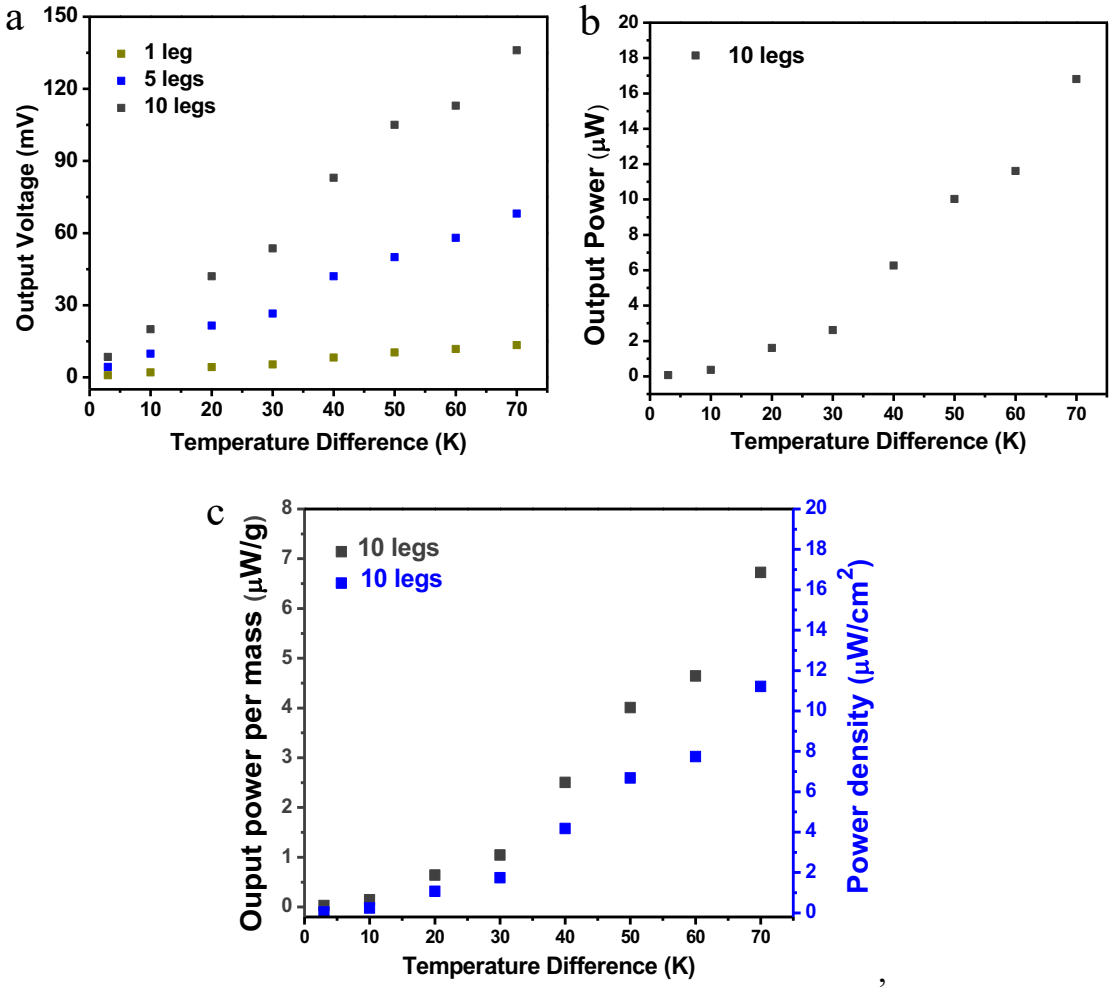

Figure 5.12 (a) Measured output voltage of 1-leg, 5-legs, 10-legs FTEGs on aramid paper circuit boards. (b) Output power, (c) output power per unit mass, output power density of 10-legs FTEGs on aramid paper circuit boards.

For the FTEG made from aramid paper and annealed at 300 ºC, the output performance was presented in **Figures 5.12 a** and **5.12 b**. The measured output voltage of a single-leg Bi_2Te_3/ PEDOT:PSS aramid paper based FTEG is nearly 13.4 mV with a temperature difference of 70 K. With 10 such units connected in series, approximately 136 mV is achieved. **Figure 5.12 c** shows the power generated by the same device. With $\Delta T = 70$ K, the aramid paper based FTEG module with these 10 TE units can generate a maximum output power of 18 μW, 64 times of that from the PDMS based FTEG under the same

conditions. Furthermore, the specific output power of the aramid paper based FTEG can be reach as high as 7 μWg^{-1}, and an areal output power density up to 11.5 $\mu W/cm^2$, approximately 62 times of PDMS-FTEG. The differences in thickness and mass per unit area of the two substrates may contribute to the apparent smaller increment (64 vs 62).

The vast differences in output power between the paper-based and PDMS-based FTEGs may lie in the annealing temperature change from 423K (PDMS-FTEG) to 573K (Aramid-paper-FTEG). The difference between the power factors of the composites annealed at these temperatures is consistent with the difference of the output power of the two FTEGs. The PDMS substrate can withstand a temperature up to 473K while the aramid paper can work at 573K for a short time. Consequently, the resultant FTEG was annealed at 423K and 573K, respectively. In our material system, the annealing temperature was limited by the thermal stability of the substrate, hence, it is expected a FTEG whose substrate can withstand a higher annealing temperature of 673K would provide even higher output power.

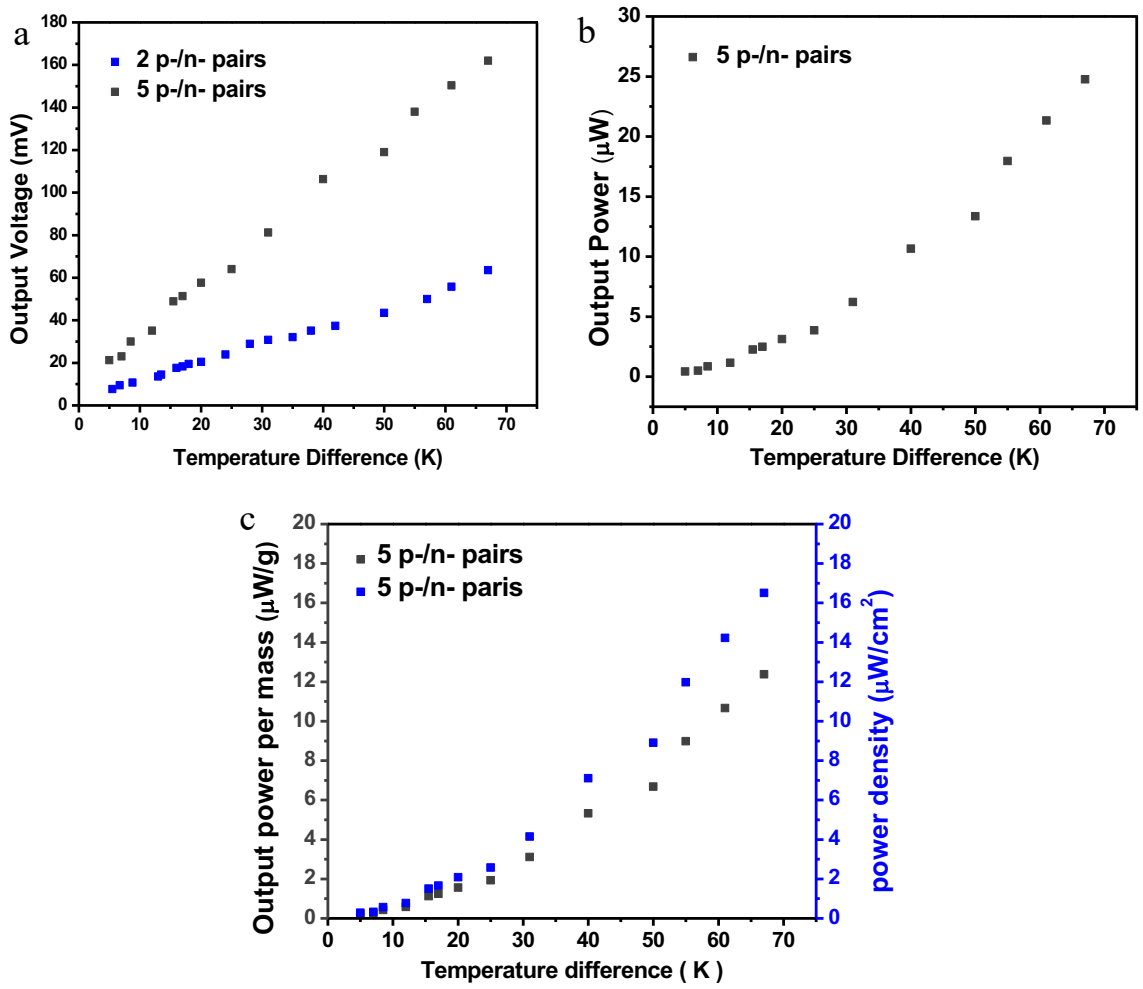

Figure 5.13 (a) Measured output voltage of 2-pairs, 5-pairs p-n π-structured FTEGs on aramid circuit boards. (b) Output power, (c) output power per unit mass, output power density of 5-pairs FTEGs on aramid paper circuit boards.

For the p-n structure FTEGs made from aramid paper as well, the output performance was presented in **Figures 5.13**. The measured output voltage of 2 pairs p-n Bi_2Te_3/ PEDOT:PSS aramid paper based FTEG is nearly 63.3 mV with a temperature difference of 67 K. With 5-pair connected in series, approximately 162 mV is achieved. The corresponding power was about 25 μW. Furthermore, the specific output power of the p-n π aramid paper based FTEG can be reach as high as 12.3 μW/g, and an areal output power density up to 16.5 $\mu W/cm^2$. The performance of p-n □ thin film shown a slightly higher than that of the pure

p-type thin film with same TE legs in it. One possible reason may be enhanced conductivity of the n-type leg, reducing the resistance of the whole film.

5.4 The sandwich-like FTEG

5.4.1 Device design

In addition to the film stricture, the same material systems can also be applied in sandwich-like device fabrication. If micro-sized TE chips can be made separately then connected to flexible substrates, the difficulties of poor TE performance and poor thermal resistance of most flexible substrates can be overcome. Thus the sandwich-like type FTEGs with chips on flexible substrate would provide opportunities for better performance. Taking advantage of the material morphological variation with annealing treatment, a novel design wearable thermoelectric device is fabricated.

Fundamentally, the TE materials must have high TE performance, that is optimal TE figure of merit with a comparatively low thermal conduction. Likewise, the thermal conduction issue in the device design should be considered as well. A novel multiple layered FTEG was designed, including 2 flexible PI films with electrodes, 2 heat-conducting glue layers and 2 copper fabrics, the TE chips were embedded between the PI films with an air gap. The connections between the TE chips and electrodes were obtained by silver paste. The TE chips had a high-ZT of 0.4 and 0.5, respectively, made from p- and n-type Bi_2Te_3/ PEDOT:PSS with optimized thermal treatments. For the TE chips, p-type material was hot pressed at 673 K, n-type chip was hot pressed at 623 K. A schematic illustration of the wearable FTEG are shown in **Figure 5.14**. In this prototype, the dimension of TE chip is 2 x 2 x 2 mm , and the air gap between p-type and n-type chips is 1 mm. Although relatively

rigid TE chips are existed in this device, the multiple-layer heat sink design ensures limited flexibility and enhances the performance by reduce thermal conductance between thermal source and the device. Compared with conventional rigid TEGs with bulky top and bottom ceramic layers, this final product is thin (~2 mm) and lightweight (0.38 g cm^{-2}), demonstrating wearable potential.

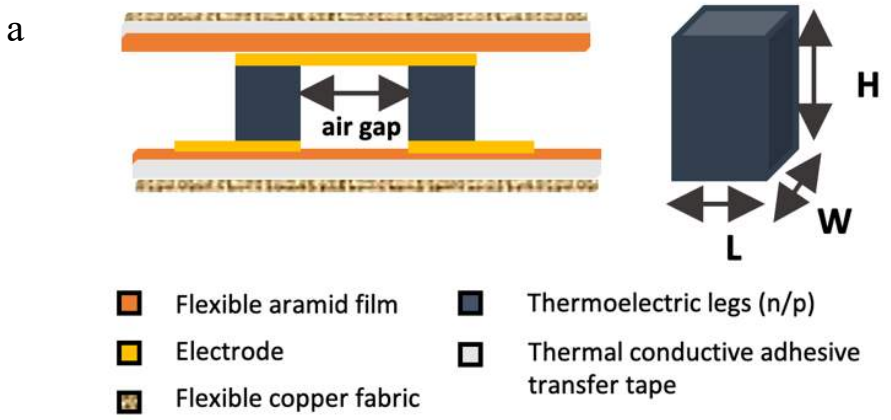

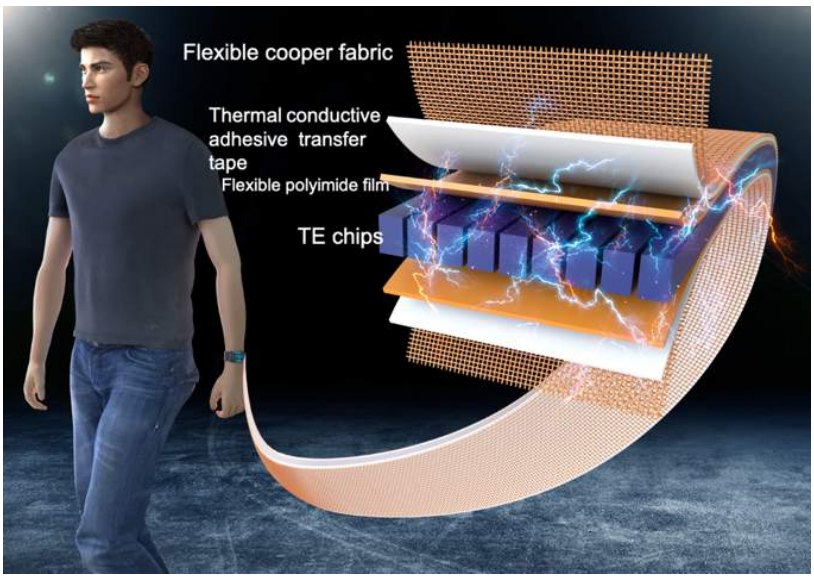

Figure 5.14 (a) The modular construction of the sandwich-like structure. (b) Schematic illustration of TED design.

The fabrication steps of the FTEG is as follows. First of all, the hot pressed p-Bi_2Te_3/PEDOT:PSS and p-Bi_2Te_3/PEDOT:PSS samples were cut into small chips with

dimensions of 2 mm by 2 mm in area and 2 mm in height. Then, the TE chips were aligned into a 4×8 array with 1-mm spacing between nearby chips. The array of π-chip pairs was attached to a flexible PI substrate with Cu electrodes using a Ag-containing epoxy adhesives followed up solidification with heating at about 573K for 10 min. The π-chip pairs were connected in series. The Cu electrodes on the PI substrate were made by etching process before for the electrode connection. After that, the thermal conductive adhesive transfer tape was attached on the PI layer and following with flexible copper fabric. Finally, a wearable TEGs with 30□35 mm^2 in area was completed. (**Figure 5.15 a-b**) This multiple-layer design not only provides sufficient flexibility despite the rigidity of TE legs but also greatly enhances the thermal conduction effect, resulting a high temperature difference.

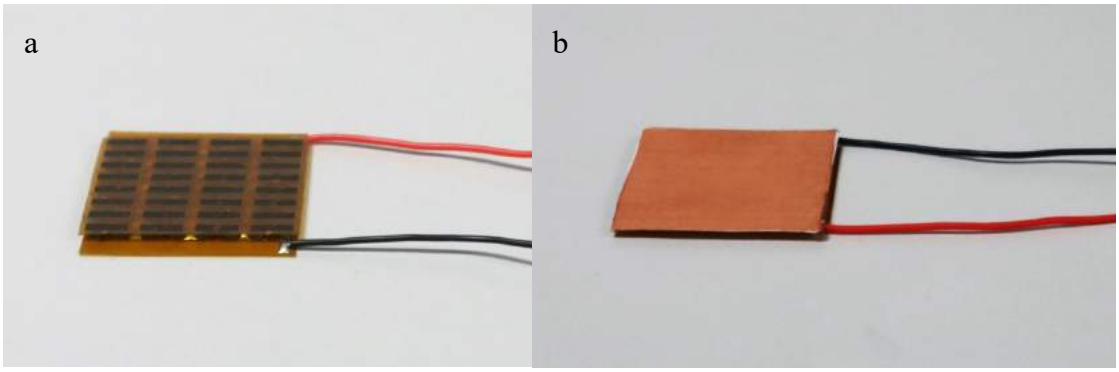

Figure 5.15 Photograph of the fabricated 20 mm by 2.5 mm flexible FTEGs with (a) PI substrate and (b) triple layer substrate.

5.4.2 Performance evaluation

For the performance evaluation, lab-made TE measurement system was used to evaluate the TE performance of the FTEGs. In the system, the volmeter and temperature detector are used for output voltage and temperature difference recording. A temperature control system including a pump and cooling water tank is used to cooling down the whole system.

Heating is achieved by electric joule heating element. A external load resistance is selected to match the internal device resistance to obtain the maximum power. The top and bottom surface of the FTEG are in direct contact with the hot/cold side of the heater in the experimental set-up. The resulted performance can be boosted by a DC-DC step-up converter, optimized for harvesting and managing energy.

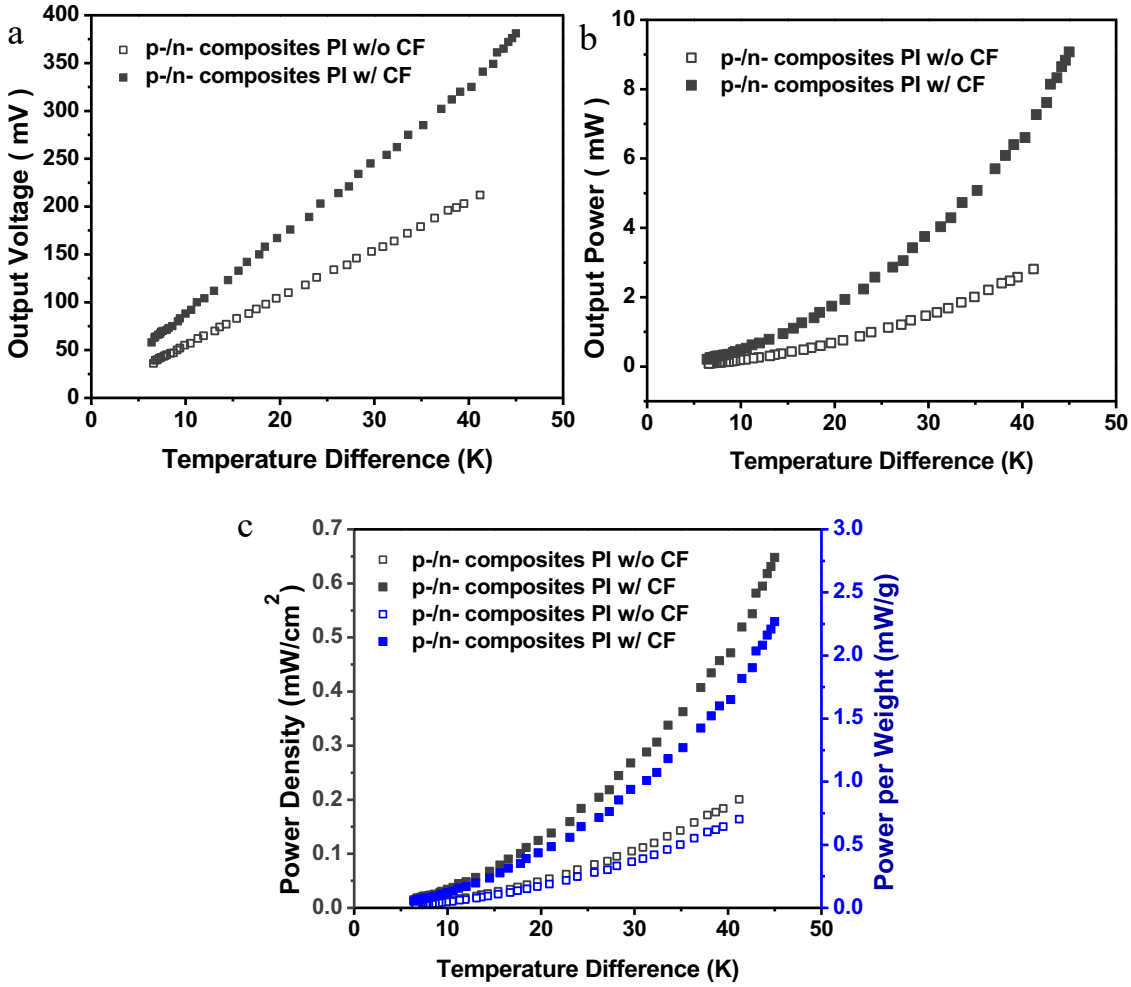

Figure 5.16 Measured (a) output voltage, (b) power, and (c) power density and power per mass of the composites FTEGs with/ without the heat-sink copper fabric.

Figure 5.16 a depicts the measured open-circuit voltage as a function of the temperature difference cross the FTEG devices with and without copper fabric heat sink. The curves are almost linear. The voltage is 381mV for the FTEG with fabric heat sink at $\Delta T = 45$ K.

It doubles that for FTEG without fabric heat sink at the same temperature difference. When the internal resistance is matching the external load, the measured output power curve of FTEG with heat sink tripled that of the FTEG without the sink fabrics . The heat sink fabric made of fine copper filaments has an outstanding flexibility and thermal conductivity. When $\Delta T = 45$ K, the 32-pair FTEG device of 3.5×4.0 cm^2, equipped with the fabric heat sink, produces an output power of 9.0 mW (**Figure 5.16 b**). The output power is comparable to that of a previously reported shape-conformable TEG using composite inks consisting of all inorganic Bi_2Te_3 inks.(*16, 17*) Furthermore, the FTEG is of lightweight and the specific output power is approximately 2.25 mW/g. The areal output power density is up to 0.64 mW/cm^2 (**Figure 5.16 c**). The output power of the realized device is one-order of magnitude lower than the theoretical upper limit thus indicating the very large space for improving the device structure and fabrication process in the future. The overall module resistance was about 4 Ω, higher than the traditional TEGs. This relatively high resistance may owing to the loose contact between the TE chips and electrodes, also the insulation microcavities in the TE chips. The copper fabric as the heat sink can reduce the thermal resistance of the heat sink and the micro-void in TE chips can enhance the thermal resistance of the inner device. This dual inner and outer thermal effect pave a practical way to enhance the temperature difference, resulting greater performance. A bending force is concentrated on the substrate when the TEG bends because the hot pressed TE materials are relatively rigid compared with printed counterparts. This design simultaneously maximizes the device flexibility and minimizes the thermal leakage through the TED, eventually resulting in high TE performance.

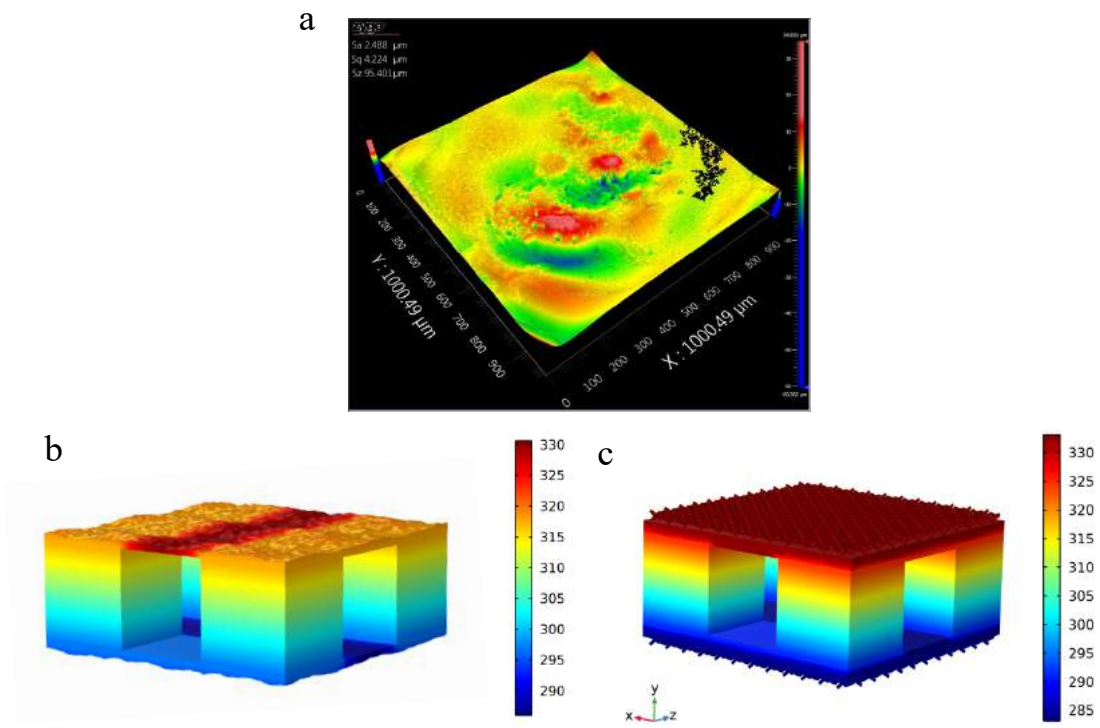

Figure 5.17 (a) Surface roughness mapping of as-made FTEG. Simulated temperature distributions of FETGs without (b)/ with (c) the heat-sink fabrics.

To deeply understand the influence of the heat sink fabric on the performance of FTEG device, analytical and numerical treatments were applied. Look a little closer to the PI film, the surface of the PI substrate is not smooth as shown in **Figure 5.17 a**. There will be air gaps between the FTEG and heat source. This effect will induce the temperature variation. **Figure 5.17 c,d** temperature distributions of FETGs without / with the heat-sink fabrics. The suimulation illustrates that the large temperature variations of FTEGs without the fabric heat sink, while with the heat sink fabric, the temperature variation on each TE leg is neglectable. The soft and conformable thermal conductive adhesive tape also fills up the airgap between the FTEG and hot or cold surface of the experimental setup. After filling up the air gap between heat/ cold source and device surface, the thermal conductance at each interface can be assumed as invariable, the average of temperature difference on TE

legs should be in the range of 37 ~ 42 K for the device with heat sink; in the range of 23 ~ 27 K for the device without heat sink. Therefore, the application of heat sink in the way of enhancing the average temperature difference on TE legs is very effective to achieve the potential of a FTEG device.

Figure 5.18 displays the comparison between FTEG devices made form pure Bi_2Te_3 alloys, composites. FTEG were made from the p- and n-type TE alloys with an identical device structure of the composite FTEG described above. The measured open-circuit voltage increases with the temperature difference monotonically (**Figure 5.18a**). Equipped with the copper heat sink fabric, the alloy FTEG exhibits a maximum output voltage of 481 mV and the corresponding output power of 30 mW at ΔT= 44 K (**Figure 5.18 a,b**). The highest areal output power density reaches up to ~ 2.0 mW/cm^2 (**Figure 5.18 c**). The overall performance of pure pure Bi_2Te_3 alloys based FTEGs is superior than that of composite based ones. These results are inconsistent with the materials properties discussed in Chapter 3 and Chapter 4. The very significant enhancement of the output power of the alloy FTEG is evident by employment of the copper fabric heat sink, similar to the FTEGs made from the composites.

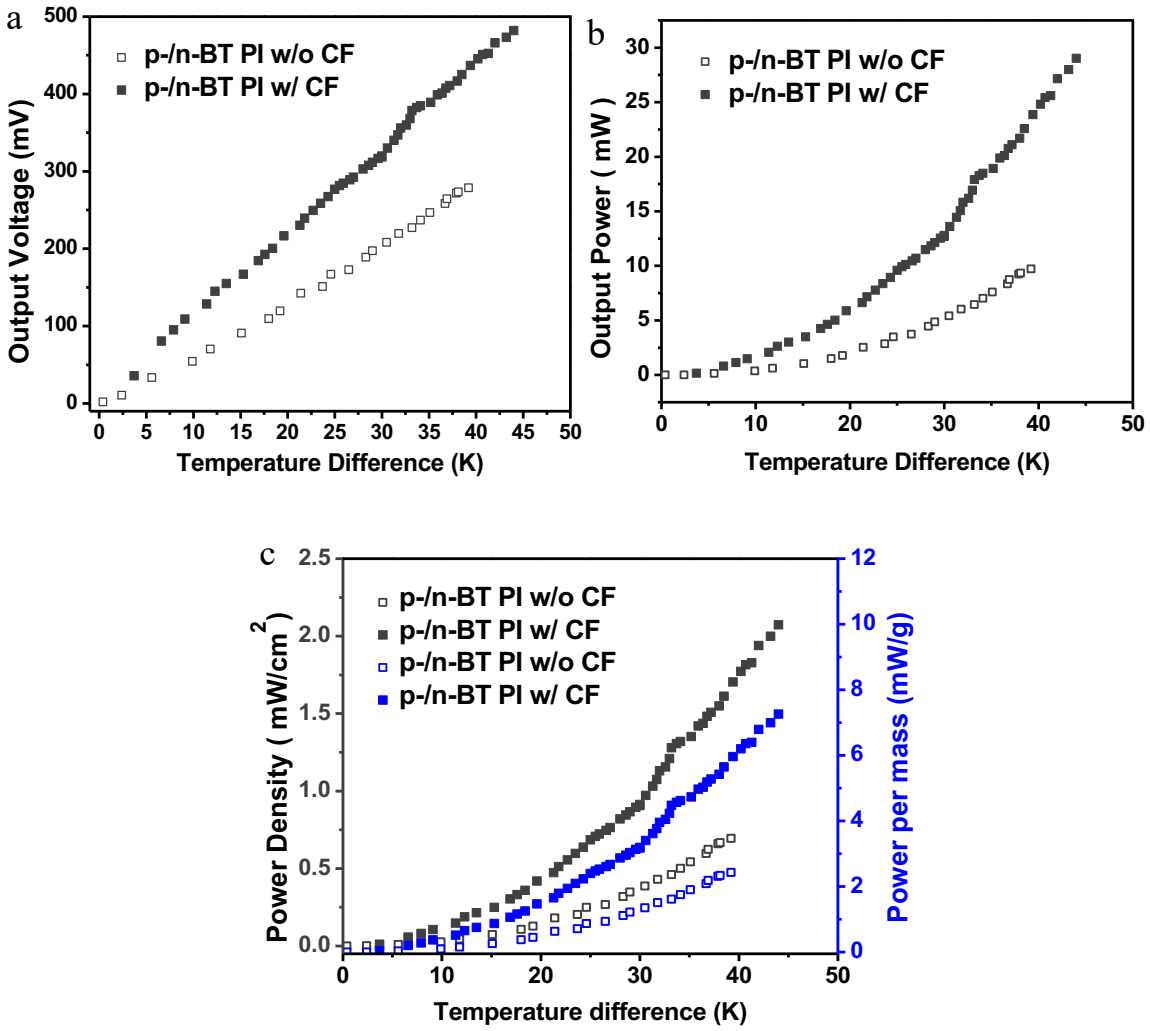

Figure 5.18 (a) Measured output voltage, (b) output power, (c) power density and power per mass of Bi_2Te_3-alloy FTEGs with/ without the heat-sing copper fabrics.

Under constant temperature difference, the measured period can keep as long as 60 min. Keeping the same thermal conditions of the experimental set-up for about 60 min, the temperature difference between the both side of the devices will reduce gradually (**Figure 5.19**). This reduction in composite FTEG is from 45 K to 34 K, smaller than that (44 K to 31 K) of the alloy FTEG. The output voltage and power reduce with time too. The copper fabric as the heat sink reduces the thermal resistance while the micro-void in composite TE chips can enhance the thermal resistance of the device. The results above show that the

performance of composites based FTEGs were in the same order of magnitudes while the composites one shown inferior with the pure Bi_2Te_3 ones. These results coincide with materials performance.

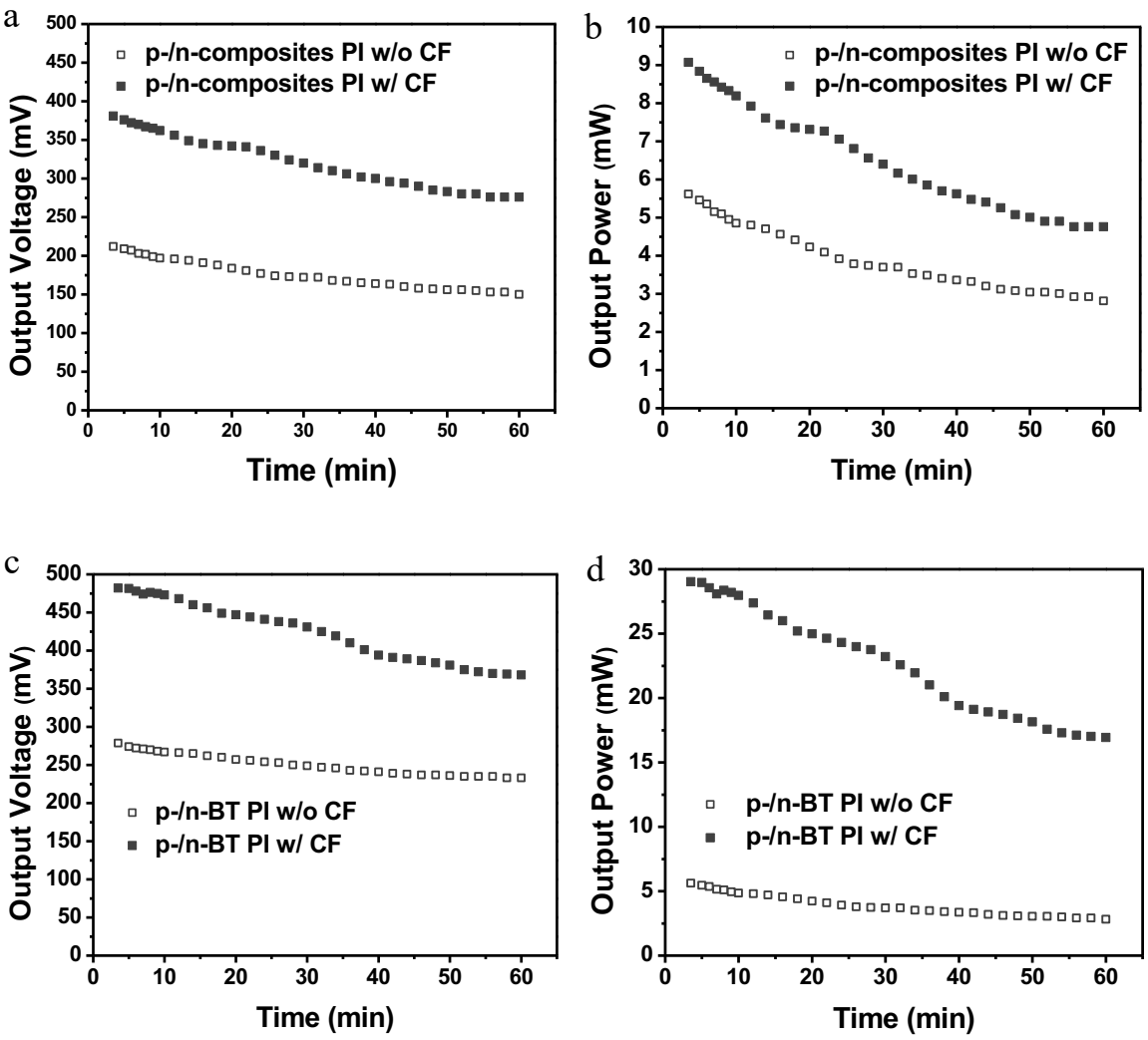

Figure 5.19 (a, b) Measured output voltage and power of composite FTEGs plotted against time. (c, d) Output voltage and power of Bi_2Te_3-alloy FTEGs plotted against time.

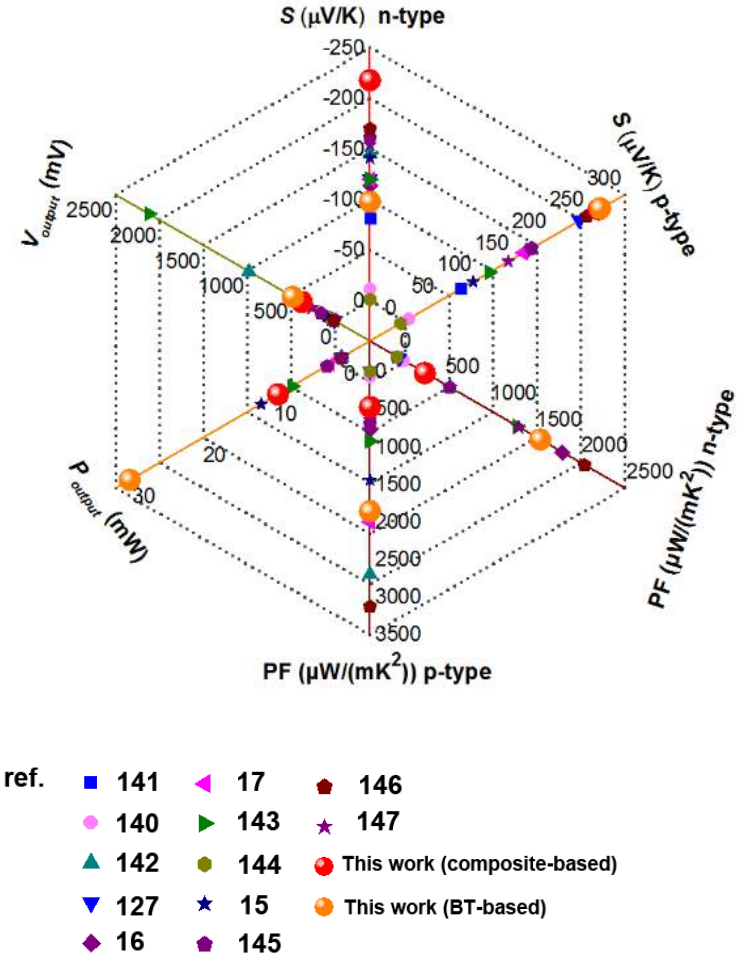

Figure 5.20 Performance benchmark of this work against other Bi_xTe_y-based FTEGs reported in the literatures.(*16, 127, 140-142*) (*15, 17, 143-147*)

Here, we further compared the major TE properties of our TE composites and the output power of FTEGs made from the TE composites, pure p-/n- Bi_2Te_3 alloys and other Bi_xTe_y-based FTEGs reported previously in the literature, as illustrated by **Figure 5.20**. It is very encouraging that the present n-type TE composite has the highest near-room-temperature Seebeck coefficient, superior to all other n-type Bi_xTe_y alloys and their TE composites. The present p-type TE composite also exhibit a high Seebeck coefficient, slightly higher than its constitutive alloy and much higher than other reported works. Due to the low electrical conductivity of the composites, the power factors for the n- and p-type composites have

much space to improve, as compared with their constituent alloys. The output power of the composite FETG is better or comparable to most reported previously, (*15-17, 127, 141-143*) (*140, 144-147*) although it is still much reduced from that of the alloy FTEG. The optimization of device structure and reduction of contact resistance can further improve the output power of the composite FTEGs.

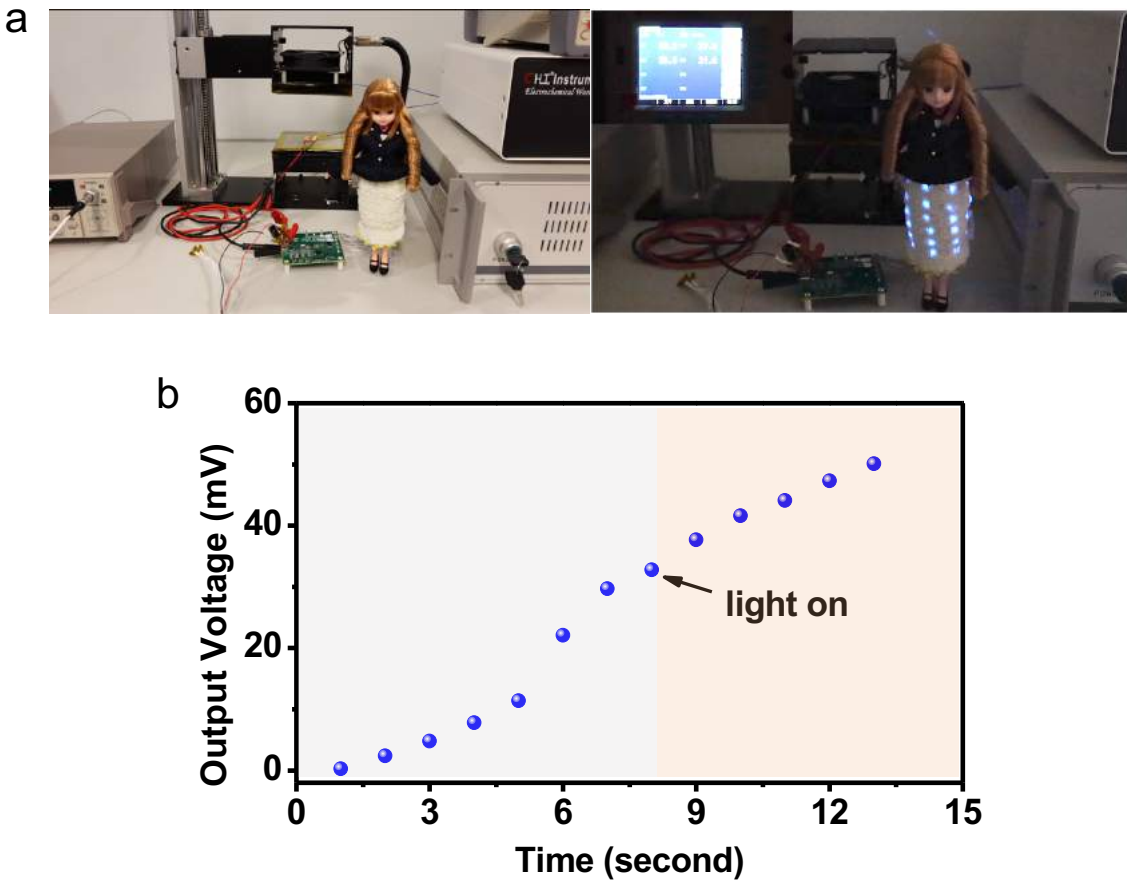

Figure 5.21 (a) An FTEG drives an LED fabric skirt via demo board. (b) Time-resolved output voltage of FTEG when light on the LEDs.

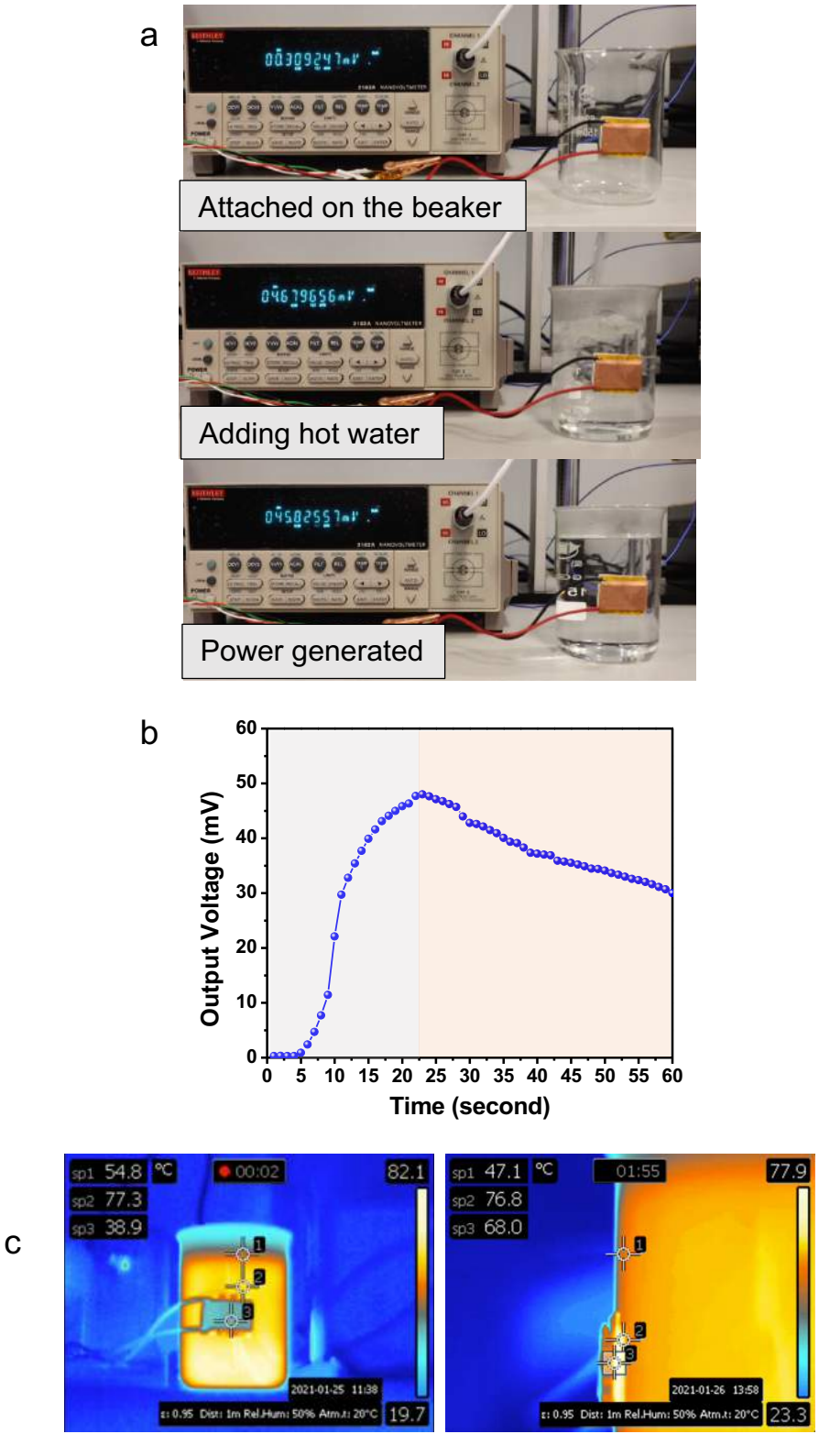

Figure 5.22 (a,b) Demonstration and output voltage of an FTEG attached on the curved surface of a beaker containing hot water. (c) Heat transfer distribution of an FTEG attached on the beaker containing hot water.

Using polyimide thin-film substrate, sandwich-structured FTEG devices exhibit a low bending rigidity thus can be deformed to some extent. **Figure 5.21** illustrates that an as-made FTEG is bent and attached on the curved surface of a beaker containing hot water and generates an output voltage of 45 mV. Significantly, owing to the outer flexible heat sink and inner low thermal conducting TE chips, the device can still keep the temperature difference for powering for a while after adding the hot water. Compared with the reported device without heatsink design, the output curve of this device goes relatively gentle instead of sharp reduction. Thus, in this system, the thermal-electric conversion shows more efficiency and long-term.(*143*) Such an FTEG can also drive an LED fabric in seconds when being placed between the hot and cold sides on the lab-made experimental set-up (**Figure 5.22**).

5.5 Devices Comparison

Comparison	**Film structure**	**Sandwich-like structure**	**Rigid TEG**
Flexibility	✓✓	✓	
Energy saving during fabrication process	✓		
Output Performance		✓	✓✓
Wearability		✓	
Lightweight	✓✓	✓	

Since the geometry of first type and second type FTEGs is different, the quantity of n-p pairs is also varied, it is hard to compare the merit and demerit of these two different FTEGs without any consideration or simulation. However, it is reasonable to discuss the differentia of these two FTEGs from perspective of fabrication process, flexibility and specific power. For the first type FTEGs, the comparatively low temperature or energy is needed in device fabrication, about 423K or 573K in a short time. However, both elastic substrate and thin film material provide more reliable guarantee for the flexibility which would be well-suited to the anomalous heat/cold source. Also, the relative high length-width ratio can hold the large working temperature difference in real application. The thin-film-structured FTEGs have two or three orders of magnitude lower specific or areal power density than the sandwich-structured FTEGs made of composite or alloy in general. The electrical conductivity and Seebeck coefficients of the printed p-and n-composite films are much lower those materials. The lack of densification process and lower annealing temperature of the printed FTEGs contribute to the impaired compactness of TE composite and its TE performance. However, one remains optimistic that the current poor performance of the film-structured FTEGs may be improved by a high annealing temperature, a better densification process together with reduction of contact resistance and device structure. Hence a high specific power density can be achieved, at least in principle, similar to or ever better than that for the sandwich-structured FTEGs. Both inherent flexibility of the TE composite and flexible substrates used in the thin-film-structured FTEGs provide more possibilities for the atypical heat source collection. While the output power is not commendable for operating current portable or wearable micro-electronic devices, this work illustrates the current limitations, sets up the theoretical ideal output, and charts up a roadmap for achieving the theoretical upper output limits. We believe that this work will

stimulate other investigations, eventually leading to the successful applications of FTEGs as an alternative power source for wearable microelectronic devices.

For the second type FTEGs, usually high temperature post treatments is required during fabrication process. Also, a high temperature tolerant substrate is necessary for the flexible and wearable TE applications if the integration of TE materials and electrodes are implemented before the thermal treatment. The potential substrate choose is limited. For the wearable application, flexing force is concentrated on the substrate when the FTEG winds because the hot pressed TE materials are relatively rigid compared with printed counterparts. In terms of working temperature, this kind of FTEGs cannot keep the large temperature difference owing to the comparatively low length-width ratio. When considering the performance, the specific power of second type FTEG shows one order of magnitude higher than that of first type FTEGs. In addition, in second type FTEGs, the effects of a copper fabric heat sink on the output performance of a wearable FTEG is also investigated. The high performance of the FTEG with copper fabric can be attributed to the improved thermal design: the copper fabric as the heat sink can reduce the thermal resistance of the heat sink and the micro-void in TE chips can enhance the thermal resistance of the inner device. This dual inner and outer thermal effect pave a practical way to enhance the temperature difference, resulting greater performance.

5.6 Conclusion

In this chapter, a three-dimensional printed FTEG device has been developed by using a novel high performance p-/n-Bi_2Te_3/PEDOT:PSS TE composite ink paste. Besides, the materials and preparation procedure for the ink, as well as the structural design, mechanism,

and fabrication procedure of the pliable two type of FTEG device are presented. More importantly, first type FTEGs were fabricated by three-dimensionally 3D printing on aramid paper and PDMS substrates, respectively. The first paper-based thermoelectric generator could produce a higher output power of 30.8 μW, the specific power density of 12.3 $\mu W g^{-1}$ and areal power density of 20.5 $\mu W/cm^2$ working at under 70 K temperature difference. In addition, the variation in electric resistance of the PDMS-based flexible TEG is negligible even after 100,000 bending cycles up to 2.5 cm^{-1} curvature, demonstrating high flexibility and durability in cyclic bending tests. The method to make FTEGs by printing TE composite precursor paste ink onto flexible substrates is a solution-based room-temperature operation. The additive method is most suitable for three-dimensionally printing, disperse printing or screen printing processes. The solidification by drying and annealing operations of the paste ink is done at low or moderate temperatures so that a variety of fibrous materials can be used for FTEGs. For the second type FTEGs, the performance can be enhanced with optimal design. For the FTEG with copper fabric, the overall performance demonstrate higher than the one without copper fabric. With $\Delta T \approx 36$ K, the module with cooper fabric can generate a maximum output power of 1140 mW. Furthermore, the FTEG is also lightweight and the maximum specific output power is approximately 300 $mW g^{-1}$. The largest areal output power density can improve up to 456 $mW cm^{-2}$. These composites, fabrication methods and findings pave a way to produce high-performance FTEGs for wearable electronic systems, waste heat harvesting and active microclimate control systems.

Chapter 6 CONLUSIONS AND RECOMMENDATIONS FOR FUTURE WORK

6.1 Conclusions

This thesis presents a systematic study about p-/n-Bi_2Te_3/PEDOT:PSS based FTEGs. Firstly, different annealing temperature affected on the p-/n-Bi_2Te_3/PEDOT:PSS TE composites were prepared and the TE properties of these samples were investigated. The possible impact factors and mechanism on p-/n-Bi_2Te_3/PEDOT:PSS composites were proposed and analysed. Then, the application of these composites on FTEGs were explored. Finally, two types of Bi_2Te_3/PEDOT:PSS based FTEGs were fabricated successfully, and the corresponding output performance of these two FTEGs were evaluated via lab-made measurement systems. Generally, the major conclusions are summarized as follows:

(1) New ink pastes suitable for disperse printing are synthesized, and their resultant composite comprising p-/n-Bi_2Te_3/PEDOT:PSS exhibits superior Seebeck coefficient, power factor and figure of merit among Bi_xTe_y/PEDOT:PSS composites reported so far. The superior room-temperature performance of p-/n-Bi_2Te_3/PEDOT:PSS thermoelectric composites explored in this work are suitable for printed flexible thermoelectric generators. The Seebeck coefficient of the optimized p-/n-Bi_2Te_3/PEDOT:PSS thermoelectric composite are 273.3 μV/K and -218.0 μV/K at room temperature, reaching that of pure Bi_2Te_3, representing the highest value for Bi_xTe_y/PEDOT:PSS composites reported so far. The corresponding power factor and ZT are 473.5 $\mu W/m \cdot K^2$, 306$\mu W/m \cdot K^2$ and 0.4, 0.23, respectively.

(2) A solution-based, moderate-temperature fabrication process of FTEG devices is firstly described. A single layer p-Bi_2Te_3/PEDOT:PSS TE composite film was printed on various substrates providing a mechanically soft and robust support that ensures an assortment of applications in complex environment. The intricate microstructure, enabled by 3D multi-material printing, becomes a well-organized and flexible precursor for FTEG.

(3) Moderate-temperature annealing is applicable to fabricate first type FTEGs. The paper-based FTEG possesses a high output power, specific and areal power density as well as excellent flexibility. FTEGs were fabricated by disperse printing on aramid paper and PDMS substrate, respectively. With $\Delta T = 70$ K, the paper-based thermoelectric generator demonstrates a high output power of 30.8 μW, specific power density of 12.3 μW/g and areal power density of 20.5 $\mu W/cm^2$.

(4) High flexibility and durability have been displayed in cyclic bending tests of PDMS-based thermoelectric generators. The variation in electric resistance is negligible even after 100,000 bending cycles up to 2.5 cm^{-1} curvature. The solution-processible, soft and flexible composites offer unique advantages that are not available to their rigid counterparts. The methods and findings presented in this report pave a way to produce high-performance flexible thermoelectric generators for wearable electronic systems, waste heat harvesting and active microclimate control systems.

(3) High-temperature treatment is applicable to fabricate second type FTEGs. The sandwich-like FTEG possesses the higher output power, specific and areal power density than that of first type FTEGs. For the FTEG with copper fabric, the overall performance demonstrate higher than the one without copper fabric. The resultant sandwich-structured FTEG shows an output power of 9.0 mW, specific output power of 2.3 mW/g and areal

power density of 0.65 mW/cm^2 at ΔT= 45 K, illustrating its promising application in wearable microelectronic devices requiring a driving power of several mWs. The marked improvement of output power of FTEG with heat-sink fabrics are revealed. The effects of annealing temperature and densification brought by the fabrication processes are highlighted. Discussions on the further improvements for the FTEGs are offered in light of the derived theoretical upper limit of the output power. This work will stimulate more research interests in pursuing high-performance FTEGs and their applications in wearable electronics, IoT, low-heat waste thermal energy harvesting.

6.2 Recommendations for Future work

The above findings demonstrated progress towards inorganic-organic TE materials for FTEGs technology. Still, owing to the insufficient time and resources, the research remains deficiencies and it also needs further work. The following suggestions are of significant scientific and practical relevant for future study.

(1) More systematic characterizations of the Bi_2Te_3/PEDOT:PSS inorganic-organic composites is needed to know the mechanism well. To our best knowledge, although significance progresses have been made toward increasing PF of inorganic-organic TE composites, the mechanisms on the interaction between inorganic and organic composites are unclear so far. One possible approach is to study more deeply on the morphology of the polymer constituent in the composites since the macromolecular conjugated systems are very complex in morphology and their structure is typically associated with randomly coiled chains of atoms, and also have contributions in density and free volume.

(2) The electrical conductivity of the TE composite need to improve. In this study, the electrical conductivity of all different temperature annealing Bi_2Te_3/PEDOT:PSS composite samples showed lower than that of the pure Bi_2Te_3 samples because of the inferior performance of the PEDOT:PSS. As shown from both the so-called Mott-Schottky and Wiedermann-Franz equation, those five parameters about TE properties are not individually, and they have a relationship of interaction instead. it can be seen from these equation that S and σ are anticorrelated. This fundamental relationship determined the huge challenges to improve the ZT of the TE materials. One solution might have been to rational engineering of the inorganic-organic interfaces, including morphology and energy alignment, which can allow improvement in PF by substantially enhancing S without greatly suppressing σ.

(3) The structure of the FTEGs are not the optimal ones for the highest efficiency. The relationship between dimension of TE legs and efficiency of FTEGs could be further studied and optimized to improve the power output. One of the effective strategy is to simulate TEGs by varying the geometry of the legs to find the optimum geometry of the TE legs. As shown from above description in chapter 2, thermal resistance and electronic connectors also play an important role in device performance. In the following study, the issues of thermal resistance and electronic connectors are also required considerations.

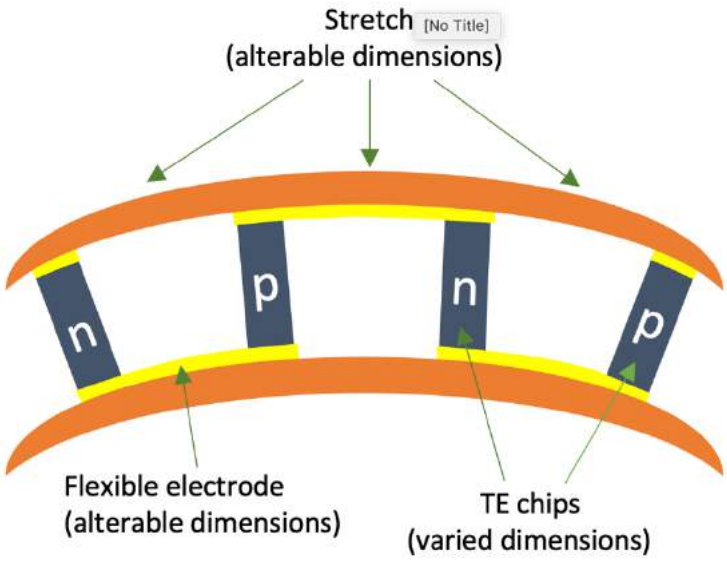

Figure 6.1Schematic diagram of the flexibility of the FTEG.

(4) The performance of the FTEGs are still lower than that of traditional rigid TEGs. From the results in Chapter 5, the thermoelectric performance (ZT) of the composite system were poorer than the equivalent TE particles. In this flexible system, the polymer acted as the bridge to connect the TE particles together and increased the flexibility of the composite as well, while it is difficult to ensure the performance equal to the pure inorganic materials. One possible solution is to adjust the performance of the TE-composite system for the FTEGs.

(5) Bi_2Te_3 is the semiconductor materials with the best thermoelectric properties near room temperature. In this task, the TE fibers will be fabricated. The adopted methods include RF sputtering, vapor deposition, and annealing process. The designed TE fibre has four layers from the inside to outside, including fibre substrate, n-/p- TE materials or electrode, protect layer, cooling layer (Figure 1). Polyimide (PI) fibre is selected as the substrate owing to high temperature resistant and flame-retardant. The long-term service temperature of PI fibre is 260℃ which is suitable for the room temperature ranged TE function. P-/n-type

Bi_2Te_3 materials will be sputtered on the fibre alternately as first layer for the TE function. Then, copper will be deposited between the p-/n-segment for the connection. The parylene will be deposited on the second layer as the protective barrier when attach to the human skin. The parylene coating can penetrate crevices and tight areas on multi-layer components, providing complete and uniform encapsulation. Finally, the fourth layer of cooper will be coated as the cooling layer to increase working temperature difference. For the final product, these prepared TE fibers will be woven into the textile devices for the wearable self-powering application (Figure 6.2).

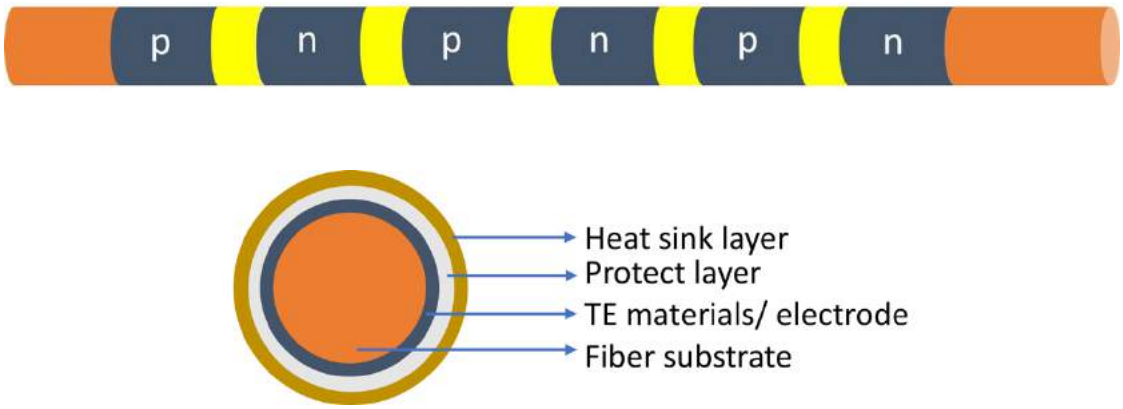

Figure 6.2 Schematic diagram of flexible TE fibers.

The challenge here is to develop uniform multilayers of TE materials, protective layer, and cooling layer in fibrous structures to achieve high performance. Based on the structure assumption, the effects of several factors will be considered, such as the thickness and length of TE materials, protective layer, cooling layer, as well as the structure of fiber. Among them, when considering the most important core TE properties, the fabrication parameters and annealing treatments will affect the TE performance of the n-/p-type Bi_2Te_3 layers. The morphology structure and related performance of n-/p-type Bi_2Te_3 layers cannot be separated from the preparation technology and process. In this task, RF magnetron

sputtering is used to deposit n-/p-type Bi_2Te_3 layers, copper layers on fiber substrate. The effects of target sputtering power, working pressure, annealing temperature will be explored. At the same time, XRD, SEM, EDS and other analytical methods will be used to characterize the prepared TE thin films, and their electrical properties will be tested for the following device fabrication.

References

1. C. Forman, I. K. Muritala, R. Pardemann, B. Meyer, Estimating the global waste heat potential. *Renew Sust Energ Rev* **57**, 1568-1579 (2016).
2. R. Saidur, M. Rezaei, W. K. Muzammil, M. H. Hassan, S. Paria, M. Hasanuzzaman, Technologies to recover exhaust heat from internal combustion engines. *Renew Sust Energ Rev* **16**, 5649-5659 (2012).
3. M. D. White, C. M. Bosio, B. N. Duplantis, F. E. Nano, Human body temperature and new approaches to constructing temperature-sensitive bacterial vaccines. *Cell Mol Life Sci* **68**, 3019-3031 (2011).
4. T. T. M. H. T. Togawa, *Body Temperature, Heat Flow, and Evaporation* (2017).
5. M. Tian, Z. L. Wang, J. Li, 3D numerical simulation of heat transfer through simplified protective clothing during fire exposure by CFD. *Int J Heat Mass Tran* **93**, 314-321 (2016).
6. X. L. Su, F. Fu, Y. G. Yan, G. Zheng, T. Liang, Q. Zhang, X. Cheng, D. W. Yang, H. Chi, X. F. Tang, Q. J. Zhang, C. Uher, Self-propagating high-temperature synthesis for compound thermoelectrics and new criterion for combustion processing. *Nat Commun* **5**, (2014).
7. Q. P. Wan, Y. K. Teh, Y. Gao, P. K. T. Mok, Analysis and Design of a Thermoelectric Energy Harvesting System With Reconfigurable Array of Thermoelectric Generators for IoT Applications. *Ieee T Circuits-I* **64**, 2346-2358 (2017).
8. Q. P. Wan, P. K. T. Mok, A 14-nA, Highly Efficient Triple-Output Thermoelectric Energy Harvesting System Based on a Reconfigurable TEG Array. *Ieee J Solid-St Circ* **54**, 1720-1732 (2019).

9. S. P. Lin, W. Zeng, L. S. Zhang, X. M. Tao, Flexible film-based thermoelectric generators. *Mrs Adv* **4**, 1691-1697 (2019).

10. W. Zeng, X. M. Tao, S. P. Lin, C. Lee, D. L. Shi, K. H. Lam, B. L. Huang, Q. M. Wang, Y. Zhao, Defect-engineered reduced graphene oxide sheets with high electric conductivity and controlled thermal conductivity for soft and flexible wearable thermoelectric generators. *Nano Energy* **54**, 163-174 (2018).

11. L. S. Zhang, S. P. Lin, T. Hua, B. L. Huang, S. R. Liu, X. M. Tao, Fiber-Based Thermoelectric Generators: Materials, Device Structures, Fabrication, Characterization, and Applications. *Adv Energy Mater* **8**, (2018).

12. X. M. Tao, Study of Fiber-Based Wearable Energy Systems. *Accounts Chem Res* **52**, 307-315 (2019).

13. V. Karthikeyan, J. U. Surjadi, J. C. K. Wong, V. Kannan, K. H. Lam, X. F. Chen, Y. Lu, V. A. L. Roy, Wearable and flexible thin film thermoelectric module for multi-scale energy harvesting. *J Power Sources* **455**, (2020).

14. M. R. Burton, T. J. Liu, J. McGettrick, S. Mehraban, J. Baker, A. Pockett, T. Watson, O. Fenwick, M. J. Carnie, Thin Film Tin Selenide (SnSe) Thermoelectric Generators Exhibiting Ultralow Thermal Conductivity. *Adv Mater* **30**, (2018).

15. S. J. Kim, J. H. We, B. J. Cho, A wearable thermoelectric generator fabricated on a glass fabric. *Energ Environ Sci* **7**, 1959-1965 (2014).

16. S. H. Park, S. Jo, B. Kwon, F. Kim, H. W. Ban, J. E. Lee, D. H. Gu, S. H. Lee, Y. Hwang, J. S. Kim, D. B. Hyun, S. Lee, K. J. Choi, W. Jo, J. S. Son, High-performance shape-engineerable thermoelectric painting. *Nat Commun* **7**, (2016).

17. F. Kim, B. Kwon, Y. Eom, J. E. Lee, S. Park, S. Jo, S. H. Park, B. S. Kim, H. J. Im, M. H.

Lee, T. S. Min, K. T. Kim, H. G. Chae, W. P. King, J. S. Son, 3D printing of shape-conformable thermoelectric materials using all-inorganic Bi2Te3-based inks. *Nat Energy* **3**, 301-309 (2018).

18. M. H. Elsheikh, D. A. Shnawah, M. F. M. Sabri, S. B. M. Said, M. H. Hassan, M. B. A. Bashir, M. Mohamad, A review on thermoelectric renewable energy: Principle parameters that affect their performance. *Renew Sust Energ Rev* **30**, 337-355 (2014).

19. X. Shi, L. Chen, C. Uher, Recent advances in high-performance bulk thermoelectric materials. *Int Mater Rev* **61**, 379-415 (2016).

20. N. M. Yatim, N. Z. I. M. Sallehin, S. Suhaimi, M. A. Hashim, A Review of ZT Measurement for Bulk Thermoelectric Material. *Aip Conf Proc* **1972**, (2018).

21. H. E. Katz, T. O. Poehler, *Innovative thermoelectric materials : polymer, nanostructure and composite thermoelectrics* (Imperial College Press Distributed by World Scientific Publishing Co. Pte Ltd., London Hackensack, NJ, 2016), pp. xv, 276 pages.

22. W. He, G. Zhang, X. X. Zhang, J. Ji, G. Q. Li, X. D. Zhao, Recent development and application of thermoelectric generator and cooler. *Appl Energ* **143**, 1-25 (2015).

23. A. Montecucco, A. R. Knox, Maximum Power Point Tracking Converter Based on the Open-Circuit Voltage Method for Thermoelectric Generators. *Ieee T Power Electr* **30**, 828-839 (2015).

24. A. Shakouri, Recent Developments in Semiconductor Thermoelectric Physics and Materials. *Annu Rev Mater Res* **41**, 399-431 (2011).

25. Q. Kuai, Q. P. Wan, P. K. T. Mok, An Auto-polarity Thermoelectric Energy Harvesting

Interface Based on a Boost/Buck-Boost Converter. *Ieee Int Symp Circ S*, (2019).

26. Q. Kuai, Q. P. Wan, P. K. T. Mok, A Dual-Frequency Dual-Input-Dual-Output Interface for Thermoelectric Energy Harvesting and Recycling With 82.9% Efficiency. *Proc Eur Solid-State*, 137-+ (2019).

27. T. M. Tritt, M. A. Subramanian, Thermoelectric materials, phenomena, and applications: A bird's eye view. *Mrs Bull* **31**, 188-194 (2006).

28. W. B. Zhou, Q. X. Fan, Q. Zhang, L. Cai, K. W. Li, X. G. Gu, F. Yang, N. Zhang, Y. C. Wang, H. P. Liu, W. Y. Zhou, S. S. Xie, High-performance and compact-designed flexible thermoelectric modules enabled by a reticulate carbon nanotube architecture. *Nat Commun* **8**, (2017).

29. R. Zybala, M. Schmidt, P. Kaminska, M. J. Kruszewski, J. Grzonka, K. Pietrzak, L. Ciupinski, Skutterudite (CoSb3) thermoelectric nanomaterials fabricated by Pulse Plasma in Liquid. *Mater Today-Proc* **5**, 10316-10322 (2018).

30. Y. C. Lan, A. J. Minnich, G. Chen, Z. F. Ren, Enhancement of Thermoelectric Figure-of-Merit by a Bulk Nanostructuring Approach. *Adv Funct Mater* **20**, 357-376 (2010).

31. J. Q. Guo, H. Y. Geng, T. Ochi, S. Suzuki, M. Kikuchi, Y. Yamaguchi, S. Ito, Development of Skutterudite Thermoelectric Materials and Modules. *J Electron Mater* **41**, 1036-1042 (2012).

32. A. Moure, M. Rull-Bravo, B. Abad, A. Del Campo, M. M. Rojo, M. H. Aguirre, A. Jacquot, J. F. Fernandez, M. Martin-Gonzalez, Thermoelectric Skutterudite/oxide nanocomposites: Effective decoupling of electrical and thermal conductivity by functional interfaces. *Nano Energy* **31**, 393-402 (2017).

33. A. A. Ivanov, A. I. Sorokin, V. P. Panchenko, I. V. Tarasova, N. Y. Tabachkova, V. T.

Bublik, R. H. Akchurin, Structure of the Cu2Se compound produced by different methods. *Semiconductors+* **51**, 866-869 (2017).

34. S. Ballikaya, H. Chi, J. R. Salvador, C. Uher, Thermoelectric properties of Ag-doped Cu2Se and Cu2Te. *J Mater Chem A* **1**, 12478-12484 (2013).

35. S. Butt, W. Xu, M. U. Farooq, G. K. Ren, Q. H. Zhang, Y. C. Zhu, S. U. Khan, L. J. Liu, M. J. Yu, F. Mohmed, Y. H. Lin, C. W. Nan, Enhanced Thermoelectricity in High-Temperature beta-Phase Copper(I) Selenides Embedded with Cu2Te Nanoclusters. *Acs Appl Mater Inter* **8**, 15196-15204 (2016).

36. I. Vlassiouk, G. Polizos, R. Cooper, I. Ivanov, J. K. Keum, F. Paulauskas, P. Datskos, S. Smirnov, Strong and Electrically Conductive Graphene-Based Composite Fibers and Laminates. *Acs Appl Mater Inter* **7**, 10702-10709 (2015).

37. P. Avouris, Graphene: Electronic and Photonic Properties and Devices. *Nano Lett* **10**, 4285-4294 (2010).

38. N. Tombros, A. Veligura, J. Junesch, J. J. van den Berg, P. J. Zomer, M. Wojtaszek, I. J. V. Marun, H. T. Jonkman, B. J. van Wees, Large yield production of high mobility freely suspended graphene electronic devices on a polydimethylglutarimide based organic polymer. *J Appl Phys* **109**, (2011).

39. C. Berger, Z. M. Song, T. B. Li, X. B. Li, A. Y. Ogbazghi, R. Feng, Z. T. Dai, A. N. Marchenkov, E. H. Conrad, P. N. First, W. A. de Heer, Ultrathin epitaxial graphite: 2D electron gas properties and a route toward graphene-based nanoelectronics. *J Phys Chem B* **108**, 19912-19916 (2004).

40. A. A. Balandin, S. Ghosh, W. Z. Bao, I. Calizo, D. Teweldebrhan, F. Miao, C. N. Lau, Superior thermal conductivity of single-layer graphene. *Nano Lett* **8**, 902-907

(2008).

41. L. Wang, X. P. Lu, S. B. Lei, Y. H. Song, Graphene-based polyaniline nanocomposites: preparation, properties and applications. *J Mater Chem A* **2**, 4491-4509 (2014).

42. W. J. Wang, Q. H. Zhang, J. L. Li, X. Liu, L. J. Wang, J. J. Zhu, W. Luo, W. Jiang, An efficient thermoelectric material: preparation of reduced graphene oxide/polyaniline hybrid composites by cryogenic grinding. *Rsc Adv* **5**, 8988-8995 (2015).

43. D. Yoo, J. Kim, J. H. Kim, Direct synthesis of highly conductive poly(3,4-ethylenedioxythiophene):poly(4-styrenesulfonate) (PEDOT:PSS)/graphene composites and their applications in energy harvesting systems. *Nano Res* **7**, 717-730 (2014).

44. T. G. Novak, J. Kim, J. Kim, A. P. Tiwari, H. Shin, J. Y. Song, S. Jeon, Complementary n-Type and p-Type Graphene Films for High Power Factor Thermoelectric Generators. *Adv Funct Mater*, (2020).

45. G. M. Chen, W. Xu, D. B. Zhu, Recent advances in organic polymer thermoelectric composites. *J Mater Chem C* **5**, 4350-4360 (2017).

46. H. Yan, N. Sada, N. Toshima, Thermal transporting properties of electrically conductive polyaniline films as organic thermoelectric materials. *J Therm Anal Calorim* **69**, 881-887 (2002).

47. L. M. Wang, Z. M. Zhang, Y. C. Liu, B. R. Wang, L. Fang, J. J. Qiu, K. Zhang, S. R. Wang, Exceptional thermoelectric properties of flexible organic-inorganic hybrids with monodispersed and periodic nanophase. *Nat Commun* **9**, (2018).

48. Z. H. Tian, H. H. Liu, N. Wang, Y. X. Liu, X. X. Zhang, Facile preparation and

thermoelectric properties of PEDOT nanowires/Bi2Te3 nanocomposites. *J Mater Sci-Mater El* **29**, 17367-17373 (2018).

49. C. L. Wan, R. M. Tian, M. Kondou, R. G. Yang, P. G. Zong, K. Koumoto, Ultrahigh thermoelectric power factor in flexible hybrid inorganic-organic superlattice. *Nat Commun* **8**, (2017).

50. P. A. Zong, J. Liang, P. Zhang, C. L. Wan, Y. F. Wang, K. Koumoto, Graphene-Based Thermoelectrics. *Acs Appl Energ Mater* **3**, 2224-2239 (2020).

51. C. Cho, N. Bittner, W. Choi, J. H. Hsu, C. Yu, J. C. Grunlan, Thermally Enhanced n-Type Thermoelectric Behavior in Completely Organic Graphene Oxide-Based Thin Films. *Adv Electron Mater* **5**, (2019).

52. O. Bubnova, X. Crispin, Towards polymer-based organic thermoelectric generators. *Energ Environ Sci* **5**, 9345-9362 (2012).

53. R. A. Schlitz, F. G. Brunetti, A. M. Glaudell, P. L. Miller, M. A. Brady, C. J. Takacs, C. J. Hawker, M. L. Chabinyc, Solubility-Limited Extrinsic n-Type Doping of a High Electron Mobility Polymer for Thermoelectric Applications. *Adv Mater* **26**, 2825-2830 (2014).

54. J. Liu, L. Qiu, R. Alessandri, X. K. Qiu, G. Portale, J. J. Dong, W. Talsma, G. Ye, A. A. Sengrian, P. C. T. Souza, M. A. Loi, R. C. Chiechi, S. J. Marrink, J. C. Hummelen, L. J. A. Koster, Enhancing Molecular n-Type Doping of Donor-Acceptor Copolymers by Tailoring Side Chains. *Adv Mater* **30**, (2018).

55. Y. Wang, M. Nakano, T. Michinobu, Y. Kiyota, T. Mori, K. Takimiya, Naphthodithiophenediimide-Benzobisthiadiazole-Based Polymers: Versatile n-Type Materials for Field-Effect Transistors and Thermoelectric Devices.

Macromolecules **50**, 857-864 (2017).

56. K. Shi, F. J. Zhang, C. A. Di, T. W. Yan, Y. Zou, X. Zhou, D. B. Zhu, J. Y. Wang, J. Pei, Toward High Performance n-Type Thermoelectric Materials by Rational Modification of BDPPV Backbones. *J Am Chem Soc* **137**, 6979-6982 (2015).

57. X. G. Zhao, D. Madan, Y. Cheng, J. W. Zhou, H. Li, S. M. Thon, A. E. Bragg, M. E. DeCoster, P. E. Hopkins, H. E. Katz, High Conductivity and Electron-Transfer Validation in an n-Type Fluoride-Anion-Doped Polymer for Thermoelectrics in Air. *Adv Mater* **29**, (2017).

58. B. Zhang, J. Sun, H. E. Katz, F. Fang, R. L. Opila, Promising Thermoelectric Properties of Commercial PEDOT:PSS Materials and Their Bi2Te3 Powder Composites. *Acs Appl Mater Inter* **2**, 3170-3178 (2010).

59. J. H. We, S. J. Kim, B. J. Cho, Hybrid composite of screen-printed inorganic thermoelectric film and organic conducting polymer for flexible thermoelectric power generator. *Energy* **73**, 506-512 (2014).

60. A. Sahu, B. Russ, N. C. Su, J. D. Forster, P. Zhou, E. S. Cho, P. Ercius, N. E. Coates, R. A. Segalman, J. J. Urban, Bottom-up design of de novo thermoelectric hybrid materials using chalcogenide resurfacing. *J Mater Chem A* **5**, 3346-3357 (2017).

61. Z. T. Tian, S. Lee, G. Chen, Heat Transfer in Thermoelectric Materials and Devices. *J Heat Trans-T Asme* **135**, (2013).

62. C. Suter, P. Tomes, A. Weidenkaff, A. Steinfeld, Heat Transfer and Geometrical Analysis of Thermoelectric Converters Driven by Concentrated Solar Radiation. *Materials* **3**, 2735-2752 (2010).

63. L. G. Chen, J. Z. Gong, F. R. Sun, C. Wu, Effect of heat transfer on the performance

of thermoelectric generators. *Int J Therm Sci* **41**, 95-99 (2002).

64. Y. Z. Pei, N. A. Heinz, G. J. Snyder, Alloying to increase the band gap for improving thermoelectric properties of Ag2Te. *J Mater Chem* **21**, 18256-18260 (2011).

65. J. W. Stevens, Optimal design of small Delta T thermoelectric generation systems. *Energ Convers Manage* **42**, 709-720 (2001).

66. G. Tan, D. L. Zhao, Study of a thermoelectric space cooling system integrated with phase change material. *Appl Therm Eng* **86**, 187-198 (2015).

67. F. Suarez, D. P. Parekh, C. Ladd, D. Vashaee, M. D. Dickey, M. C. Ozturk, Flexible thermoelectric generator using bulk legs and liquid metal interconnects for wearable electronics. *Appl Energ* **202**, 736-745 (2017).

68. C. S. Kim, G. S. Lee, H. Choi, Y. J. Kim, H. M. Yang, S. H. Lim, S. G. Lee, B. J. Cho, Structural design of a flexible thermoelectric power generator for wearable applications. *Appl Energ* **214**, 131-138 (2018).

69. J. H. Bahk, H. Y. Fang, K. Yazawa, A. Shakouri, Flexible thermoelectric materials and device optimization for wearable energy harvesting. *J Mater Chem C* **3**, 10362-10374 (2015).

70. T. Park, C. Park, B. Kim, H. Shin, E. Kim, Flexible PEDOT electrodes with large thermoelectric power factors to generate electricity by the touch of fingertips. *Energ Environ Sci* **6**, 788-792 (2013).

71. P. Fan, Z. H. Zheng, Y. Z. Li, Q. Y. Lin, J. T. Luo, G. X. Liang, X. M. Cai, D. P. Zhang, F. Ye, Low-cost flexible thin film thermoelectric generator on zinc based thermoelectric materials. *Appl Phys Lett* **106**, (2015).

72. S. J. Kim, H. E. Lee, H. Choi, Y. Kim, J. H. We, J. S. Shin, K. J. Lee, B. J. Cho, High-

Performance Flexible Thermoelectric Power Generator Using Laser Multiscanning Lift-Off Process. *Acs Nano* **10**, 10851-10857 (2016).

73. Y. Du, J. Y. Xu, B. Paul, P. Eklund, Flexible thermoelectric materials and devices. *Appl Mater Today* **12**, 366-388 (2018).

74. Z. Y. Lu, M. Layani, X. X. Zhao, L. P. Tan, T. Sun, S. F. Fan, Q. Y. Yan, S. Magdassi, H. H. Hng, Fabrication of Flexible Thermoelectric Thin Film Devices by Inkjet Printing. *Small* **10**, 3551-3554 (2014).

75. G. Bulman, P. Barletta, J. Lewis, N. Baldasaro, M. Manno, A. Bar-Cohen, B. Yang, Superlattice-based thin-film thermoelectric modules with high cooling fluxes. *Nat Commun* **7**, (2016).

76. S. Lee, K. Esfarjani, T. F. Luo, J. W. Zhou, Z. T. Tian, G. Chen, Resonant bonding leads to low lattice thermal conductivity. *Nat Commun* **5**, (2014).

77. J. Kim, M. Zhang, W. Bosze, S. D. Park, J. H. Lim, N. V. Myung, Maximizing thermoelectric properties by nanoinclusion of gamma-SbTe in Sb2Te3 film via solid-state phase transition from amorphous Sb-Te electrodeposits. *Nano Energy* **13**, 727-734 (2015).

78. S. Chen, Z. F. Ren, Recent progress of half-Heusler for moderate temperature thermoelectric applications. *Mater Today* **16**, 387-395 (2013).

79. Z. Fan, P. C. Li, D. H. Du, J. Y. Ouyang, Significantly Enhanced Thermoelectric Properties of PEDOT:PSS Films through Sequential Post-Treatments with Common Acids and Bases. *Adv Energy Mater* **7**, (2017).

80. H. J. Lee, G. Anoop, H. J. Lee, C. Kim, J. W. Park, J. Choi, H. Kim, Y. J. Kim, E. Lee, S. G. Lee, Y. M. Kim, J. H. Lee, J. Y. Jo, Enhanced thermoelectric performance of PEDOT:

PSS/PANI-CSA polymer multilayer structures. *Energ Environ Sci* **9**, 2806-2811 (2016).

81. H. J. Song, K. F. Cai, Preparation and properties of PEDOT:PSS/Te nanorod composite films for flexible thermoelectric power generator. *Energy* **125**, 519-525 (2017).

82. Y. H. Lin, T. C. Lee, Y. S. Hsiao, W. K. Ling, W. T. Whang, C. H. Chen, Facile Synthesis of Diamino-Modified Graphene/Polyaniline Semi-Interpenetrating Networks with Practical High Thermoelectric Performance. *Acs Appl Mater Inter* **10**, 4946-4952 (2018).

83. Q. Yao, Q. Wang, L. M. Wang, L. D. Chen, Abnormally enhanced thermoelectric transport properties of SWNT/PANI hybrid films by the strengthened PANI molecular ordering. *Energ Environ Sci* **7**, 3801-3807 (2014).

84. K. Zhang, S. R. Wang, J. J. Qiu, J. L. Blackburn, X. Zhang, A. J. Ferguson, E. M. Millers, B. L. Weeks, Effect of host-mobility dependent carrier scattering on thermoelectric power factors of polymer composites. *Nano Energy* **19**, 128-137 (2016).

85. T. Zhang, K. W. Li, C. C. Li, S. Y. Ma, H. H. Hng, L. Wei, Mechanically Durable and Flexible Thermoelectric Films from PEDOT:PSS/PVA/Bi0.5Sb1.5Te3 Nanocomposites. *Adv Electron Mater* **3**, (2017).

86. X. C. Tian, J. Jin, S. Q. Yuan, C. K. Chua, S. B. Tor, K. Zhou, Emerging 3D-Printed Electrochemical Energy Storage Devices: A Critical Review. *Adv Energy Mater* **7**, (2017).

87. M. M. Laronda, A. L. Rutz, S. Xiao, K. A. Whelan, F. E. Duncan, E. W. Roth, T. K. Woodruff, R. N. Shah, A bioprosthetic ovary created using 3D printed microporous

scaffolds restores ovarian function in sterilized mice. *Nat Commun* **8**, (2017).

88. Y. J. Li, T. T. Gao, Z. Yang, C. J. Chen, W. Luo, J. W. Song, E. Hitz, C. Jia, Y. B. Zhou, B. Y. Liu, B. Yang, L. B. Hu, 3D-Printed, All-in-One Evaporator for High-Efficiency Solar Steam Generation under 1 Sun Illumination. *Adv Mater* **29**, (2017).

89. M. L. Gou, X. Qu, W. Zhu, M. L. Xiang, J. Yang, K. Zhang, Y. Q. Wei, S. C. Chen, Bio-inspired detoxification using 3D-printed hydrogel nanocomposites. *Nat Commun* **5**, (2014).

90. K. A. Borup, E. S. Toberer, L. D. Zoltan, G. Nakatsukasa, M. Errico, J. P. Fleurial, B. B. Iversen, G. J. Snyder, Measurement of the electrical resistivity and Hall coefficient at high temperatures. *Rev Sci Instrum* **83**, (2012).

91. M. Stavytska-Barba, A. M. Kelley, Surface-Enhanced Raman Study of the Interaction of PEDOT:PSS with Plasmonically Active Nanoparticles. *J Phys Chem C* **114**, 6822-6830 (2010).

92. S. R. S. Kumar, N. Kurra, H. N. Alshareef, Enhanced high temperature thermoelectric response of sulphuric acid treated conducting polymer thin films. *J Mater Chem C* **4**, 215-221 (2016).

93. M. Reyes-Reyes, I. Cruz-Cruz, R. Lopez-Sandoval, Enhancement of the Electrical Conductivity in PEDOT:PSS Films by the Addition of Dimethyl Sulfate. *J Phys Chem C* **114**, 20220-20224 (2010).

94. P. Sakunpongpitiporn, K. Phasuksom, N. Paradee, A. Sirivat, Facile synthesis of highly conductive PEDOT:PSS via surfactant templates. *Rsc Adv* **9**, 6363-6378 (2019).

95. Y. Zheng, X. Y. Tan, X. J. Wan, X. Cheng, Z. H. Liu, Q. Y. Yan, Thermal Stability and

Mechanical Response of Bi2Te3-Based Materials for Thermoelectric Applications. *Acs Appl Energ Mater* **3**, 2078-2089 (2020).

96. J. P. Fu, S. Y. Song, X. G. Zhang, F. Cao, L. Zhou, X. Y. Li, H. J. Zhang, Bi2Te3 nanoplates and nanoflowers: Synthesized by hydrothermal process and their enhanced thermoelectric properties. *Crystengcomm* **14**, 2159-2165 (2012).

97. C. M. Tang, Z. C. Huang, J. Pei, B. P. Zhang, P. P. Shang, Z. H. Shan, Z. Y. Zhang, H. Y. Gu, K. B. Wen, Bi2Te3 single crystals with high room-temperature thermoelectric performance enhanced by manipulating point defects based on first-principles calculation. *Rsc Adv* **9**, 14422-14431 (2019).

98. G. Zheng, X. L. Su, T. Liang, Q. B. Lu, Y. G. Yan, C. Uher, X. F. Tang, High thermoelectric performance of mechanically robust n-type Bi2Te3-xSex prepared by combustion synthesis. *J Mater Chem A* **3**, 6603-6613 (2015).

99. N. D. Lu, L. Li, M. Liu, A review of carrier thermoelectric-transport theory in organic semiconductors. *Phys Chem Chem Phys* **18**, 19503-19525 (2016).

100. J. Smith, R. Hamilton, I. McCulloch, N. Stingelin-Stutzmann, M. Heeney, D. D. C. Bradley, T. D. Anthopoulos, Solution-processed organic transistors based on semiconducting blends. *J Mater Chem* **20**, 2562-2574 (2010).

101. M. Y. Wang, R. Gurunathan, K. Imasato, N. R. Geisendorfer, A. E. Jakus, J. Peng, R. N. Shah, M. Grayson, G. J. Snyder, A Percolation Model for Piezoresistivity in Conductor-Polymer Composites. *Adv Theor Simul* **2**, (2019).

102. J. P. Clerc, G. Giraud, J. M. Laugier, J. M. Luck, The Ac Electrical-Conductivity of Binary Disordered-Systems, Percolation Clusters, Fractals and Related Models. *Adv Phys* **39**, 191-308 (1990).

103. G. J. Snyder, E. S. Toberer, Complex thermoelectric materials. *Nat Mater* **7**, 105-114 (2008).

104. Y. Z. Pei, X. Y. Shi, A. LaLonde, H. Wang, L. D. Chen, G. J. Snyder, Convergence of electronic bands for high performance bulk thermoelectrics. *Nature* **473**, 66-69 (2011).

105. L. P. Hu, T. J. Zhu, X. H. Liu, X. B. Zhao, Point Defect Engineering of High-Performance Bismuth-Telluride-Based Thermoelectric Materials. *Adv Funct Mater* **24**, 5211-5218 (2014).

106. Q. S. Wei, M. Mukaida, Y. Naitoh, T. Ishida, Morphological Change and Mobility Enhancement in PEDOT:PSS by Adding Co-solvents. *Adv Mater* **25**, 2831-2836 (2013).

107. V. J. Lin, J. J. Zeng, C. L. Tsai, Enhancement of the carrier mobility of poly(3,4-ethylenedioxythiophene) doped with poly(4-styrenesulfonate) by incorporating reduced graphene oxide. *Appl Phys Lett* **101**, (2012).

108. X. Y. Zhou, Y. C. Yan, X. Lu, H. T. Zhu, X. D. Han, G. Chen, Z. F. Ren, Routes for high-performance thermoelectric materials. *Mater Today* **21**, 974-988 (2018).

109. Y. Zheng, Q. Zhang, X. L. Su, H. Y. Xie, S. C. Shu, T. L. Chen, G. J. Tan, Y. G. Yan, X. F. Tang, C. Uher, G. J. Snyder, Mechanically Robust BiSbTe Alloys with Superior Thermoelectric Performance: A Case Study of Stable Hierarchical Nanostructured Thermoelectric Materials. *Adv Energy Mater* **5**, (2015).

110. L. P. Hu, T. J. Zhu, Y. G. Wang, H. H. Xie, Z. J. Xu, X. B. Zhao, Shifting up the optimum figure of merit of p-type bismuth telluride-based thermoelectric materials for power generation by suppressing intrinsic conduction. *Npg Asia Mater* **6**, (2014).

111. K. T. Kim, K. J. Kim, G. H. Ha, Thermoelectric Properties of P-Type Bismuth Telluride Powders Synthesized by a Mechano-Chemical Process. *Electron Mater Lett* **6**, 177-180 (2010).

112. S. I. Kim, K. H. Lee, H. A. Mun, H. S. Kim, S. W. Hwang, J. W. Roh, D. J. Yang, W. H. Shin, X. S. Li, Y. H. Lee, G. J. Snyder, S. W. Kim, Dense dislocation arrays embedded in grain boundaries for high-performance bulk thermoelectrics. *Science* **348**, 109-114 (2015).

113. G. Zheng, X. L. Su, H. Y. Xie, Y. J. Shu, T. Liang, X. Y. She, W. Liu, Y. G. Yan, Q. J. Zhang, C. Uher, M. G. Kanatzidis, X. F. Tang, High thermoelectric performance of p-BiSbTe compounds prepared by ultra-fast thermally induced reaction. *Energ Environ Sci* **10**, 2638-2652 (2017).

114. J. H. Son, M. W. Oh, B. S. Kim, S. D. Park, B. K. Min, M. H. Kim, H. W. Lee, Effect of ball milling time on the thermoelectric properties of p-type (Bi,Sb)(2)Te-3. *J Alloy Compd* **566**, 168-174 (2013).

115. Q. L. Jiang, C. C. Liu, H. J. Song, J. K. Xu, D. Z. Mo, H. Shi, Z. P. Wang, F. X. Jiang, B. Y. Lu, Z. Y. Zhu, Free-standing PEDOT:PSS Film as Electrode for the Electrodeposition of Bismuth Telluride and Its Thermoelectric Performance. *Int J Electrochem Sc* **9**, 7540-7551 (2014).

116. J. H. Xiong, L. Y. Wang, J. K. Xu, C. C. Liu, W. Q. Zhou, H. Shi, Q. L. Jiang, F. X. Jiang, Thermoelectric performance of PEDOT:PSS/Bi2Te3-nanowires: a comparison of hybrid types. *J Mater Sci-Mater El* **27**, 1769-1776 (2016).

117. Y. Du, K. F. Cai, S. Chen, P. Cizek, T. Lin, Facile Preparation and Thermoelectric Properties of Bi2Te3 Based Alloy Nanosheet/PEDOT:PSS Composite Films. *Acs Appl*

Mater Inter **6**, 5735-5743 (2014).

118. G. Goo, G. Anoop, S. Unithrattil, W. S. Kim, H. J. Lee, H. B. Kim, M. H. Jung, J. Park, H. C. Ko, J. Y. Jo, Proton-Irradiation Effects on the Thermoelectric Properties of Flexible Bi2Te3/PEDOT:PSS Composite Films. *Adv Electron Mater* **5**, (2019).

119. S. M. Shin, J. W. Roh, H. S. Kim, R. K. Chen, Role of surfactant on thermoelectric behaviors of organic-inorganic composites. *J Appl Phys* **123**, (2018).

120. A. A. Abd Rahman, A. A. Umar, M. H. U. Othman, Effect of bismuth telluride concentration on the thermoelectric properties of PEDOT:PSS-glycerol organic films. *Physica E* **66**, 293-298 (2015).

121. D. Li, R. R. Sun, X. Y. Qin, Improving thermoelectric properties of p-type Bi2Te3-based alloys by spark plasma sintering. *Prog Nat Sci-Mater* **21**, 336-340 (2011).

122. Y. M. Zhou, L. D. Zhao, Promising Thermoelectric Bulk Materials with 2D Structures. *Adv Mater* **29**, (2017).

123. H. J. Song, C. C. Liu, H. F. Zhu, F. F. Kong, B. Y. Lu, J. K. Xu, J. M. Wang, F. Zhao, Improved Thermoelectric Performance of Free-Standing PEDOT:PSS/Bi2Te3 Films with Low Thermal Conductivity. *J Electron Mater* **42**, 1268-1274 (2013).

124. R. Liu, X. Tan, G. K. Ren, Y. C. Liu, Z. F. Zhou, C. Liu, Y. H. Lin, C. W. Nan, Enhanced Thermoelectric Performance of Te-Doped Bi2Se3-xTex Bulks by Self-Propagating High-Temperature Synthesis. *Crystals* **7**, (2017).

125. Y. Pan, T. R. Wei, C. F. Wu, J. F. Li, Electrical and thermal transport properties of spark plasma sintered n-type Bi2Te3-xSex alloys: the combined effect of point defect and Se content. *J Mater Chem C* **3**, 10583-10589 (2015).

126. S. D. Kang, G. J. Snyder, Charge-transport model for conducting polymers. *Nat*

Mater **16**, 252-257 (2017).

127. J. Peng, I. Witting, N. Geisendorfer, M. Wang, M. Chang, A. Jakus, C. Kenel, X. Yan, R. Shah, G. J. Snyder, M. Grayson, 3D extruded composite thermoelectric threads for flexible energy harvesting. *Nat Commun* **10**, (2019).

128. N. D. Lu, L. Li, M. Liu, Universal carrier thermoelectric-transport model based on percolation theory in organic semiconductors. *Phys Rev B* **91**, (2015).

129. C. W. Nan, Y. Shen, J. Ma, Physical Properties of Composites Near Percolation. *Annu Rev Mater Res* **40**, 131-151 (2010).

130. D. B. T. J. C. Garland, *Electrical Transport and Optical Properties in Inhomogeneous Media* (Amer Inst of Physics, 1977).

131. H. Lee, D. Vashaee, D. Z. Wang, M. S. Dresselhaus, Z. F. Ren, G. Chen, Effects of nanoscale porosity on thermoelectric properties of SiGe. *J Appl Phys* **107**, (2010).

132. N. D. M. Neil W Ashcroft, *Solid state physics* (New York: Holt, Rinehart and Winston, 1976).

133. X. F. Xu, J. Zhou, J. Chen, Thermal Transport in Conductive Polymer-Based Materials. *Adv Funct Mater* **30**, (2020).

134. C. Han, G. J. Tan, T. Varghese, M. G. Kanatzidis, Y. L. Zhang, High-Performance PbTe Thermoelectric Films by Scalable and Low-Cost Printing. *Acs Energy Lett* **3**, 818-+ (2018).

135. L. Tzounis, M. Zappalorto, F. Panozzo, K. Tsirka, L. Maragoni, A. S. Paipetis, M. Quaresimin, Highly conductive ultra-sensitive SWCNT-coated glass fiber reinforcements for laminate composites structural health monitoring. *Compos Part B-Eng* **169**, 37-44 (2019).

136. X. Wang, M. Jiang, Z. W. Zhou, J. H. Gou, D. Hui, 3D printing of polymer matrix composites: A review and prospective. *Compos Part B-Eng* **110**, 442-458 (2017).

137. N. G. T. Cyrus K. Aidun, *Liquid Film Coating* (High-Speed Blade Coating).

138. H. T. Yang, P. Jiang, Large-Scale Colloidal Self-Assembly by Doctor Blade Coating. *Langmuir* **26**, 13173-13182 (2010).

139. Y. Wang, Y. G. Shi, D. Q. Mei, Z. C. Chen, Wearable thermoelectric generator to harvest body heat for powering a miniaturized accelerometer. *Appl Energ* **215**, 690-698 (2018).

140. Y. G. Shi, Y. C. Wang, D. Q. Mei, Z. C. Chen, Wearable Thermoelectric Generator With Copper Foam as the Heat Sink for Body Heat Harvesting. *Ieee Access* **6**, 43602-43611 (2018).

141. M. Kashiwagi, T. Koshi, E. Iwase, High Performance Flexible Thermoelectric Device Included Rigid Material. *Proc Ieee Micr Elect*, 1010-1012 (2019).

142. W. Ren, Y. Sun, D. L. Zhao, A. Aili, S. Zhang, C. Q. Shi, J. L. Zhang, H. Y. Geng, J. Zhang, L. X. Zhang, J. L. Xiao, R. G. Yang, High-performance wearable thermoelectric generator with self-healing, recycling, and Lego-like reconfiguring capabilities. *Sci Adv* **7**, (2021).

143. B. Lee, H. Cho, K. T. Park, J. S. Kim, M. Park, H. Kim, Y. Hong, S. Chung, High-performance compliant thermoelectric generators with magnetically self-assembled soft heat conductors for self-powered wearable electronics. *Nat Commun* **11**, (2020).

144. S. Hong, Y. Gu, J. K. Seo, J. Wang, P. Liu, Y. S. Meng, S. Xu, R. K. Chen, Wearable thermoelectrics for personalized thermoregulation. *Sci Adv* **5**, (2019).

145. G. Lee, C. S. Kim, S. Kim, Y. J. Kim, H. Choi, B. J. Cho, Flexible heatsink based on a phase-change material for a wearable thermoelectric generator. *Energy* **179**, 12-18 (2019).

146. H. Park, D. Kim, Y. Eom, D. Wijethunge, J. Hwang, H. Kim, W. Kim, Mat-like flexible thermoelectric system based on rigid inorganic bulk materials. *J Phys D Appl Phys* **50**, (2017).

147. W. Wang, Y. Ji, H. Xu, H. Li, T. Visan, F. Golgovici, A high packing density micro-thermoelectric power generator based on film thermoelectric materials fabricated by electrodeposition technology. *Surf Coat Tech* **231**, 583-589 (2013).